MULTILAYER RELAXATIONS ON HIGH-MILLER-INDEX METAL SURFACES

SUN YIYANG

(M.Sc., Xiamen University)

(B.Eng., Jilin University)

A THESIS SUBMITTED

FOR THE DEGREE OF DOCTOR OF PHILOSOPHY

DEPARTMENT OF PHYSICS

NATIONAL UNIVERSITY OF SINGAPORE

2004

Acknowledgements

I am indebted to my supervisors, Associate Professor Andrew Wee Thye Shen and Associate Professor Alfred Huan Cheng Hon, for their guidance and advice throughout my thesis work.

I am grateful to Associate Professor Feng Yuan Ping for his generosity with time and expertise teaching me the programs for first-principles calculations.

I wish to thank Dr Xu Hai, Mr Wong How Kwong, Mr Chen Wei and Mr Md Abdul Kader Zilani for the cherishable moments working together in the Surface Science Lab.

I appreciate Dr Ismail and Professor Franco Jona for providing me with their experimental LEED data.

I acknowledge the National University of Singapore for a research scholarship and grants to overseas and local conferences.

I owe my parents and my wife, Mao Mao, for their constant love, support and encouragement.

Contents

Summary

The structures of Cu(210) and Fe(310) have been studied by quantitative low-energy electron diffraction (LEED) analyses and first-principles pseudopotential calculations. It is demonstrated that the layer-doubling method works well for high-index transition metal surfaces with interlayer spacings down to about 0.8 Å. The structures obtained from the two techniques on both surfaces show good consistency. This indicates that the pseudopotential plane-wave method is a reliable tool for studying the structures of high-index transition metal surfaces, which is not normally studied using the pseudopotential method due to the prohibitively large basis set needed.

By observing the existing results from several high-index Cu surfaces, an empirical rule for multilayer relaxations on open metal surfaces is proposed, which can be described as: At bulk-truncated configuration, define a *surface slab* in which the nearest neighbors of all atoms are fewer than those in the bulk. In the process of relaxation, the interlayer spacing between each pair of layers within this slab contracts, while the spacing between this slab and the substrate expands.

For checking the validity of this rule, pseudopotential calculations have been carried out along two directions. Firstly, taking Cu as an example, the high-index surfaces of fcc structure with interlayer spacings down to 0.5 Å are studied. It is shown that the proposed rule is obeyed on all these surfaces. Secondly, the relaxations of (311), (331) and (210) surfaces of seven transition metals, including Ni, Cu, Rh, Pd, Ag, Ir and Pt, have been studied. The results show that the surfaces of the same orientation, but of different materials, have the same relaxation sequence and conform to the proposed rule.

Comparison with existing results on the open surfaces of other structures, such as bcc, hcp and even reconstructed missing-row surfaces, also shows the validity of the rule.

Abbreviations

AFM	Atomic Force Microscopy
BZ	Brillouin Zone
CASTEP	Cambridge Serial Total Energy Package
DFT	Density Functional Theory
DIIS	Direct Inversion in the Iterative Space
FLAPW	Full-potential Linearized Augmented Plane-wave
GGA	Generalized Gradient Approximation
HEIS	High-energy Ion Scattering
LAPW	Linearized Augmented Plane-wave
LCAO	Linear Combination of Atomic Orbitals
LDA	Local Density Approximation
LEED	Low-energy Electron Diffraction
LEIS	Low-energy Ion Scattering
LMTO	Linear Muffin-tin Orbital
MEIS	Medium-energy Ion Scattering
NCPP	Norm-conserving Pseudopotential
PAW	Projector Augmented Wave
RFS	Renormalized Forward Scattering
RHEED	Reflection High-energy Electron Diffraction
RMM	Residual Minimization Method
SEXAFS	Surface Extended X-ray Absorption Fine Structure
STM	Scanning Tunneling Microscopy
USPP	Ultra-soft Pseudopotential
VASP	Vienna *ab initio* Simulation Package
XPD	X-ray Photoelectron Diffraction

Publications

1. Y. Y. Sun, A. T. S. Wee, and A. C. H. Huan. "Study of a computational-time-saving scheme for quantitative LEED analysis by the matrix inversion method", *Surf. Rev. Lett.* **10**, 493, (2003).

2. Y. Y. Sun, H. Xu, J. C. Zheng, J. Y. Zhou, Y. P. Feng, A. C. H. Huan, and A. T. S. Wee. "Multilayer relaxation of Cu(210) studied by layer-doubling LEED analysis and pseudopotential density functional theory calculations", *Phys. Rev. B* **68**, 115420, (2003).

3. Y. Y. Sun, H. Xu, Y. P. Feng, A. C. H. Huan, and A. T. S. Wee. "Structure of Fe(310) studied by quantitative LEED analysis and pseudopotential DFT calculations", *Surf. Sci.* **546**, L808, (2003).

4. Y. Y. Sun, H. Xu, Y. P. Feng, A. C. H. Huan, and A. T. S. Wee. "Multilayer relaxations of (311), (331) and (210) fcc transition metal surfaces studied by pseudopotential DFT calculations", *Surf. Sci.* **548**, 309, (2004).

5. Y. Y. Sun, H. Xu, Y. P. Feng, A. C. H. Huan, and A. T. S. Wee. "A rule for structures of open metal surfaces", *Phys. Rev. Lett.*, accepted.

Chapter 1

Introduction

Surface structure determination is an important branch of surface science. Almost all quantitative studies on electronic, energetic, vibrational and magnetic properties of a surface require detailed structural information on it. Surface structures that have been elucidated so far are mainly confined to close-packed low-Miller-index (low-index in short) surfaces. In the past two decades, open (loosely-packed) surfaces have received more attention than before due to the practical interests arising from areas such as heterogeneous catalysis and crystal growth. Nevertheless, the information on open surfaces is still limited as opposed to that on close-packed surfaces. This thesis is devoted to the study of multilayer relaxations on open metal surfaces.

1.1 Open Surfaces

Open surfaces normally refer to high-index single crystal surfaces. Yet, some low-index surfaces also exhibit "open" features, such as the bcc(111), hcp($10\bar{1}0$) and fcc(110) surfaces. A common point of high-index and open low-index surfaces is that they all have small packing densities so that more than one atomic layer is "exposed" to the vacuum. More strictly, the coordination of the atoms in at least two layers is lowered when creating the surface. In this thesis, the term "open" is adopted to describe this category of surfaces whenever a general purpose is aimed at, while high-index metal surfaces will actually be the main subject of this thesis.

A high-index single crystal surface is obtained by cutting a crystal at a specific angle away from a low-index plane. Even perfect high-index surfaces exhibit *terraces* that are oriented to certain low-index planes and separated by well-ordered monoatomic *steps*. On some of these surfaces the steps are straight, while on others they are in a zigzag shape. The atomic sites where the steps change direction are called *kinks*. Since every high-index surface is vicinal to a certain low-index plane and characterized by the existence of steps, a high-index surface is also referred to as a *vicinal* or *stepped* surface. The atomic sites at the steps and kinks are highly active due to the lower coordination, hence play an important role in catalytic reactions [1]. This feature of high-index surfaces makes them suitable platforms

on which experimental and theoretical studies can be conducted for understanding the fundamental mechanisms of heterogenous catalysis.

Another feature of high-index surfaces is the low symmetry. There is at most a mirror plane that can be present on these surfaces. If such a mirror plane exists, the direction of the steps is perpendicular to the mirror. Studies have shown that preferential nucleation takes place along the steps during thin film growth. This is helpful for the self-organized growth of low dimensional structures, such as nanowires [2–5]. Although such studies have so far been mainly conducted on semiconductor surfaces, the potential application for the growth of magnetic nanowires on high-index metal surfaces is promising [6], especially for high density data storage. High-index surfaces without any symmetry also have a niche in chiral chemistry [7]. Some of these surfaces have proven to be enantioselective [8]. Studies on chiral single crystal surfaces have opened a new field for chiral chemistry. The current reaction carriers for chiral syntheses are mainly organic materials which cannot be used for high temperature reactions and single crystal chiral metal surfaces are more suitable for these applications.

1.2 Structures of Surfaces

When cutting a single crystal to form two surfaces, the fresh atomic configuration (or the bulk-truncated configuration) in the surface region is not stable due to the change in atomic coordination. The surface atoms undergo displacements to achieve a stable configuration. Various deformations with respect to the bulk-truncated configuration may occur on single crystal surfaces. All of them are, from the point of view of energetics, the consequence of the minimization of free energy of the surfaces.

The deformation that most likely occurs on clean open metal surfaces is *multilayer relaxation*, that is, more than one atomic layer in the surface is displaced from the bulk-truncated configuration, while the shape and size of the original surface unit cell remain unchanged. Open metal surfaces usually exhibit more significant multilayer relaxations than close-packed surfaces.

Another type of deformation is *surface reconstruction*, which refers to a rearrangement of one or more atomic layers in the surface region resulting in a change in the periodicity of the surface along one or both basis vectors of the substrate. Surface reconstructions are rather common on clean semiconductor surfaces due to the strong interactions between the dangling covalent bonds on these surfaces, a classical example being the Si(111)-(7x7) surface. On clean metal surfaces, however, the cases of reconstruction are fewer due to the non-local nature of the metallic bonds which allows the surface stresses to be released easily without severe change in the atomic positions. Nevertheless, surface reconstructions have been observed on several heavy transition metal surfaces, such as Ir(110) [9], Pt(110) [10] and W(100) [11]. Interestingly, on clean high-index metal surfaces few reconstructions have been observed. One of the rare exceptions is the clean Pt(311) surface on which a (2x1) reconstruction has been reported [12].

Facets are a kind of more severe deformations occurring on surfaces. They are pyramid-like surface structures where each side of the pyramid belongs to specific crystal planes. Faceting on clean surfaces is rarely observed in experiments. This phenomenon is usually induced by adsorbate atoms which have strong interactions with the substrate atoms.

1.3 Scope of Research

This thesis focuses on the multilayer relaxations of open metal surfaces. The main techniques involved will be quantitative low-energy electron diffraction (LEED) analysis and first-principles total-energy calculations based on density functional theory (DFT). Quantitative LEED analysis is the principal experimental technique for surface crystallography and DFT is the most definitive theoretical method for structural studies on single crystal surfaces. The two techniques will be briefly reviewed in Chapter 2.

Chapter 3 presents results on quantitative LEED analysis. It will be shown that the layer-doubling method works well for Cu(210). This method is much more efficient than the l-space methods which are currently dominant in the quantitative

LEED analysis of high-index metal surfaces.

Chapter 4 is dedicated to solving the discrepancy in the literature on the structure of Fe(310) obtained by quantitative LEED analysis and first-principles calculations. It will be demonstrated that the pseudopotential plane-wave method is able to obtain consistent results with LEED.

In Chapter 5, an empirical rule for multilayer relaxations on open metal surfaces is proposed. A systematic evaluation of this rule is conducted on a series of vicinal Cu surfaces.

In Chapter 6, the proposed rule will be further evaluated on the (311), (331) and (210) surfaces of seven fcc transition metals.

Concluding remarks will be given in Chapter 7.

Chapter 2

Methodology

There is a long list of techniques that are suitable for surface structure studies. Each technique has its advantages and limitations. For experimental techniques, various probes can be used, such as electrons (e.g., LEED and RHEED), ions (e.g., LEIS, MEIS and HEIS), X-rays (e.g., XPD and SEXAFS) and atomic tips (e.g., STM and AFM). For theoretical techniques, both empirical (or semi-empirical) and first-principles methods are available. The technique of choice should be decided on a case by case basis. Often, a combination of two or more techniques is required to elucidate a surface structure. In this thesis, two techniques are used. They are quantitative LEED analysis and first-principles DFT calculations.

2.1 Quantitative LEED Analysis

In 1927, Davisson and Germer experimentally demonstrated the wavelike properties of electrons on a single crystal Ni surface [13]. However, the usage of electron diffraction after Davisson and Germer's discovery is mainly confined in the high-energy electrons until 1960's when the development in both ultra-high vacuum technique and multiple scattering theory makes it possible to experimentally prepare a clean surface and theoretically describe a low-energy electron diffraction process. Since then, quantitative LEED analysis has been the principal experimental technique for surface crystallography. According to the NIST Surface Structure Database (Ver. 4.0) [14], about 60% of determined surface structures are contributed by this technique. Two reasons may account for this. Firstly, the experimental setup of LEED is low-cost compared with other analytical surface science techniques and can be easily incorporated in an ultra-high vacuum system. Secondly, the computer simulation packages for quantitative LEED analysis have been developed over three decades and are currently available for free from many groups.

2.1.1 Low Energy Electron Diffraction

LEED is an experimental technique used to study crystalline surfaces, mainly single crystal surfaces (often with atomic or molecular adsorptions). In LEED, a

surface is excited by a beam of incident electrons and the elastically back-scattered wavefield is then analysed to obtain structural information of the surface. The incident electrons are normally in the energy range from 20 eV to 500 eV. The electrons in this range possess two good properties which make them suitable probes for surface structures. Firstly, the inelastic mean free path of electrons in this energy range is $5-10$ Å, which means that the electrons can only penetrate several atomic layers into the surface. In other words, low-energy electrons are surface-sensitive. Beyond this range, the depth of penetration rapidly increases. Secondly, electron energies from 20 eV to 500 eV correspond to de Broglie wavelengths from 2.74 Å to 0.55 Å, which are excellent for crystallographic studies on surfaces, just like X-rays for bulk crystals.

The wavefield back-scattered from a 2-dimensional periodic system consists of an array of diffraction beams, each of which is related to the incident electron beam by a 2-dimensional reciprocal lattice vector $\mathbf{g}$. This can be regarded as an exchange of momentum $\mathbf{g}$ between the incident electrons and the lattice to conserve the total parallel momentum of the system. The structure factor (Ref. [15], p.79) of the periodic system (i.e., the constructive interference) prevents the beams with the momentums other than $\mathbf{g}$ from contributing to the back-scattered wavefield.

Two kinds of information are available from the diffraction beams, the diffraction pattern and the beam intensities. The diffraction pattern can be used to analyze the surface symmetry and deduce the size and shape of the surface unit cell, while the relation between the beam intensities and the incident energy, often referred to as I-V or $I(E)$ curves, implicitly contains the detailed structural information of the surface.

The interpretation of the LEED pattern is normally straightforward. For example, Figure 2.1 shows the LEED patterns from the SiC(0001), Si(001) and Cu(210) surfaces. From these patterns, one can easily observe that the first one has a (3×3) reconstruction, the second a (2×1) and the third unreconstructed.

On the contrary, extracting structural information from the beam intensities is much more complicated and sophisticated theory is required [15,16]. The detailed

(a) (b) (c)

Fig. 2.1: LEED patterns. (a) SiC(0001)-(3x3); (b) Si(001)-(2x1); (c) Cu(210)-(1x1).

structure determination by LEED is often referred to as quantitative LEED analysis, which consists of two main steps. In the first step, one needs to acquire a set of I-V curves from the diffraction beams. In the next step, the structure of the surface is derived from the I-V curves in a trial-and-error way. The retrieval procedure starts from a reasonably guessed trial structure (often known as a *model*). The theoretical I-V curves are then calculated from the trial structure and compared with the experimental ones. Whether this trial structure is accepted as the "real" structure is decided by the agreement between the two sets of curves. If it is rejected, a new trial structure will be generated by systematically adjusting the old one. This procedure will be repeated until a structure which gives the best fit to the experimental curves is found. The calculations of the theoretical I-V curves have to be conducted within the framework of multiple scattering (or dynamical) theory due to the large scattering cross-sections (i.e., strong interactions) between the incident electrons and the surface atoms. This is different from the case of X-ray diffraction, where the diffraction process is mainly determined by the geometric parameters of the system and single scattering (or kinematic) theory is sufficient.

In the following subsections, the experimental setup of LEED and the theories of quantitative LEED analysis will be introduced.

2.1.2 Experimental Setup

Figure 2.2 shows a standard LEED setup, which is essentially made up of an electron gun, a sample manipulator and a display system.

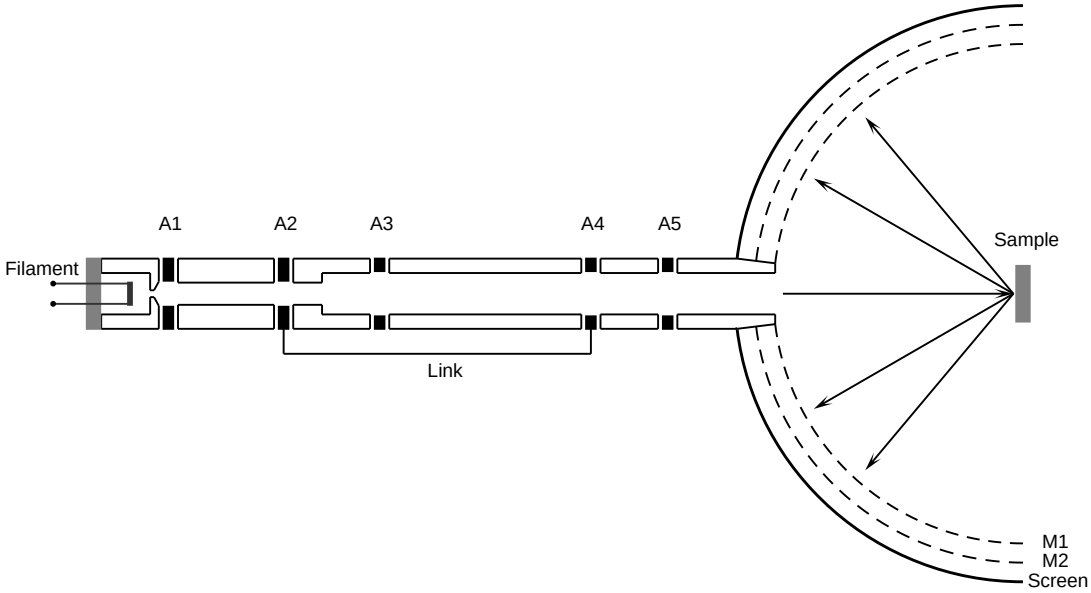

Fig. 2.2: A schematic LEED setup. The left part is the electron gun and the right shows the sample and the display system. The black blocks denote the anodes, where A2 and A4 have been linked together.

An electron gun is used to produce a well collimated monoenergetic electron beam. At the rear end of the electron gun is a cathode, which is usually a thoria-coated tungsten filament or a piece of LaB_6 crystal. When the cathode is heated up over a certain temperature by a current, electrons will overcome the work function of the filament material and emit from the cathode. The cathode is housed in a so-called Wehnelt cylinder which is applied with an adjustable negative bias (normally shown as *Grid* on a standard LEED controller) with respect to the filament in order to control the emission current. The control on the incident energy E_p is implemented by applying a negative bias ($-E_\mathrm{p}$) on the filament with respect to the sample, which is earthed. Once passing through the aperture of the Wehnelt cylinder, the electrons enter a focusing region formed by a series of anodes (usually five, see Fig. 2.2) [17]. A1, the nearest anode to the filament, is applied with a high positive voltage (e.g., +600 V) to extract the electrons. A5, the farthest anode from the filament is earthed. The voltages applied on other anodes

are either user-adjustable or slaved to E_{p} (*A2* and *Focus* on a LEED controller). Finally, a beam of electrons with a diameter of about 1 mm and a current of the order 1 μA is obtained after the aperture located at the front end of the gun.

The electron beam generated from the gun passes through a vacuum region and impinges on the sample which is mounted on a manipulator. The electrons will undergo scattering in the surface and an array of diffracted beams as well as a flux of electrons due to the inelastic scattering will emerge from the surface and travel towards the display system.

The display system is formed by a series of concentric meshes and a fluorescent screen. For a LEED experiment, two meshes are sufficient. If the same system is also used for Auger electron spectroscopy, one (or two) more mesh is helpful for improving the energy resolution. The mesh near the sample (M1 in Fig. 2.2) is earthed in order to ensure that the electrons travel in a field-free region before reaching this mesh. The mesh near the screen (M2) is biased with a retarding potential $(-E_{\mathrm{p}} + \Delta V_{\mathrm{m}})$ to filter out the electrons due to inelastic scattering (i.e., those with $E < E_{\mathrm{p}}$), where ΔV_{m} is an adjustable tolerance potential within a typical range $0-10$ eV and shown as *Mesh* on a LEED controller. The electrons that are able to overcome the retarding potential (i.e., those elastically back-scattered) are accelerated by a high voltage (typically +5 kV) applied on the screen making them energetic enough to light up the fluorescent screen. The intensities of the diffraction beams are then measured by a rear-view video camera system.

For conducting a quantitative LEED analysis, several points on the experimental setup are worth mentioning:

- The sample should be mounted on an accurately adjustable manipulator which allows precise control of the incident angle (often normal incidence).
- A computer-controlled rapid data acquisition system should be used in order to reduce the influence of the residual gases on the sample due to adsorption.
- It is preferred that the sample be cooled to low temperatures in order to reduce the temperature effect, such as vibration and desorption.

2.1.3 Muffin-tin Approximation

Once the incident electrons approach the surface, they start to feel the potential formed by the nuclei and the electrons in the surfaces until they are back-scattered away from the surface. Exactly describing the scattering of the electrons in the surface requires that the potential is known mathematically. Obtaining an accurate form of this potential is possible from first-principles calculations. However, a practical LEED theory based on such a potential is not available yet. The existing LEED theories are based on approximations to this potential. The simplest one is the muffin-tin approximation, which originated from the band-structure calculations in solid states.

The muffin-tin approximation takes the regions surrounded by the largest possible non-overlapping spheres centered on the nuclei as the ion-cores. The potential inside each ion-core (the ion-core potential) is treated spherically symmetric. In the interstitial region between the ion-cores the potential is taken constant (represented by V_0), which is usually referred to as the inner potential (or the optical potential, the muffin-tin constant) in the context of LEED. The ion-core potential is largely determined by the nuclear charge and the core-electrons so that it is *expected* not to change the scattering property significantly with the change in the chemical environment, even near the surface. However, near the surface the potential outside the muffin-tins is no longer constant. It will gradually increase to the vacuum level and form a surface potential step (or a barrier potential). Frequently, this surface step is treated as only a refractive layer. Or in other words, the step potential is a function of only the z coordinate and has no structure parallel to the surface. Thus, the parallel component of the momentum of the electrons is conserved when they penetrate this barrier. In a standard LEED analysis this barrier is often neglected.

2.1.4 Inner Potential and Inelastic Process

As mentioned above, the inner potential V_0 is approximated as a constant. This, in some sense, is constrained by the fact that exactly describing this potential

is rather difficult. In a standard quantitative LEED analysis, one firstly sets the inner potential to a reasonably guessed value, then it is systematically adjusted in the process of the best-fit search. Since this potential is attractive (negative), it is equivalent to a rigid shift of the incident energy E_p towards the higher energy. Hereafter in this section, $E = E_\mathrm{p} - V_0$ will be adopted.

The inner potential is regarded as mainly contributed by the valence electrons which account for the principal mechanisms of the absorptions of the incident electrons in the surface (e.g., surface plasmon and single-electron excitations). Therefore, it is necessary that the inner potential should incorporate some property of absorbing electrons. In other words, the electron waves must be damping when propagating in the inner potential. In LEED theory, this is achieved phenomenologically by assigning a negative imaginary part to the inner potential so that V_0 is expressible as a complex number, i.e., $V_0 = V_{0\mathrm{r}} + iV_{0\mathrm{i}}$, where both $V_{0\mathrm{r}}$ and $V_{0\mathrm{i}}$ are negative. The effect of the negative imaginary part $V_{0\mathrm{i}}$ can be easily seen. Consider a one-dimensional plane-wave $\boldsymbol{e}^{ikx}$, whose energy E has a positive imaginary part (note that $E = E_\mathrm{p} - V_0$), and express the wavevector by $k = k_\mathrm{r} + ik_\mathrm{i}$. Since $k = \sqrt{2E}$, the imaginary part k_i is positive too. Thus, the electron wave $\boldsymbol{e}^{ikx} = \boldsymbol{e}^{-k_\mathrm{i}x}\boldsymbol{e}^{ik_\mathrm{r}x}$ has a damping factor $\boldsymbol{e}^{-k_\mathrm{i}x}$.

The imaginary part of the inner potential $V_{0\mathrm{i}}$ simulates the absorption processes in the surface, hence decides the inelastic mean free path λ of the incident electrons, which in turn affects the peak widths ΔE in the I-V curves. Therefore, ΔE is a rough indicator of the magnitude of $V_{0\mathrm{i}}$.

In most quantitative LEED analyses, V_0 is kept unchanged throughout the whole energy range. However, it does vary as the incident energy E_p changes. This is because, as E_p increases, the correlation between the incident electrons and the electrons in the surface becomes weakened. Thus, the screening due to the surface electrons is reduced [15]. This makes the incident electron feel more attraction. Therefore, the $V_{0\mathrm{r}}$ normally increases with E_p, especially at high energies, and the change is usually not linear. The energy-dependency of the inner potential for Cu has been studied by Rundgren [18]. Some LEED studies have employed

this potential [19] and it has been shown that the systematic error introduced by non-consideration of the energy-dependency is rather low (0.01 Å) and negligible by today's standards of quantitative LEED analysis [20]. In this thesis, V_0 (both real and imaginary parts) is always taken to be energy-independent.

2.1.5 Ion-core Scattering and Phase Shifts

Consider a beam of electrons with energy E represented by $\boldsymbol{e}^{i\mathbf{kr}}$ incident on an isolated ion-core. This plane-wave can be decomposed into a series of spherical waves by using the expansion

$$\boldsymbol{e}^{i\mathbf{kr}} = \sum_{lm} 4\pi(-1)^m Y_{l\,-m}(\mathbf{k}) i^l j_l(\kappa r) Y_{lm}(\mathbf{r}), \tag{2.1}$$

where each $i^l j_l(\kappa r) Y_{lm}(\mathbf{r})$ is a spherical wave (also known as a partial wave) and $4\pi(-1)^m Y_{l\,-m}(\mathbf{k})$ forms the expansion coefficient. j_l and Y_{lm} are the spherical Bessel functions and the spherical harmonics, respectively, and $\kappa = \sqrt{2E}$. The vector arguments in the spherical harmonics actually stand only for the angular coordinates (i.e., θ and φ) of these vectors. In addition, it should be noted that

$$(-1)^m Y_{l\,-m}(\mathbf{k}) \neq Y^*_{lm}(\mathbf{k}), \tag{2.2}$$

if $\mathbf{k}$ is a complex number, which is the case when the plane-wave travels in the complex inner potential. The multiple scattering theory introduced later is based on the propagation of spherical waves in the surface. With the expansion in Eq. (2.1), the ion-core scattering problem is transformed to one like

$$|l'm'\rangle = \mathbf{t}\,|lm\rangle\,, \tag{2.3}$$

where $|lm\rangle$ and $|l'm'\rangle$ denote two wavefields expressed in the spherical wave representation (or the l-space) and $\mathbf{t}$ is a l-space ion-core scattering matrix which connects the two wavefields.

In the muffin-tin approximation, the ion-core potential is spherically symmet-

ric. Therefore, the angular momentum of each l-component is conserved. In other words, for a spherically symmetric potential, the scattering matrix is diagonal and independent of the magnetic quantum number m. Two causes may break the diagonality of the t-matrix. One is the anisotropic vibrations of the ion-cores at finite temperature as will be discussed in next subsection. Another is the failure of the muffin-tin approximation itself, which still cannot be handled practically in the current LEED theory.

Once the **t**-matrix is known, the ion-core can be treated as a "black box" in any scattering process. Given the muffin-tin potential V_{mt} and the electron energy E, one can solve the radial Schrödinger equation

$$\left[-\frac{1}{2}\frac{d^2}{dr^2}+\frac{l(l+1)}{2r^2}+V_{\mathrm{mt}}(r)\right]u_l(r)=Eu_l(r) \tag{2.4}$$

for the effective radial wavefunctions $u_l(r)$ which is related to the actual radial wavefunctions $\phi_l(r)$ by $u_l(r)=r\phi_l(r)$. Then, the scattering matrix element t_l can be evaluated at the muffin-tin radius R_{mt} by

$$t_l=\frac{1}{2}\left[\frac{L_l(R_{\mathrm{mt}})h_l^*(\kappa R_{\mathrm{mt}})-h_l^{*\prime}(\kappa R_{\mathrm{mt}})}{h_l'(\kappa R_{\mathrm{mt}})-L_l(R_{\mathrm{mt}})h_l(\kappa R_{\mathrm{mt}})}-1\right]=i\boldsymbol{e}^{i\delta_l}\sin\delta_l. \tag{2.5}$$

L_l is the logarithmic derivative defined by

$$L_l(r)\equiv\frac{\phi_l'(r)}{\phi_l(r)}=\frac{u_l'(r)}{u_l(r)}-\frac{1}{r}. \tag{2.6}$$

h_l and h_l^* are the spherical Hankel functions of the first and second kinds, respectively. The t_l are complex numbers. For the sake of convenience, however, each of them can be characterized by a real number δ_l, as given in Eq. (2.5), which has a physical meaning known as the *phase shift*. Normally, when evaluating the **t**-Matrix, the imaginary part of the inner potential is not considered. That is to say, E, hence κ in the Hankel functions, is real. Thus, the Hankel functions of the first and second kinds are the complex conjugates of each other, which ensures that the phase shifts calculated from Eq. (2.5) are real.

2.1.6 Temperature Effect

If the LEED experiment is conducted at a finite temperature, the thermal vibrations of the ion-cores will affect the scattering process. As the sample temperature is increased, the beam intensity becomes weaker, the background is enhanced and the diffraction spots become diffused. In the kinematic limit, the vibrations can be described by Debye-Waller factors as in the case of X-ray diffraction. However, within the framework of the multiple scattering theory, incorporating the thermal effect is much more complicated. Usually, in a standard LEED analysis, only isotropic vibrations are considered, which is also the scheme adopted in this thesis. Nevertheless, attempts to include the anisotropic vibrations in LEED analysis have been made. In the following, a general formalism for treating the harmonic thermal vibrations, as described by Fritzsche [21], is introduced.

A harmonic vibration of an ion-core can always be described by three root-mean-square (rms) vibration amplitudes (μ_x, μ_y and μ_z) along three orthogonal axes (principal axes) of a specific coordinate system. The $\mathbf{t}$-matrix at a finite temperature, denoted by $\mathbf{t}(T)$, can be obtained by a series summation

$$\mathbf{t}(T) = \sum_n \mathbf{t}^{(n)}. \tag{2.7}$$

The $\mathbf{t}^{(n)}$ are given by the recurrence relation

$$\mathbf{t}^{(n+1)} = -\frac{\kappa^2}{2(n+1)} \sum_{\alpha=x,y,z} \mu_\alpha^2 \left[\mathbf{M}^\alpha \mathbf{M}^\alpha \mathbf{t}^{(n)} - 2\mathbf{M}^\alpha \mathbf{t}^{(n)} \mathbf{M}^\alpha + \mathbf{t}^{(n)} \mathbf{M}^\alpha \mathbf{M}^\alpha\right] \tag{2.8}$$

with the starting condition

$$\mathbf{t}^{(0)} = \mathbf{t}(0), \tag{2.9}$$

which is calculated by the method described in the last subsection. The matrices

$\mathbf{M}^{\alpha}$ are given by

$$\mathbf{M}^{z}_{l'm',lm} = i^{l'-l}\sqrt{\frac{4\pi}{3}}\int Y^{*}_{l'm'}Y_{lm}Y_{10}d\Omega, \tag{2.10a}$$

$$\mathbf{M}^{x}_{l'm',lm} = \frac{1}{\sqrt{2}}(\mathbf{M}^{-}_{l'm',lm} - \mathbf{M}^{+}_{l'm',lm}), \tag{2.10b}$$

$$\mathbf{M}^{y}_{l'm',lm} = \frac{i}{\sqrt{2}}(\mathbf{M}^{-}_{l'm',lm} + \mathbf{M}^{+}_{l'm',lm}) \tag{2.10c}$$

with

$$\mathbf{M}^{\pm}_{l'm',lm} = i^{l'-l}\sqrt{\frac{4\pi}{3}}\int Y^{*}_{l'm'}Y_{lm}Y_{1\pm1}d\Omega. \tag{2.11}$$

In the limit of isotropic vibration, it has been shown that the summation in Eq. (2.7) converges to

$$t_l(T) = e^{-\kappa^2\mu^2}\sum_{l'l''} i^{l''}j_{l''}(-i\kappa^2\mu^2)(2l''+1)(2l'+1)\,B^{l''}_{l,l'}\,t_{l'}(0), \tag{2.12}$$

where μ is the rms isotropic vibration amplitude and the coefficients $B^{l''}_{l,l'}$ can be obtained by Adams' formula [22]

$$B^{l''}_{l,l'} = \int_{-1}^{1} P_l(u)P_{l'}(u)P_{l''}(u)du = \frac{2}{2s+1}\frac{A(s-l)A(s-l')A(s-l'')}{A(s)} \tag{2.13}$$

where $P_l(u)$ is the Legendre function, $s = (l+l'+l'')/2$ and $A(n) = \frac{1\cdot3\cdot5\cdots(2n-1)}{1\cdot2\cdot3\cdots n}$ with $A(0) = 1$. Eq. (2.12) is the standard formula in the LEED theory to evaluate the temperature-dependent **t**-matrix. The calculation of non-diagonal **t**-matrix scales as $(l_{max}+1)^6$ [23]. This prohibits the anisotropic vibrations from being incorporated in a practical LEED analysis.

2.1.7 Multiple Scattering Theory

Consider an atomic slab constituted by a lattice of atoms with 2-dimensional periodicity. The k-th atom in the j-th unit cell can be identified by a position vector $\mathbf{R}_j + \mathbf{r}_k$, where $\mathbf{R}_j$ is the origin of the j-th unit cell and $\mathbf{r}_k$ the displacement of the k-th atom relative to $\mathbf{R}_j$. Let $\boldsymbol{e}^{i\mathbf{k}^{+}_{\mathbf{g}}\mathbf{r}}$ and $\boldsymbol{e}^{i\mathbf{k}^{-}_{\mathbf{g}}\mathbf{r}}$ denote the *incoming* plane-waves which are incident on the upper and lower faces of the slab, respectively.

Their amplitudes are represented by $A^+_{\mathbf{g}}$ and $A^-_{\mathbf{g}}$. The wavevectors $\mathbf{k}^+_{\mathbf{g}}$ and $\mathbf{k}^-_{\mathbf{g}}$ are defined by

$$\mathbf{k}^{\pm}_{\mathbf{g}} = \left(\mathbf{k}_{\parallel} + \mathbf{g}, k^{\pm}_{\mathbf{g}z}\right), \tag{2.14a}$$

$$k^{\pm}_{\mathbf{g}z} = \pm\sqrt{2E - \left|\mathbf{k}_{\parallel} + \mathbf{g}\right|^2}, \tag{2.14b}$$

$$\left|k^{\pm}_{\mathbf{g}}\right| = \kappa = \sqrt{2E}, \tag{2.14c}$$

where $\mathbf{k}_{\parallel}$ is the parallel component of the wavevector of the primary electrons and E has been corrected by the complex inner potential, i.e., $E = E_{\mathrm{p}} - V_0$. Similarly, $A^+_{\mathbf{g}'}$ and $A^-_{\mathbf{g}'}$ denote the amplitudes of the *outgoing* plane-waves leaving the slab from the lower and the upper faces, respectively.

The objective of multiple scattering theory is to deduce the reflection matrices ($\boldsymbol{R}^{-+}_{\mathbf{g}'\mathbf{g}}$ and $\boldsymbol{R}^{+-}_{\mathbf{g}'\mathbf{g}}$) and the transmission matrices ($\boldsymbol{T}^{++}_{\mathbf{g}'\mathbf{g}}$ and $\boldsymbol{T}^{--}_{\mathbf{g}'\mathbf{g}}$) of the slab, which connect the incident and scattered plane-waves by

$$A^{\pm}_{\mathbf{g}'} = \sum_{\mathbf{g}} \boldsymbol{M}^{\pm\pm}_{\mathbf{g}'\mathbf{g}} A^{\pm}_{\mathbf{g}}, \tag{2.15}$$

where a unified multiple scattering matrix in the plane-wave representation (or the k-space) $\boldsymbol{M}^{\pm\pm}_{\mathbf{g}'\mathbf{g}}$ has been used to represent the four matrices above by taking note that

$$\boldsymbol{R}^{-+} = \boldsymbol{M}^{-+};\ \boldsymbol{T}^{++} = \boldsymbol{I} + \boldsymbol{M}^{++};\ \boldsymbol{R}^{+-} = \boldsymbol{M}^{+-};\ \boldsymbol{T}^{--} = \boldsymbol{I} + \boldsymbol{M}^{--}. \tag{2.16}$$

$\boldsymbol{I}$ is the unit matrix in the k-space. The superscripts and subscripts in the matrices above should be read from right to left.

According to Pendry [15],

$$\boldsymbol{M}^{\pm\pm}_{\mathbf{g}'\mathbf{g}} = \frac{1}{2i\Omega\left|k^{\pm}_{\mathbf{g}}\right|\left|k^{\pm}_{\mathbf{g}'z}\right|}\mathbf{A}(\mathbf{k}^{\pm}_{\mathbf{g}})\mathbf{T}\mathbf{A}^{\dagger}(\mathbf{k}^{\pm}_{\mathbf{g}'}), \tag{2.17}$$

where Ω is the area of the surface unit cell. $\mathbf{A}(\mathbf{k}^{\pm}_{\mathbf{g}})$, $\mathbf{T}$ and $\mathbf{A}^{\dagger}(\mathbf{k}^{\pm}_{\mathbf{g}'})$ will be described below.

$\mathbf{A}(\mathbf{k})$ is an augmented row vector having the form

$$\mathbf{A}(\mathbf{k}) = \left[\begin{array}{cccc} \mathbf{A}_1(\mathbf{k}) & \mathbf{A}_2(\mathbf{k}) & \cdots & \mathbf{A}_N(\mathbf{k}) \end{array} \right], \tag{2.18}$$

where N is the number of atoms in each unit cell, i.e., the number of single-Bravais-lattice layers in the slab. Each component vector $\mathbf{A}_k(\mathbf{k})$ represents the expansion coefficients of the incident plane-wave $\boldsymbol{e}^{i\mathbf{kr}}$ about the spherical waves centered on $\mathbf{r}_k$ (i.e., the k-th atom in the unit cell *at the origin*). The elements of $\mathbf{A}_k(\mathbf{k})$ are given by

$$A^k_{lm}(\mathbf{k}) = 4\pi(-1)^m Y_{l\,-m}(\mathbf{k})\boldsymbol{e}^{i\mathbf{kr}_k}. \tag{2.19}$$

Eq. (2.1) is used here to obtain this formula. The term $\boldsymbol{e}^{i\mathbf{kr}_k}$ means a propagation of $\boldsymbol{e}^{i\mathbf{kr}}$ from the origin to $\mathbf{r}_k$.

$\mathbf{A}^\dagger(\mathbf{k})$ is similar to $\mathbf{A}(\mathbf{k})$, but a column vector having the form

$$\mathbf{A}^\dagger(\mathbf{k}) = \left[\begin{array}{c} \mathbf{A}^\dagger_1(\mathbf{k}) \\ \mathbf{A}^\dagger_2(\mathbf{k}) \\ \vdots \\ \mathbf{A}^\dagger_N(\mathbf{k}) \end{array} \right]. \tag{2.20}$$

If the wavevector $\mathbf{k}$ is real, $\mathbf{A}^\dagger(\mathbf{k})$ is exactly the conjugate transpose of $\mathbf{A}(\mathbf{k})$. However, as discussed in Section 2.1.4, $\mathbf{k}$ is usually complex. In view of this, the elements of $\mathbf{A}^\dagger_k(\mathbf{k})$ are given by

$$A^{\dagger k}_{lm}(\mathbf{k}) = 4\pi Y_{lm}(\mathbf{k})\boldsymbol{e}^{-i\mathbf{kr}_k}. \tag{2.21}$$

$\mathbf{T}$ is the l-space multiple scattering matrix which can be written as

$$\mathbf{T} = \left[\mathbf{I} - \tau\mathbf{G}\right]^{-1}\tau. \tag{2.22}$$

Here, $\mathbf{I}$ is the unit matrix in the l-space. The matrix τ has the form

$$\tau = \begin{bmatrix} \mathbf{t}_1 & 0 & \cdots & 0 \\ 0 & \mathbf{t}_2 & \cdots & 0 \\ \vdots & \vdots & \ddots & \vdots \\ 0 & 0 & \cdots & \mathbf{t}_N \end{bmatrix} \tag{2.23}$$

with $\mathbf{t}_k$ the $\mathbf{t}$-matrix for the k-th ion-core in the unit cell. The matrix $\mathbf{G}$ includes the propagations of the spherical waves between the ion-cores in the slab, which has the form

$$\mathbf{G} = \begin{bmatrix} \mathbf{G}^{11} & \mathbf{G}^{12} & \cdots & \mathbf{G}^{1N} \\ \mathbf{G}^{21} & \mathbf{G}^{22} & \cdots & \mathbf{G}^{2N} \\ \vdots & \vdots & \ddots & \vdots \\ \mathbf{G}^{N1} & \mathbf{G}^{N2} & \cdots & \mathbf{G}^{NN} \end{bmatrix}. \tag{2.24}$$

The elements of $\mathbf{G}_{kk'}$ are given by

$$G^{kk'}_{lm,l'm'} = {\sum_j}' e^{i\mathbf{k}_\parallel \mathbf{R}_j} \hat{G}^{kk'}_{lm,l'm'}(\mathbf{R}_j), \tag{2.25}$$

$$\hat{G}^{kk'}_{lm,l'm'}(\mathbf{R}_j) = \sum_{l''m''} 4\pi i^{l''} h_{l''}(\kappa|\mathbf{r}_{kk'} - \mathbf{R}_j|) Y^*_{l''m''}(\mathbf{r}_{kk'} - \mathbf{R}_j) C^{l''m''}_{lm,l'm'}, \tag{2.26}$$

where $\mathbf{r}_{kk'} = \mathbf{r}_{k'} - \mathbf{r}_k$ and $C^{l''m''}_{lm,l'm'}$ is a Gaunt coefficient which can be evaluated by

$$C^{l''m''}_{lm,l'm'} = \int Y_{lm} Y_{l''m''} Y^*_{l'm'} d\Omega = \sqrt{\frac{(2l+1)(2l''+1)}{4\pi(2l'+1)}} \hat{C}^{l'0}_{l0,l''0} \hat{C}^{l'm'}_{lm,l''m''}. \tag{2.27}$$

Here, $\hat{C}^{l'm'}_{lm,l''m''}$ is a Clebsch-Gordon coefficient, which can be expressed in a variety of algebraic forms, e.g., the Wigner's formula [24]

$$\begin{aligned} \hat{C}^{c\gamma}_{a\alpha,b\beta} =& \sqrt{\frac{(a+b-c)!(a-b+c)!(-a+b+c)!}{(a+b+c+1)!}} \sqrt{\frac{(c+\gamma)!(c-\gamma)!(2c+1)!}{(a+\alpha)!(a-\alpha)!(b+\beta)!(b-\beta)!}} \\ & \times \sum_z \frac{(-1)^{b+\beta+z}(c+b+\alpha-z)!(a-\alpha+z)!}{z!(c-a+b-z)!(c+\gamma-z)!(a-b-\gamma+z)!}. \end{aligned} \tag{2.28}$$

The prime above the summation symbol in Eq. (2.25) denotes that, if $k = k'$, the point at $\mathbf{R}_j = 0$ will be excluded from the summation.

The number of single-Bravais-lattice layers in the slab N should be large enough for representing the whole surface. This depends on the interlayer spacing and the scattering species. As can be seen from the formalism above, the calculation of the l-space multiple scattering matrix $\mathbf{T}$ involves inverting a matrix of dimension $N(l_{max}+1)^2$, where l_{max} is the largest l-component included in the expansion Eq. (2.1). Therefore, the formalism introduced above is often referred to as the matrix inversion (or giant matrix) method. This method is rather inefficient since the matrix inversion is an $O(N^3)$ operation. For overcoming this difficulty, various k-space methods have been developed, one example being the layer-doubling method.

2.1.8 Layer-doubling Method

Due to the spherical symmetry of the ion-core potentials, it is convenient to treat the inter-atom scatterings in the l-space. However, because the wavefield between two atomic layers is made up of discrete diffraction beams, it is also possible to handle the inter-layer scatterings in the k-space. The layer-doubling method is one of the implementations of the multiple scattering theory in the k-space.

Consider a pair of diffracting layers (A and B), each of which is characterized by four matrices: $\boldsymbol{r}^{-+}$, $\boldsymbol{t}^{++}$, $\boldsymbol{r}^{+-}$ and $\boldsymbol{t}^{--}$. These matrices have the same meaning as in Eq. (2.16). Each layer of A and B can be a single-Bravais-lattice layer or a composite layer (a stack of sub-layers that have the same Bravais lattice). For single-Bravais-lattice layers, one has $\boldsymbol{r}^{-+} = \boldsymbol{r}^{+-}$ and $\boldsymbol{t}^{++} = \boldsymbol{t}^{--}$. For composite layers, however, these equalities rarely hold [16].

The multiple scattering process between the two layers is illustrated in Fig. 2.3. In the following, it will be shown how the total reflection matrix $\boldsymbol{R}^{-+}$ of the double-layer is constructed from the scattering matrices of the component layers (A and B) in the layer-doubling method.

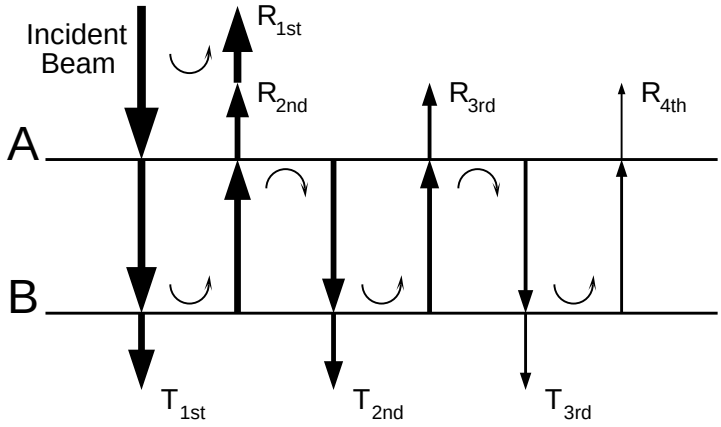

Fig. 2.3: Multiple scattering between a pair of diffraction layers.

From Fig. 2.3, it can be seen that the first order reflection of the double-layer is due to the layer A. This is given by Eq. (2.29a). The second order of the reflection is formed by a transmission through A, a propagation to B, a reflection by B, a propagation to A and a transmission through A. This process is formulated in Eq. (2.29b). (Notice that the formulae should be read from right to left.) In the same manner, the 3rd and 4th orders can be obtained by Eq. (2.29c) and (2.29d) in which one can see that the underlined parts are a repeating block.

$$\boldsymbol{R}^{-+}_{\mathrm{1st}} = \boldsymbol{r}^{-+}_{A} \tag{2.29a}$$

$$\boldsymbol{R}^{-+}_{\mathrm{2nd}} = \boldsymbol{t}^{--}_{A}\, \boldsymbol{P}^{-}\, \boldsymbol{r}^{-+}_{B}\, \boldsymbol{P}^{+}\; \boldsymbol{t}^{++}_{A} \tag{2.29b}$$

$$\boldsymbol{R}^{-+}_{\mathrm{3rd}} = \boldsymbol{t}^{--}_{A}\, \boldsymbol{P}^{-}\, \boldsymbol{r}^{-+}_{B}\, \boldsymbol{P}^{+}\, \underline{\boldsymbol{r}^{+-}_{A}\, \boldsymbol{P}^{-}\, \boldsymbol{r}^{-+}_{B}\, \boldsymbol{P}^{+}}\; \boldsymbol{t}^{++}_{A} \tag{2.29c}$$

$$\boldsymbol{R}^{-+}_{\mathrm{4th}} = \boldsymbol{t}^{--}_{A}\, \boldsymbol{P}^{-}\, \boldsymbol{r}^{-+}_{B}\, \boldsymbol{P}^{+}\, \underline{\boldsymbol{r}^{+-}_{A}\, \boldsymbol{P}^{-}\, \boldsymbol{r}^{-+}_{B}\, \boldsymbol{P}^{+}}\; \underline{\boldsymbol{r}^{+-}_{A}\, \boldsymbol{P}^{-}\, \boldsymbol{r}^{-+}_{B}\, \boldsymbol{P}^{+}}\; \boldsymbol{t}^{++}_{A} \tag{2.29d}$$

If carrying this procedure on to infinite order, one finally obtains a geometric series. Add them together and the total reflection matrix of the double-layer can be expressed as in Eq. (2.30a).

$$\boldsymbol{R}^{-+} = \boldsymbol{r}^{-+}_{A} + \boldsymbol{t}^{--}_{A}\, \boldsymbol{P}^{-}\, \boldsymbol{r}^{-+}_{B}\, \boldsymbol{P}^{+}\, \left(\mathbf{I} - \boldsymbol{r}^{+-}_{A}\, \boldsymbol{P}^{-}\, \boldsymbol{r}^{-+}_{B}\, \boldsymbol{P}^{+}\right)^{-1} \boldsymbol{t}^{++}_{A} \tag{2.30a}$$

$$\boldsymbol{T}^{++} = \boldsymbol{t}^{++}_{B}\, \boldsymbol{P}^{+}\, \left(\mathbf{I} - \boldsymbol{r}^{+-}_{A}\, \boldsymbol{P}^{-}\, \boldsymbol{r}^{-+}_{B}\, \boldsymbol{P}^{+}\right)^{-1} \boldsymbol{t}^{++}_{A} \tag{2.30b}$$

$$\boldsymbol{R}^{+-} = \boldsymbol{r}^{+-}_{B} + \boldsymbol{t}^{++}_{B}\, \boldsymbol{P}^{+}\, \boldsymbol{r}^{+-}_{A}\, \boldsymbol{P}^{-}\, \left(\mathbf{I} - \boldsymbol{r}^{-+}_{B}\, \boldsymbol{P}^{+}\, \boldsymbol{r}^{+-}_{A}\, \boldsymbol{P}^{-}\right)^{-1} \boldsymbol{t}^{--}_{B} \tag{2.30c}$$

$$\boldsymbol{T}^{--} = \boldsymbol{t}^{--}_{A}\, \boldsymbol{P}^{-}\, \left(\mathbf{I} - \boldsymbol{r}^{-+}_{B}\, \boldsymbol{P}^{+}\, \boldsymbol{r}^{+-}_{A}\, \boldsymbol{P}^{-}\right)^{-1} \boldsymbol{t}^{--}_{B} \tag{2.30d}$$

The other diffraction matrices in Eq. (2.30) can be deduced by analogy. The propagators $\boldsymbol{P}^+$ and $\boldsymbol{P}^-$ are diagonal matrices, which are given by

$$\boldsymbol{P}_{\mathbf{g}}^{\pm} = \boldsymbol{e}^{\pm i \mathbf{k}_{\mathbf{g}}^{\pm} \boldsymbol{r}_{BA}}, \tag{2.31}$$

where $\boldsymbol{r}_{BA}$ is a vector connecting the origins of the layers A and B.

Normally, for a substrate calculation, this process can be accelerated by stacking two identical slabs consisting of 2^{n-1} layers into one consisting of 2^n layers at the n-th iteration, for which the layer-doubling method is named. Thus, four or five iterations are usually sufficient to converge the substrate calculation. However, at surfaces, stacking has to be done layer by layer, since the interlayer spacings there change from layer to layer due to relaxation. The number of surface layers depends on the system studied. For high-index metal surfaces, at least three surface layers should be allowed to relax.

From the formalism above, it can be seen that the matrices to be manipulated in an $O(N^3)$ way (i.e., multiplications and inversions) have a dimension of N_b, which can be evaluated by

$$N_b = \frac{\Omega}{4\pi}[2E + (\frac{\ln t}{d})^2]. \tag{2.32}$$

The second term accounts for those plane waves that decay away when propagating from one layer to the next, i.e., the so-called evanescent waves [16], where d is the interlayer spacing and t a user-input dimensionless quantity which serves as the beam cutoff criterion. Typical values of N_b are from 100 to 200. These are much smaller than the size of the matrices in the matrix inversion method (typically greater than 1000). Hence, the layer-doubling method is much more efficient.

2.1.9 Reliability Factors

As has been mentioned, a quantitative LEED analysis is carried out by systematically searching for the surface structure which gives the best fit between the calculated and experimental I-V curves. Therefore, there must be a measurement

that can quantify the agreement between the two sets of curves. This is achieved by defining a quantity called the *reliablity factor* (or R-factor). Various definitions exist in the literature [25–28]. In this thesis, Pendry's definition is employed [27]. The Pendry R-factor (R_{P}) is designed to be sensitive mainly to the peak positions, rather than the absolute intensities. It equally weights the strong and weak peaks. This design is preferred for high index surfaces since weak peaks (or even long flat regions) due to multiple scatterings dominate the I-V curves.

The Pendry's procedure starts from the definition of function $Y(E)$ by

$$Y(E) = \frac{L(E)}{1 + L^2(E)V_{0\mathrm{i}}^2}, \tag{2.33}$$

where $L(E)$ is the logarithmic derivative of the I-V curves given by

$$L(E) = \frac{I'(E)}{I(E)}. \tag{2.34}$$

Then the Pendry R-factor is defined by

$$R_{\mathrm{P}} = \frac{\int (Y_{\mathrm{exp}} - Y_{\mathrm{cal}})^2 dE}{\int (Y_{\mathrm{exp}}^2 + Y_{\mathrm{exp}}^2) dE}. \tag{2.35}$$

In this approach, the variation of R_{P} or the statistical error can be estimated by

$$\mathrm{var}(R_{\mathrm{P}}) = \min(R_{\mathrm{P}}) \sqrt{\frac{8\,|V_{0\mathrm{i}}|}{\Delta E}}, \tag{2.36}$$

where ΔE is the total energy range of the I-V curves. With this quantity, the error bars for the structural parameters determined can be estimated [27].

2.1.10 Best-fit Search and Tensor LEED

Quantitative LEED analysis is actually an optimization problem, where the R-factor is taken as the cost function (or objective function) whose minimum is sought within the hyperspace spanned by the structural and non-structural parameters. The computing time to perform an exhaustive search through the parameter space scales exponentially as the number of parameters. Therefore,

one has to employ a more efficient algorithm to find the minimum of the R-factor.

The most conventional algorithm is to convert the multi-dimensional search into a sequence of one-dimensional searches. Starting from a certain parameter (often the one to which the R-factor is most sensitive), one first fixes all other parameters and performs a one-dimensional optimization. Then, the current parameter is fixed and the search changes to the next parameter. This procedure is repeated until the minimum is reached. This algorithm, hereafter referred to as conventional grid search algorithm, is also adopted in this thesis due to its simplicity. Often, whenever a change is made to the current parameter, the already-fixed parameters need to be checked if they are affected by the current change. This is expected to be very inefficient if the number of parameters is large and the correlation between the parameters is strong. However, for the cases involved in this thesis, it is still affordable.

Many other algorithms exist for multivariable optimization. One category of these algorithms is the steepest descent approaches which direct the search by using the gradient of the R-factor [29]. A more robust (but sometimes less efficient) algorithm is the simplex method [29]. In this method, there is no need for the calculation of the gradient of the R-factor, which is sensitive to the experimental noise and the truncation errors in the computation. These algorithms as well as the conventional grid search algorithm suffer the problem that they can be easily trapped in a local, rather than the global, minimum in the parameter space. To overcome this difficulty, global minimization algorithms such as simulated annealing [30], genetic algorithm [31] and their variants [32] have been introduced. In principle, these algorithms guarantee the global minimum only when the searched number of grid points approaches infinity. In practice, multi-starting searches are done to confirm the global minimum, especially when the best-fit R-factor achieved is rather poor, e.g., larger than 0.25 if the R_{P} is used.

A breakthrough in quantitative LEED analysis is tensor LEED theory [33]. The idea of this theory is that the full-dynamical LEED calculation is only necessary for a so-called *reference structure*, while for the trial structures in its vicinity

the LEED intensities can be obtained by the perturbative method. The tensor LEED scheme can significantly speed up the structure determination compared to conventional LEED analysis.

If a trial structure is characterized by a set of displacements $\{\delta\mathbf{r}_k\}$ with respect to the reference structure, the scattering from the trial structure is equivalent to that from the reference structure except that the $\mathbf{t}$-matrices of the displaced atoms are replaced by the renormalized $\mathbf{t}$-matrices

$$\mathbf{t}'_k = \mathbf{t}_k + \delta\mathbf{t}_k(\delta\mathbf{r}_k). \tag{2.37}$$

Note that $\delta\mathbf{t}_k$ are usually non-diagonal. By substituting the $\mathbf{t}'_k$ into the formalism introduced in Section 2.1.7 and neglecting all propagation paths where $\delta\mathbf{t}_k$ occur more than once (i.e., to the first order approximation), the difference between the amplitudes of diffraction beam $\mathbf{k}^-_{\mathbf{g}'}$ from the reference and the trial structures, denoted by $\delta A^-_{\mathbf{g}'}$, can be expressed by

$$\delta A_{\mathbf{g}'} = \frac{1}{2i\Omega\kappa k^+_{\mathbf{g}'z}} \sum_k \mathcal{A}_k(-\mathbf{k}^+_{\mathbf{g}})\delta\mathbf{t}_k\mathcal{A}^\dagger_k(\mathbf{k}^+_0). \tag{2.38}$$

The evaluation of $\mathcal{A}_k(-\mathbf{k}^+_{\mathbf{g}})$ and $\mathcal{A}^\dagger_k(\mathbf{k}^+_0)$ still requires full-dynamical calculations. However, this can be done once and for all in the reference structure calculation since they are independent of $\{\delta\mathbf{r}_k\}$. Therefore, one can gain a great performance improvement in structure determination using the tensor LEED scheme.

The implementation of tensor LEED in the matrix inversion method is straightforward. However, for the layer-doubling method, it is delayed until a very recent article [34]. To date, few surfaces have been studied by the layer-doubling tensor LEED scheme. In this thesis, conventional LEED analysis is still adopted. Normally, the error bars of a conventional LEED analysis are slightly smaller than in a tensor LEED analysis [35] since the I-V curves from the structures in the vicinity of the best-fit structure are calculated fully dynamically.

2.2 First-principles Calculations

First-principles or *ab initio* calculations refer to calculations that do not rely on any adjustable parameters. State-of-the-art methods for conducting first-principles studies on materials properties and processes are based on density functional theory. In this section, a brief introduction to density functional theory and techniques for implementing this theory will be given.

2.2.1 Density Functional Theory

In terms of quantum mechanics, a system comprising N electrons and M nuclei is described by a Hamiltonian $\mathcal{H}$ as:

$$\mathcal{H} = -\frac{1}{2}\sum_{i=1}^{N}\nabla_i^2 + \sum_{i<j}^{N}\frac{1}{|\mathbf{r}_i - \mathbf{r}_j|} + \sum_{i=1}^{N}\sum_{I=1}^{M}\frac{Z_I}{|\mathbf{r}_i - \mathbf{R}_I|} - \frac{1}{2}\sum_{I=1}^{M}\nabla_I^2 + \sum_{I<J}^{M}\frac{Z_I Z_J}{|\mathbf{R}_I - \mathbf{R}_J|}, \quad (2.39)$$

where Z denotes the nuclear charge. Exactly solving a Schrödinger equation with such a many-body Hamiltonian is only possible in principle. For any practical system, one has to resort to approximations. First of all, by the Born-Oppenheimer (or adiabatic) approximation one drops the last two terms in the Hamiltonian above and treats the nuclei separately. The grounds for this treatment are that the nuclei are much heavier, hence move much slower than the electrons. In this approximation, the kinetic energy of the nuclei is neglected and the interaction between the nuclei is handled classically. Thus, the original problem in Eq. (2.39) is reduced to one regarding a system of interacting electrons moving in an external potential, $V(\mathbf{r})$, formed by a frozen-in ionic configuration. For such an inhomogeneous system of interacting electrons, Hohenberg and Kohn [36] proved two theorems with regard to the electron density function $\rho(\mathbf{r})$:

Theorem I If the number of electrons in the system is conserved, the external potential $V(\mathbf{r})$ uniquely determines the ground state density $\rho_0(\mathbf{r})$.

Theorem II There exists a universal energy functional of ρ, $E[\rho]$, which is minimized by the ground state density ρ_0.

These two theorems form the basis of density functional theory.

Kohn and Sham [37] carried this theory further and obtained a single-particle Schrödinger equation,

$$\left\{-\frac{1}{2}\nabla^2 + \int \frac{\rho(\mathbf{r}')}{|\mathbf{r}-\mathbf{r}'|}d^3\mathbf{r}' + \frac{\delta E_{\mathrm{xc}}[\rho(\mathbf{r})]}{\delta\rho(\mathbf{r})} + V(\mathbf{r})\right\}\psi_i(\mathbf{r}) = \varepsilon_i\psi_i(\mathbf{r}), \tag{2.40}$$

which is usually referred to as the Kohn-Sham equation in the literature. The Kohn-Sham equation maps a many-electron interacting system onto a single-electron system within an effective potential formed by the nuclei and other electrons. The first term in the Kohn-Sham Hamiltonian accounts for the kinetic energy and the following three terms are the Coulomb (or Hartree), the exchange-correlation (xc) and the external (e.g., the ionic) potentials, respectively. Comparing with the many-body Hamiltonian in Eq. (2.39), solving the Kohn-Sham equation is much easier for a practical system. Nowadays, even a system consisting of several hundred atoms can be handled with density functional theory.

Due to the fact that the potential and the charge density depend on each other, the Kohn-Sham equation has to be solved self-consistently. Starting from an assumed density $\rho(\mathbf{r})$, one first calculates the Coulomb and xc potentials, then solves Eq. (2.40) for the Kohn-Sham orbitals $\psi_i(\mathbf{r})$. With these orbitals, a new density can be constructed by

$$\rho(\mathbf{r}) = \sum_i |\psi_i(\mathbf{r})|^2, \tag{2.41}$$

where the index i goes over all occupied orbitals. This procedure is repeated until self-consistency (i.e., consistency between the output and input densities) is achieved.

2.2.2 Exchange-correlation Functional

The formalism of the Kohn-Sham equation is much simpler than that of other first-principles methods, such as the Hartree-Fock method where the exchange effect is treated exactly by a complicated manipulation of the wavefunctions. Un-

fortunately, for an inhomogeneous electron gas system, the explicit form of the xc functional $E_{\rm xc}[\rho(\mathbf{r})]$ in the Kohn-Sham equation is unknown and the xc energy is usually a significant part in the total energy of a system. Various approximations to the xc functional have to be made. The simplest one is the local density approximation (LDA) [37], which assumes that, for a system with slowly varying density, the electron density in a small region near point $\mathbf{r}$ can be treated as if it is homogeneous. Thus, the xc functional can be written as

$$E_{\rm xc}[\rho(\mathbf{r})] = \int \epsilon_{\rm xc}(\mathbf{r})\rho(\mathbf{r})d^3\mathbf{r}, \tag{2.42}$$

where $\epsilon_{\rm xc}(\mathbf{r})$ is the xc energy per electron. Despite neglecting the inhomogeneity near point $\mathbf{r}$, the LDA gives remarkably good results when calculating the properties for both isolated (e.g., atoms and molecules) and extended (e.g., solids) systems.

Another promising approximation is the generalized gradient approximation (GGA), which has a form like

$$E_{\rm xc}[\rho] = \int f(\rho, \nabla\rho)d^3\mathbf{r}. \tag{2.43}$$

A variety of choices for $f(\rho, \nabla\rho)$ can be made [38–40]. They usually give an overall improvement on the energetic properties, such as the adsorption energies of molecules on surfaces, over the LDA.

2.2.3 Bloch Theorem and Supercell Approximation

Bloch theorem states that, for a system of electrons moving in a periodic potential, each wavefunction has the form,

$$\psi_{\mathbf{k}}(\mathbf{r}) = e^{i\,\mathbf{kr}}u_{\mathbf{k}}(\mathbf{r}), \tag{2.44}$$

where $u_{\mathbf{k}}(\mathbf{r})$ has the same periodicity as the potential. In a crystal lattice potential, it satisfies

$$u_{\mathbf{k}}(\mathbf{r}+\mathbf{R}) = u_{\mathbf{k}}(\mathbf{r}), \tag{2.45}$$

where $\mathbf{R}$ is a real space lattice vector.

The wavevector $\mathbf{k}$ can always be confined in the first Brillouin zone (1BZ) in the context of band-structure and total-energy calculations since the electron energy is periodic in the $\mathbf{k}$-space and each $\mathbf{k}$-point outside the 1BZ can be mapped onto a $\mathbf{k}$-point inside. The number of $\mathbf{k}$-points in the 1BZ is equal to the number of unit cells in real space. Since this number is in the magnitude of 10^{22}, the $\mathbf{k}$-points in the 1BZ are quasi-continuous.

Many systems of interest do not possess periodicity along all three dimensions. For example, a surface system is only periodic in the plane parallel to the surface; a carbon-nano-tube has only a 1-dimensional periodicity and an isolated atom or molecule is completely aperiodic. To study these systems, two approximations are available. One is to model the system by a cluster of atoms which do not employ any periodicity. Another is to artificially impose a periodicity on the aperiodic dimension(s) represented by a so-called *supercell*.

For a surface system, the supercell approximation is implemented by modeling the surface by periodically arranged slabs which are separated by vacuum layers. A vacuum layer, which is typically 10 Å, prevents the interaction and charge transfer between two slabs. The thickness of the slabs depends on the system under study. Normally, the smaller the interlayer spacing, the thicker the slabs.

2.2.4 Plane-waves and Pseudopotentials

The Kohn-Sham equation is normally solved in the reciprocal space although attempts to solve it in real space are also in progress [41]. This means that one has to employ some kind of basis functions to expand the Kohn-Sham orbitals. In terms of the basis set used, there are many methods for solving the Kohn-Sham equation, such as the LAPW, LMTO and LCAO. The most straightforward choice is to use plane-waves. The plane-wave method has several advantages. Firstly, the

simple mathematical formalism makes it easy to implement this method in a computer program and complex algorithms, such as the Car-Parrinello approach [42], can be easily incorporated. Secondly, the basis set itself is independent of the ion-core positions, which is suitable for surface structures where large relaxations are normally involved in the calculations. Thirdly, the fast Fourier transform algorithm [29] can significantly facilitate the transformation between reciprocal and real spaces. Other advantages of the plane-wave method can also be seen in the following subsections (e.g., in the calculation of the forces).

As can be seen in Eq. (2.45), the Bloch wave has the periodicity of the crystal lattice. Therefore, the crystal wavefunctions can be readily expanded by plane-waves having the same periodicity,

$$\psi_{n,\mathbf{k}}(\mathbf{r}) = \sum_{\mathbf{G}} c^{\mathbf{k}}_{n,\mathbf{G}}\, e^{i\,(\mathbf{k}+\mathbf{G})\cdot\mathbf{r}}. \tag{2.46}$$

Each plane-wave in the expansion corresponds to a reciprocal space lattice vector $\mathbf{G}$, which satisfies $\mathbf{G}\cdot\mathbf{R} = 2\pi m$ (m is an integer). Since the Kohn-Sham equation has many eigenvalues at each $\mathbf{k}$-point, an auxiliary index n (i.e., the band index) has been used to label the wavefunctions. The expansion coefficients $c^{\mathbf{k}}_{n,\mathbf{G}}$ are the unknowns that one needs to solve for.

With the plane-wave expansion, at each $\mathbf{k}$-point one has the secular equation

$$\begin{bmatrix} \mathbf{H}^{\mathbf{k}}_{\mathbf{G}_1,\mathbf{G}_1} & \mathbf{H}^{\mathbf{k}}_{\mathbf{G}_1,\mathbf{G}_2} & \cdots & \mathbf{H}^{\mathbf{k}}_{\mathbf{G}_1,\mathbf{G}_{\max}} \\ \mathbf{H}^{\mathbf{k}}_{\mathbf{G}_2,\mathbf{G}_1} & \mathbf{H}^{\mathbf{k}}_{\mathbf{G}_2,\mathbf{G}_2} & \cdots & \mathbf{H}^{\mathbf{k}}_{\mathbf{G}_2,\mathbf{G}_{\max}} \\ \vdots & \vdots & \ddots & \vdots \\ \mathbf{H}^{\mathbf{k}}_{\mathbf{G}_{\max},\mathbf{G}_1} & \mathbf{H}^{\mathbf{k}}_{\mathbf{G}_{\max},\mathbf{G}_2} & \cdots & \mathbf{H}^{\mathbf{k}}_{\mathbf{G}_{\max},\mathbf{G}_{\max}} \end{bmatrix} \begin{bmatrix} c^{\mathbf{k}}_{n,\mathbf{G}_1} \\ c^{\mathbf{k}}_{n,\mathbf{G}_2} \\ \vdots \\ c^{\mathbf{k}}_{n,\mathbf{G}_{\max}} \end{bmatrix} = \varepsilon^{\mathbf{k}}_n \begin{bmatrix} c^{\mathbf{k}}_{n,\mathbf{G}_1} \\ c^{\mathbf{k}}_{n,\mathbf{G}_2} \\ \vdots \\ c^{\mathbf{k}}_{n,\mathbf{G}_{\max}} \end{bmatrix}, \tag{2.47}$$

where the Hamiltonian matrix elements $\mathbf{H}^{\mathbf{k}}_{\mathbf{G},\mathbf{G}'}$ are obtained by the Fourier transforms of the corresponding terms in the Kohn-Sham equation. For example, the kinetic term can be written as

$$\left\langle \mathbf{k}+\mathbf{G}' \left| -\frac{1}{2}\nabla^2 \right| \mathbf{k}+\mathbf{G} \right\rangle = -\frac{1}{2}|\mathbf{k}+\mathbf{G}|^2 \delta_{\mathbf{G}\mathbf{G}'}, \tag{2.48}$$

which is diagonal. The non-diagonal elements are contributed by the sum of the Hartree, xc and ionic terms.

The size of the Hamiltonian matrix, i.e., the number of plane-waves N_{pw} used in the expansion, is determined by the cutoff energy $\frac{1}{2}|\mathbf{k}+\mathbf{G}_{\mathrm{max}}|^2$, which is denoted by $\mathrm{E_{cut}}$. Due to the nature of the fast oscillation of the core-electron wavefunctions, an extremely large N_{pw} is required to expand the core wavefunctions. Therefore, to apply the plane-wave method, the pseudopotential approximation is necessary [43]. In this approximation, it is firstly assumed that, when putting atoms together to form molecules and solids, the core-electron wavefunctions do not overlap. Thus, the core-electrons can be separated from the electronic system to form the ion-core potential together with the nuclei. Even by doing so, the real valence-electron wavefunctions still oscillate too much to be expanded by a reasonably sized plane-wave basis set. Hence, the real ion-core potential is further replaced by a pseudopotential, which possesses at least the following two properties:

- The valence eigenvalues as obtained from an all-electron calculation can be reproduced by the pseudopotential.
- The pseudo wavefunctions $\phi_{n,\mathbf{k}}(\mathbf{r})$ (i.e., the eigenfunctions of the pseudopotential) and the real wavefunctions $\psi_{n,\mathbf{k}}(\mathbf{r})$ match beyond a chosen core radius r_c.

The pseudopotentials are usually generated from isolated atoms or ions, but can be used in other chemical environments, such as solids. This property is referred to as the *transferability* of the pseudopotentials. Generally speaking, the smaller the core radius r_c, the better the transferability of the pseudopotentials, but the larger the $\mathrm{E_{cut}}$ needed.

For improving the transferability, the norm-conserving condition [44]

$$\int_0^{r_c} |\phi_{n,\mathbf{k}}(\mathbf{r})|^2 d^3\mathbf{r} = \int_0^{r_c} |\psi_{n,\mathbf{k}}(\mathbf{r})|^2 d^3\mathbf{r} \tag{2.49}$$

should normally be fulfilled. The scattering properties of the real ion-core potential

should also be preserved. In other words, the logarithmic derivatives, hence the phase shifts, of the real and pseudo wavefunctions agree beyond r_c. Since the phase shifts produced by the ion-core is different for each angular momentum (l-) component of the valence wavefunction, the pseudopotentials are intrinsically non-local, i.e., different pseudopotentials should be used for different l-components. Formally, a non-local pseudopotential can be written as

$$V_{\text{nloc}} = \sum_l V_l(r)\hat{P}_l, \tag{2.50}$$

where $\hat{P}_l$ is a projection operator on the l-component. This form means that a wavefunction is firstly decomposed into l-components, each of which is then acted by the corresponding $V_l(r)$. A classical assembly of pseudopotentials of this form is provided by Bachelet *et al.* for almost all elements in the periodic table [45]. As pointed out by Kleinman and Bylander [46], these pseudopotentials are still semi-local (non-local in the angular coordinates only) and can be further transformed into a fully non-local separable form

$$V_{\text{NL}} = \sum_{lm} \frac{|\delta V_l \phi_{lm}\rangle \langle \phi_{lm} \delta V_l|}{\langle \phi_{lm}| \delta V_l |\phi_{lm}\rangle} \tag{2.51}$$

with $\delta V_l = V_l(r) + V_{\text{arb}}$ and V_{arb} an arbitrary function (which needs careful selection for obtaining a high quality pseudopotential). The K-B type pseudopotentials are more efficient than the semi-local form since they reduce the number of projections in Eq. (2.50), which are involved in setting up the Hamiltonian matrix elements, from $O(N_{\text{pw}}^2)$ to $O(N_{\text{pw}})$.

The norm-conserving pseudopotentials (NCPP) enjoyed great success in calculating the solid-state properties. However, applying this approach to systems containing the first-row and transition metal elements was hindered in the past because the highly localized valence orbitals in these elements, such as the $2p$ of first-row elements and the d-band of transition metals, are difficult to represent by plane-waves in a NCPP scheme. Fortunately, this difficulty has been overcome by introducing the so-called ultrasoft pseudopotentials (USPP) [47]. Since this thesis

focuses on transition metals that have to be handled by the USPP, the formalism of this approach will be introduced in the next subsection.

2.2.5 Ultrasoft Pseudopotentials

In Vanderbilt's formalism [47], it is also intended to generate a K-B type pseudopotential with a fully non-local separable form. Instead of basing on the semi-local pseudopotentials as proposed by Kleinman and Bylander, the construction of a USPP starts from direct manipulation on the pseudo wavefunctions ϕ_i. The main difference is that the constraint of norm-conserving is removed so that the pseudo wavefunctions can be constructed as soft as possible. This treatment introduces many complications to the mathematical formalism, hence the programming efforts, compared with using a NCPP. However, as a compensation, the cutoff energy E_{cut} can be significantly reduced.

Since the pseudo and real wavefunctions match beyond r_c, while the norm-conserving condition is not satisfied, the pseudo wavefunctions are no longer normalized and the orthonormality condition has to be replaced by

$$\langle \phi_i | \, \mathbf{S} \, | \phi_j \rangle = \delta_{ij} \tag{2.52}$$

introducing the overlap operator

$$\mathbf{S} = 1 + \sum_I \sum_{n,m} q^I_{nm} \left| \beta^I_n \right\rangle \left\langle \beta^I_m \right| \tag{2.53}$$

where

$$q^I_{nm} = \int Q^I_{nm}(\mathbf{r}) d^3\mathbf{r} \tag{2.54}$$

and I is the ion index. As an effect, the pseudo valence charge density cannot be simply calculated by Eq. (2.41). An extra term

$$\sum_i \sum_I \sum_{nm} Q^I_{nm}(\mathbf{r}) \langle \phi_i | \beta^I_n \rangle \langle \beta^I_n | \phi_i \rangle \tag{2.55}$$

accounting for the augmentation charge in the core region has to be added.

Finally, one is confronted with a generalized eigenvalue problem [48]

$$\mathbf{H}\left|\phi_{n,\mathbf{k}}\right\rangle = \varepsilon_{n,\mathbf{k}}\mathbf{S}\left|\phi_{n,\mathbf{k}}\right\rangle, \tag{2.56}$$

where

$$\mathbf{H} = -\frac{1}{2}\nabla^2 + V_{\text{eff}} + \sum_I \sum_{nm} D^I_{nm}|\beta^I_n\rangle\langle\beta^I_n|. \tag{2.57}$$

Here,

$$V_{\text{eff}}(\mathbf{r}) = V_{\text{loc}}(\mathbf{r}) + \int \frac{\rho(\mathbf{r}')}{|\mathbf{r}-\mathbf{r}'|}d^3\mathbf{r}' + \frac{\delta E_{\text{xc}}[\rho(\mathbf{r})]}{\delta\rho(\mathbf{r})} \tag{2.58}$$

is the screened effective potential and

$$D^I_{nm} = D^{I,(0)}_{nm} + \int V_{\text{eff}}(\mathbf{r})Q^I_{nm}(\mathbf{r})d^3\mathbf{r}. \tag{2.59}$$

The quantities V_{loc}, Q, $D^{(0)}$ and β in the preceding equations above characterize a USPP and should be generated when creating it.

The transferability of a USPP can be systematically improved with arbitrary accuracy by increasing the number of reference energies at which the scattering properties of the all-electron potential are preserved. Practically, at most two such reference energies are sufficient to generate an accurate USPP.

Since there is no rigorous rule on how to setup the construction parameters of a USPP, generating a USPP is still more an art than a routine technique. Caution should be given to generate a widely-applicable USPP, such as avoiding the so-called ghost-state (i.e., a state with nodes in the core region and unphysically low energy). In this thesis, it is not intended to generate the USPP's involved. Instead, the USPP's delivered with the package which have been extensively tested will be used.

2.2.6 k-point Sampling

Many calculations in periodic structures involve averaging a function of $\mathbf{k}$, $f(\mathbf{k})$, over the 1BZ. For example, the expression for the valence electron density

in Eq. (2.41) should be replaced by

$$\rho(\mathbf{r}) = \frac{\Omega}{(2\pi)^3} \int_{1BZ} \rho_{\mathbf{k}}(\mathbf{r}) d^3\mathbf{k} \tag{2.60}$$

with

$$\rho_{\mathbf{k}}(\mathbf{r}) = \sum_n |\psi_{n,\mathbf{k}}(\mathbf{r})|^2 \tag{2.61}$$

for a periodic system. Again, the band index n goes over all occupied bands at a specific $\mathbf{k}$-point. Ω is the volume of the real space unit cell.

As stated in Section 2.2.3, the $\mathbf{k}$-points in the 1BZ are quasi-continuous. Carrying out numerical integration like Eq. (2.60) is practically impossible due to the unaffordable computational resources required. If there is a mean-value point $\mathbf{k}_0$, which satisfies $\overline{f} = f(\mathbf{k}_0)$, the problem will become simple. But, such a point does not in fact exist [49]. Nevertheless, the integration can always be estimated by sampling the 1BZ using a set of special $\mathbf{k}$-points. A good property of the $\mathbf{k}$-point sampling technique is that the calculated physical quantities, such as the total energy, of a system always converge with the number of $\mathbf{k}$-points increasing.

Various schemes for generating a sampling $\mathbf{k}$-point set have been developed [49, 50]. The most commonly used is due to Monkhorst and Pack [50]. In this scheme, a grid of $(N_1 \times N_2 \times N_3)$ $\mathbf{k}$-points are defined in the 1BZ by

$$\mathbf{k}_{lmn} = u_l \mathbf{b}_1 + u_m \mathbf{b}_2 + u_n \mathbf{b}_3 \tag{2.62}$$

with

$$\begin{aligned} u_l &= (2l - N_1 - 1)/2N_1 \qquad (l \in [1, N_1]); \\ u_m &= (2m - N_2 - 1)/2N_2 \qquad (m \in [1, N_2]); \\ u_n &= (2n - N_3 - 1)/2N_3 \qquad (n \in [1, N_3]), \end{aligned} \tag{2.63}$$

where $\mathbf{b}_1$, $\mathbf{b}_2$ and $\mathbf{b}_3$ are the basis vectors of the reciprocal lattice. All these $\mathbf{k}$-points are equally weighted. However, by applying the point group symmetry of the unit cell, the number of $\mathbf{k}$-points can be reduced to form an irreducible $\mathbf{k}$-point set in which each $\mathbf{k}$-point represents a $\mathbf{k}$-star [1] in the original set. Because

[1] A set of symmetry-equivalent $\mathbf{k}$-points.

the number of **k**-points in each star may be different from that in another, the **k**-points in the irreducible set normally have different weights. Finally, one has a solution for the 1BZ integration like

$$\overline{f} = \int_{1BZ} f(\mathbf{k}) d^3\mathbf{k} = \sum_{i=1}^{N_k} w_i f(\mathbf{k}_i), \tag{2.64}$$

where the weights satisfy

$$\sum_{i=1}^{N_k} w_i = 1 \tag{2.65}$$

and N_k is the number of irreducible **k**-points.

2.2.7 Metallic System and Smearing Method

At absolute zero point, the band structure energy (a portion of the total-energy) is defined as

$$\frac{\Omega}{(2\pi)^3} \sum_n \int_{1BZ} \varepsilon_{n,\mathbf{k}} \delta(\varepsilon_{n,\mathbf{k}} - E_{\mathrm{F}}) d^3\mathbf{k}, \tag{2.66}$$

where E_{F} is the Fermi energy and

$$\delta(\varepsilon_{n,\mathbf{k}} - E_{\mathrm{F}}) = \begin{cases} 1 & \text{if } \varepsilon_{n,\mathbf{k}} \leq E_{\mathrm{F}} \\ 0 & \text{if } \varepsilon_{n,\mathbf{k}} \geq E_{\mathrm{F}} \end{cases} \tag{2.67}$$

As discussed in the last subsection, this integration has to be carried out by sampling the 1BZ using a set of special **k**-points. For semiconducting and insulating systems, there is no discontinuity in the occupancy, i.e., for all occupied bands, at all **k**-points the occupancies are exactly 2. However, for metallic systems, the occupancies jump from 2 to 0 at the Fermi level. That is, for the same band, at different **k**-points the occupancies may be different. This causes the convergence of the integration against the number of sampling **k**-points to be much slower.

A solution for this difficulty is to replace the step function in the integral by a smoothly varying function $f(\frac{\varepsilon_{n,\mathbf{k}} - E_{\mathrm{F}}}{\sigma})$. A smearing energy σ is introduced

here, which is related to the smearing temperature [2] by $\sigma = k_B T$. With this replacement, the total energy minimum is no longer located at the electronic ground state. Instead, a generalized free-energy functional

$$F(\sigma) = E(\sigma) - \sum_n \sigma S(\frac{\varepsilon_{n,\mathbf{k}} - E_\mathrm{F}}{\sigma}) \tag{2.68}$$

replaces the total-energy functional as the variational quantity, where S is a generalized entropy term due to the elevated temperature.

In the scheme of Methfessel and Paxton [51], the N-th order smearing function and its corresponding entropy term are expressed as

$$f_N(x) = \frac{1 - \mathrm{erf}(x)}{2} + \sum_{m=1}^{N} A_m H_{2m-1}(x) e^{-x^2} \tag{2.69}$$

and

$$S_N(x) = \frac{1}{2} A_N H_{2N}(x) e^{-x^2} \tag{2.70}$$

with

$$x = \frac{\varepsilon_{n,\mathbf{k}} - E_\mathrm{F}}{\sigma} \tag{2.71}$$

and $H(x)$ the Hermite polynomials.

With the smearing method, the number of $\mathbf{k}$-points can be significantly reduced by a carefully selected smearing energy (typically 0.1 – 1.0 eV depending on the DOS structure near the Fermi level). The total energy at zero temperature can be obtained by extrapolating to $\sigma = 0$ according to the relation

$$E_{\sigma=0} = \frac{1}{N+2}[(N+1)F(\sigma) + E(\sigma)]. \tag{2.72}$$

Note that the Gaussian smearing is the zeroth order approximation of Methfessel-Paxton method. For higher orders, unphysical negative occupancies may occur.

[2] Only when the smearing function is the Fermi-Dirac distribution does the "temperature" have a physical meaning.

2.2.8 Iterative Methods for Eigenproblems

The eigenproblem in Eq. (2.47) is traditionally solved by direct diagonalization methods, such as the Choleski-Householder algorithm [29]. In terms of computational effort, however, these methods have two drawbacks:

- The computation time for direct diagonalization of an $(N_{\mathrm{pw}} \times N_{\mathrm{pw}})$ matrix scales as N_{pw}^3 and is independent of the number of eigenvalues sought since direct diagonalization methods obtain all N_{pw} eigenvalues at the same time even though only the lowest N_{band} eigenvalues are required. (Normally, $N_{\mathrm{band}} \ll N_{\mathrm{pw}}$.)

- The direct diagonalization methods need much non-sequential access to both the Hamiltonian and overlap matrices. This property causes the "cache thrashing" effect [52] which is one of the main issues in high-performance computing.

With recent studies concentrating more and more on large systems, these drawbacks become more severe. The iterative methods, in this context, become more and more appealing due to the contrary properties they possess:

- The computation time scales as N_{pw}^2 with a coefficient equal to the number of iterations N_{iter} needed for convergence. ($N_{\mathrm{iter}} \ll N_{\mathrm{pw}}$)

- The iterative methods mainly rely on sequential access to the Hamiltonian and overlap matrices.

- Only the lowest N_{band} eigenvalues that are required and the corresponding eigenfunctions are solved for.

Nowadays, all state-of-the-art computer program packages for first-principles calculations employ some kind of iterative method for the eigenvalue problem.

In this thesis, the residual minimization method with direct inversion in the iterative subspace (RMM-DIIS) [53] is used throughout. For very large systems, the RMM-DIIS is superior to other iterative algorithms in terms of performance (see VASP manual). A brief introduction to this algorithm is given below.

The RMM-DIIS includes three steps: initialization, preconditioning and correction, where the latter two steps are to be iterated.

Assume a generalized eigenvalue problem

$$\mathbf{H}\left|\psi_i\right\rangle = \varepsilon_i \mathbf{S}\left|\psi_i\right\rangle, \tag{2.73}$$

where $\mathbf{H}$ is the Hamiltonian matrix and $\mathbf{S}$ is the overlap matrix which describes the non-orthogonality of the eigenvectors. Only the lowest N_{band} eigenvalues and the corresponding eigenvectors are sought. The RMM-DIIS starts with a $(N_{\text{band}} \times N_{\text{band}})$ Hamiltonian $\mathbf{H}_0$ which is constructed from $\mathbf{H}$ in some way, e.g., Lowdin's method [54]. Since the eigenvectors of $\mathbf{H}_0$ will be used as the initial trial vectors for finding the corresponding real eigenvectors of $\mathbf{H}$, $\mathbf{H}_0$ should be chosen so that the level structure (the ordering and degeneracy of eigenvalues) of the lowest N_{band} eigenvalues of $\mathbf{H}$ is preserved. Since $N_{\text{band}} \ll N_{\text{pw}}$, the eigenvectors of $\mathbf{H}_0$, $\{\left|a_i\right\rangle, i = 1, \ldots, N_{\text{band}}\}$, can be obtained by direct diagonalization. Then, a set of trial vectors $\{\left|\tilde{\psi}_i^{(0)}\right\rangle, i = 1, \ldots, N_{\text{pw}}\}$ are constructed by:

- $\left|\tilde{\psi}_i^{(0)}\right\rangle = \left|a_i\right\rangle$ (with augmented zeros), for $i = 1, \ldots, N_{\text{band}}$;
- $\left|\tilde{\psi}_i^{(0)}\right\rangle = \left|e_i\right\rangle$, for $i = N_{\text{band}} + 1, \ldots, N_{\text{pw}}$.

$\left|e_i\right\rangle$ is a unit vector with only a one at the i-th position and zeros at all others. This vector set is referred to as a *complete set*. After this initialization step, the trial vectors in the complete set will be refined one by one (band-by-band) to the real eigenvectors. For each trial vector, a vector set called *expansion set*, is constructed, which will be used in the correction step. At first, it has only one vector, $\left|\tilde{\psi}_i^{(0)}\right\rangle$. It evolves as the iteration progresses.

For the i-th trial vector and the m-th iteration, the preconditioning step starts with calculating the Rayleigh quotient

$$\tilde{\varepsilon}_i^{(m)} = \frac{\left\langle \tilde{\psi}_i^{(m)} \right| \mathbf{H} \left| \tilde{\psi}_i^{(m)} \right\rangle}{\left\langle \tilde{\psi}_i^{(m)} \right| \mathbf{S} \left| \tilde{\psi}_i^{(m)} \right\rangle}, \tag{2.74}$$

which is an estimation to the i-th correct eigenvalue ε_i. Then, a quantity of central importance in all iterative methods, the residual vector, is evaluated by

$$|\mathbf{R}\rangle = \frac{\mathbf{H} - \tilde{\varepsilon}_i^{(m)}\mathbf{S}}{\left\langle \tilde{\psi}_i^{(m)} \right| \mathbf{S} \left| \tilde{\psi}_i^{(m)} \right\rangle} \left| \tilde{\psi}_i^{(m)} \right\rangle . \tag{2.75}$$

The norm of residual vector $\mathbb{R}^2 = \langle \mathbf{R}| \, \mathbf{R}\rangle$ (or the residual) is an accepted measure for the error in the current trial vector. Next, a correction vector $\left| \delta\psi_i^{(m)} \right\rangle$ is generated by preconditioning the residual vector with a matrix $\mathbf{K}$

$$\left| \delta\psi_i^{(m)} \right\rangle = \mathbf{K} \, |\mathbf{R}\rangle \, , \tag{2.76}$$

where the preconditioning matrix $\mathbf{K}$ is given by

$$\mathbf{K} = -\sum_{i=1}^{N_{\mathrm{pw}}} \frac{\left| \tilde{\psi}_i^{(m)} \right\rangle \left\langle \tilde{\psi}_i^{(m)} \right|}{\left| \tilde{\psi}_i^{(m)} \right\rangle (\mathbf{H} - \tilde{\varepsilon}_i^{(m)}\mathbf{S}) \left\langle \tilde{\psi}_i^{(m)} \right|}. \tag{2.77}$$

Once generated, the m-th correction vector will be appended to the expansion set. Note that, to this point, the expansion set has evolved to one including $m+1$ vectors, $\{\left| \delta\psi_i^{(0)} \right\rangle, \left| \delta\psi_i^{(1)} \right\rangle, \ldots, \left| \delta\psi_i^{(m)} \right\rangle\}$, where $\left| \delta\psi_i^{(0)} \right\rangle = \left| \tilde{\psi}_i^{(0)} \right\rangle$. The expansion vector set spans the *iterative subspace*.

Now, one enters the correction step. A new trial vector will be constructed by a linear combination of the vectors in the expansion set

$$\left| \tilde{\psi}_i^{(m+1)} \right\rangle = \sum_{j=0}^{m} \alpha_j \left| \delta\psi_i^{(j)} \right\rangle \tag{2.78}$$

with the expansion coefficients $\{\alpha_j\}$ obtained by solving the eigenproblem

$$\mathbf{P} \, |\alpha\rangle = \mathbb{R}^2 \mathbf{Q} \, |\alpha\rangle \tag{2.79}$$

for the eigenvector with the lowest eigenvalue, where the $(m+1)\times(m+1)$ matrices $\mathbf{P}$ and $\mathbf{Q}$ are given by

$$\mathbf{P}_{rs} = \left\langle (\mathbf{H} - \tilde{\varepsilon}_i^{(m)}\mathbf{S})\delta\psi_i^{(r)} | (\mathbf{H} - \tilde{\varepsilon}_i^{(m)}\mathbf{S})\delta\psi_i^{(s)} \right\rangle \tag{2.80}$$

and

$$\mathbf{Q}_{rs} = \left\langle \delta\psi_i^{(r)} \middle| \mathbf{S} \middle| \delta\psi_i^{(s)} \right\rangle, \tag{2.81}$$

respectively. This small eigenproblem can be solved by direct diagonalization. In other words, the choice of the expansion coefficients tries to minimize the residual $\mathbb{R}^2$, hence the name RMM. Also, finding these expansion coefficients involves direct inversion in the iterative subspace, hence the name DIIS.

The preconditioning and correction steps are iterated until the residual $\mathbb{R}^2$ is smaller than a preset tolerance. Different iterative methods and their variances are characterized by the choice on the complete set and the evolution scheme for the expansion set. Also, the preconditioning matrix in Eq. (2.77) and the correction expansion in Eq. (2.78) are not unique.

2.2.9 Density Mixing and Self-consistency Loop

As mentioned in Section 2.2.1, the Kohn-Sham equation has to be solved self-consistently. Starting from random charge density (or the superposition of atomic charge densities), one may directly use the output density from the current iteration as the input of the next iteration. However, an efficient mixing of the output density with some of the previous input densities can improve the stability of iteration and accelerate the convergence to self-consistency.

Various mixing schemes have been developed. The scheme proposed by Pulay and improved by Kresse and Furthmüller using Kerker's preconditioning matrix is demonstrated to be the most efficient [55–57]. Given an initial charge density, this scheme generates a new input charge density after the m-th iteration by

$$\rho_{\text{in}}^{(m+1)} = \rho_{\text{in}}^{\text{opt}} + \mathbf{KR}[\rho_{\text{in}}^{\text{opt}}] \tag{2.82}$$

with

$$\rho_{\rm in}^{\rm opt} = \rho_{\rm in}^{(m)} + \sum_{i=1}^{m-1} \alpha_i \Delta\rho^{(i)}, \tag{2.83}$$

where

$$\mathbf{R}[\rho_{\rm in}] = \rho_{\rm out}[\rho_{\rm in}] - \rho_{\rm in}, \tag{2.84}$$

which is the residual charge density with respect to the input density $\rho_{\rm in}$, and

$$\Delta\rho^{(i)} = \rho_{\rm in}^{(i+1)} - \rho_{\rm in}^{(i)}. \tag{2.85}$$

The preconditioning matrix $\mathbf{K}$ is given by Kerker's scheme,

$$\mathbf{K}(\mathbf{G}) = \frac{A|\mathbf{G}|^2}{|\mathbf{G}|^2 + \lambda^2} \tag{2.86}$$

in which $\mathbf{K}$ is diagonal. A and λ are adjustable parameters. $A = 0.8$ and $\lambda = 1.0$ Å^{-1} are usually suitable for most systems. The coefficient α_i is optimized by

$$\alpha_i = -\sum_{j=1}^{m-1} \frac{\left\langle \Delta\mathbf{R}^{(j)} \middle| \mathbf{R}[\rho_{\rm in}^{(m)}] \right\rangle}{\left\langle \Delta\mathbf{R}^{(i)} \middle| \Delta\mathbf{R}^{(j)} \right\rangle} \tag{2.87}$$

with

$$\Delta\mathbf{R}^{(i)} = \mathbf{R}[\rho_{\rm in}^{(i+1)}] - \mathbf{R}[\rho_{\rm in}^{(i)}]. \tag{2.88}$$

The density mixing scheme described above will be used throughout the thesis.

2.2.10 H-F Forces and Relaxation of Ionic System

The equilibrium configuration of an ionic system is characterized by the minimum total-energy. Since the force on the I-th ion is defined by

$$f_I = -\frac{\partial E}{\partial \mathbf{R}_I}, \tag{2.89}$$

the equilibrium configuration is also a zero force configuration. In most ionic relaxation calculation, moving the ions in a non-equilibrium configuration is directed by the forces calculated on them. However, numerical evaluation of forces by di-

rectly using the definition above involves the calculations of the total-energies of not only the configuration under consideration, but also its neighbors. All these calculations have to be done self-consistently, which is very inefficient from the point of view of computational time. Fortunately, Hellmann and Feynman [58] proved a theorem with which the problem can be greatly simplified.

Formally, the total energy of a system is given by

$$E = \langle\psi|\,\mathbf{H}\,|\psi\rangle\,. \tag{2.90}$$

For the sake of simplicity, the orbital index has been dropped here. Thus, the force can be written as

$$f_I = -\frac{\partial E}{\partial \mathbf{R}_I} = -\langle\frac{\partial\psi}{\partial \mathbf{R}_I}|\mathbf{H}|\psi\rangle - \langle\psi|\,\frac{\partial \mathbf{H}}{\partial \mathbf{R}_I}\,|\psi\rangle - \langle\psi|\mathbf{H}|\frac{\partial\psi}{\partial \mathbf{R}_I}\rangle. \tag{2.91}$$

Hellmann and Feynman proved that the first and third terms in the right-hand side of the equation above cancel each other when ψ is the eigenstate of $\mathbf{H}$. Hence, an ionic relaxation is usually conducted according to the Hellmann-Feynman (H-F) forces, i.e., the second term in Eq. (2.91), after the electronic iteration has converged. The H-F forces can be calculated without consideration of neighboring ionic configurations and the computational time can be greatly saved.

A problem associated with the H-F force is that, if the basis set is not complete, the first and third term in Eq. (2.91) do not cancel each other exactly and an extra term called Pulay force [59] has to be added to the H-F force. Fortunately, it has been shown that the Pulay force vanishes if the derivatives of all basis functions can also be expanded by the basis set [60]. This is true for a plane-wave basis set. However, even though the Pulay forces are zero when using a plane-wave basis set, the Pulay stresses on the unit cell may be nonzero. Therefore, the relaxation of the unit cell parameters has to be done with caution. Fortunately, this is usually *not* necessary in a surface relaxation calculation because the thickness of the vacuum region can be varied to some extent without loss of accuracy.

If the Vanderbilt-type ultrasoft pseudopotentials are employed, the formalism

for calculating the forces will be considerably complicated. Two principal reasons account for this. One is the introduction of the overlap operator $\mathbf{S}$ in Eq. (2.53), which does not appear in the case of norm-conserving pseudopotentials. Another is that the charge density in Vanderbilt's scheme explicitly depends on the ion positions through Q and β as shown in Eq. (2.55). Nevertheless, efficient formalisms for calculating the H-F forces have been developed [48].

Chapter 3

Multilayer Relaxation of Cu(210)

3.1 Introduction

High-index transition metal surfaces are of practical interest in areas such as catalytic chemistry. They have received attention since the early days of surface science [61,62]. However, detailed structure analyses on high-index surfaces started rather late in contrast to those on low-index surfaces. The main reason for this is that the principal technique for surface crystallography, quantitative LEED analysis, encounters methodological difficulty when treating the closely spaced atomic layers in most high-index surfaces.

For a quantitative LEED analysis, the most efficient and extensively used k-space method for calculating the I-V curves is the renormalized forward scattering (RFS) method [63]. However, the RFS method does not converge well for interlayer spacings less than about 1 Å [64]. Currently, the most practical solution for circumventing this difficulty is either to group several atomic layers throughout the surface into medium-sized slabs [65] or to simulate the whole surface region by a thick slab [19]. A common point in both solutions is that l-space methods are involved in the multiple scattering calculations within the slabs. The main difficulty of using l-space methods, e.g., the Beeby-type matrix-inversion method [66] as re-formalized in Section 2.1.7, is the prohibitively long computing time which scales as the cube of the number of layers in the slabs. This scaling property makes l-space methods quite cumbersome for thick slabs. In this sense, another k-space method, the layer-doubling method (cf. Section 2.1.8), may help. The layer-doubling method delays the divergence against the interlayer spacing due to the exact treatment of the multiple scatterings between two layers as opposed to the perturbative treatment in the RFS method. Interest in the layer-doubling method has been recently renewed. The tensor-LEED scheme has been implemented in this method by Materer [34]. However, few high-index surfaces have been successfully studied by the layer-doubling method. In this chapter, the Cu(210) surface is investigated using the layer-doubling method. This surface has an interlayer spacing of 0.808 Å which is the smallest studied by the layer-doubling method.

This chapter also aims to investigate the accuracy of first-principles calcu-

lations on predicting structures of high-index metal surfaces. Clean high-index metal surfaces are suitable benchmarks for checking the current theoretical framework since reliable experimental data on these surfaces are available. The results of multilayer relaxations on several high-index Cu surfaces from both quantitative LEED analysis and first-principles calculations have been reported. They include Cu(311) [67, 68], Cu(331) [69, 70], Cu(211) [70–72], Cu(511) [68, 73] and Cu(711) [19,68] surfaces. In terms of the interlayer spacing, Cu(210) lies between Cu(331) and Cu(211). The first-principles result on this surface, however, is still absent. In this chapter, a pseudopotential DFT study on Cu(210) is conducted to see if consistent results with quantitative LEED analysis can be obtained.

3.2 Cu(210) Surface

The Cu(210) surface is obtained by cutting a copper crystal at 26.6° away from the (100) plane in the [001] azimuth. The top and side views of this surface are shown in Fig. 3.1. From the top view it can be seen that there is only one

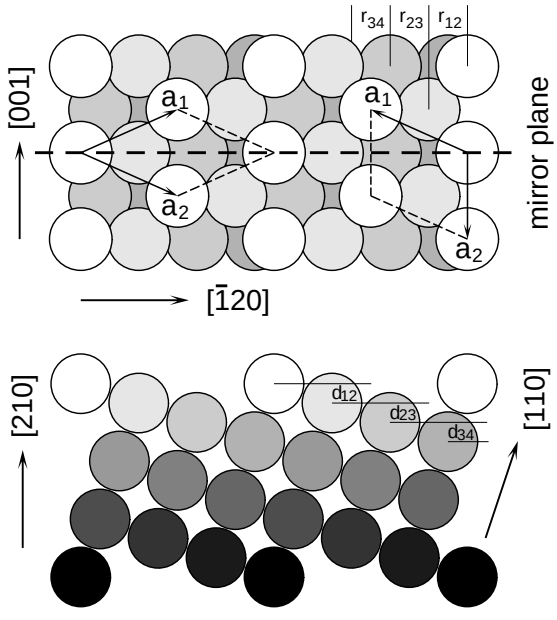

Fig. 3.1: Top view of Cu(210) surface and side view at the mirror plane.

symmetry operation present on this surface, i.e., the mirror plane. Four layers are "visible" from the top view, which demonstrates the openness of this surface. The registry repeats at every eleventh layer as seen from the side view. The interlayer

registries (r_{ij}) and the interlayer spacings (d_{ij}) of the topmost three layers are illustrated in the top and side views, respectively. The interlayer registry and spacing in the bulk-truncated configuration, denoted by r_0 and d_0, are equal to $\frac{1}{\sqrt{5}}a_0$ and $\frac{1}{2\sqrt{5}}a_0$, respectively. Two equivalent surface unit cells are shown in the top view. The left one is used in the slab DFT calculations, the right one in the quantitative LEED analysis.

The coordination number of the atoms in the first layer is only 6. Those in the second and the third layers are 9 and 11 coordinated, respectively. From the fourth layer downwards, the coordination number recovers to the bulk value, i.e., 12. This surface is characterized by steps along the [001] direction and very narrow terraces in-between. The atoms on each step line do not contact each other and are separated by a_0 in terms of the hardball model. The inter-step distance is $\frac{\sqrt{5}}{2}a_0$.

3.3 Layer-doubling LEED Analysis

3.3.1 Experimental I-V Dataset

The multilayer relaxations on Cu(210) have been investigated by two previous quantitative LEED studies [74, 75]. The experimental I-V dataset used in this study is provided by Dr. Ismail [75]. The dataset was collected at 130 K with a normal incidence of the primary electrons. The combined-space method [76] was used in the study by Ismail *et al.* for the multiple scattering calculation. In this study the tensor-LEED approximation was not employed. Therefore, to facilitate the analysis, the previous dataset has been cut into a shorter energy range, i.e., from 60 eV to 350 eV . Finally, nine beams spanning a ΔE=2000 eV energy range were used. Since only six structural parameters were optimized in this work, this dataset is believed to be sufficient. The beam labels are given in Fig. 3.2. They are consistent with the basis vectors (the right unit cell) shown in Fig. 3.1.

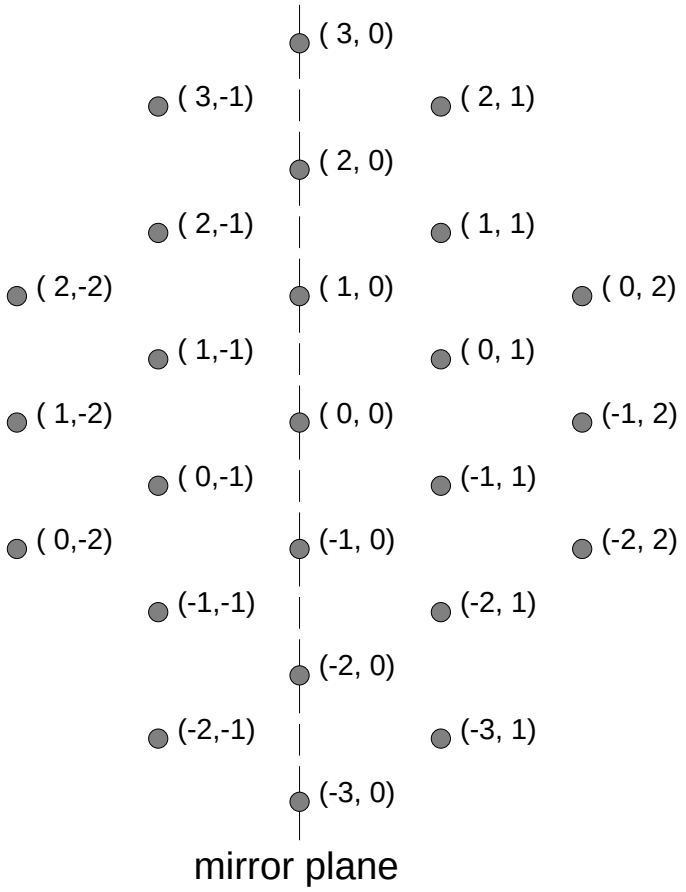

Fig. 3.2: Schematic LEED pattern for Cu(210).

3.3.2 Computer Program

The program used in this thesis for layer-doubling LEED analysis was written in Fortran 90 language adopting the dynamic allocation of memory space, which is important for implementing the energy-dependent features introduced later. This program implements the formalism of the layer-doubling method given in Section 2.1.8 with the scattering matrices of individual layer calculated by the matrix inversion scheme described in Section 2.1.7. In view of the fact that the calculations of phase shifts take negligible computer cycles compared with the full-dynamical LEED intensity calculations, the phase shift generation code is integrated into this program. Thus, no interpolation of the tabulated phase shifts is needed.

The Gaunt coefficients used in Section 2.1.7 are slightly different from those in the existing LEED codes [15, 16]. A subroutine GAUNT is developed to gener-

ate these coefficients. Also, the traditional 1-dimensional storage scheme has been replaced by a new scheme employing a 3-dimensional array with its first index corresponding to the pair $(l''m'')$ in Eq. (2.27) and another two indices corresponding to the pairs (lm) and $(l'm')$, respectively. This scheme makes it easier to do the indexing. In addition, by using the formulas in Eqs. (2.27) and (2.28), GAUNT can work well for $l_{\max} = 13$ even without using double-precision computer arithmetic.

To improve the performance of the program, several schemes have been employed:

- Firstly, the number of propagating beams $N_{\rm b}$ is made energy-dependent. At each energy point, the required $N_{\rm b}$ for representing the wavefield between two layers is estimated by Eq. (2.32). By using the energy-dependent $N_{\rm b}$, the computing time for a full-dynamical calculation can be reduced by a factor of about 2. This scheme also results in a uniform error introduced by the beam cutoff throughout the whole energy range. For implementing this scheme, the beams required at the highest energy are sorted and stored according to their kinetic energies $\frac{1}{2}|\mathbf{k}_{\|} + \mathbf{g}|^2$. At each energy point, only the first $N_{\rm b}$ beams are used.

- Secondly, the basic linear algebra subroutines (BLAS) are called to do the multiplications and inversions of the matrices involved in the layer-doubling formalism. On most modern computer architectures, there are implementations of BLAS, e.g., Intel's Math Kernel Library (MKL), HP's Compaq Extended Math Library (CXML), SGI's Scientific Computing Software Library (SCSL) and IBM's Essential Scientific Software Library (ESSL). Since each implementation of BLAS is specially optimized for a specific architecture (mainly for the cache structure) by the hardware provider, calling BLAS subroutines to execute the same function is much faster than self-developed subroutines, especially for large scale matrices.

- Thirdly, the number of ion-core scattering phase shifts N_l is also made energy-dependent. Two choices are available for determining N_l. One is

to use the classical formula $l_{max} = \kappa R_{\rm mt}$ [15]. Another is to define a small value ϵ and include only the phase shifts with their absolute values larger than ϵ. Numerical results show that [77] the two approaches actually give very similar results for ϵ=0.001.

- Lastly, it is intended to make the number of lattice points involved in the summation of Eq. (2.25) as small as possible. This summation decides the computing time for setting up the l-space propagator. As the property of the spherical Hankel function guarantees the convergence of the summation, only a finite number of lattice points need to be included. The cutoff criterion $r_{\rm max} = 5.0\sqrt{2E}/|V_{0\rm i}|$ introduced in Van Hove/Tong's program [16] was adopted in this program so that all propagations between two atoms with distances larger than $r_{\rm max}$ are neglected.

It should be noted that the major performance gain is due to the first two schemes, while the last two become critical only when thick composite layers are involved, which can be avoided in this thesis.

3.3.3 Details of Analysis

As stated in Section 2.1.4, the inner potential of Cu was taken to be energy-independent. $V_{0\rm i}$ was fixed at -4.5 eV, while $V_{0\rm r}$ was optimized during the course of the best-fit structure search.

The beam cutoff criterion t in Eq. (2.32) was set at 0.002, which corresponds to about 90 propagating beams at the low energy end (60 eV) and about 180 at the high energy end (350 eV).

Only phase shifts with absolute values larger than 0.001 were included. This corresponds to 7 phase shifts at the low energy end and 13 at the high energy end. The muffin-tin potential for Cu tabulated by Morruzi, Janak and Williams [78] was used to generate the phase shifts. The first seven phase shifts calculated from this potential are illustrated in Fig. 3.3.

The temperature effect was taken into account by considering the isotropic thermal vibrations of the ion-cores, which were incorporated in the temperature-

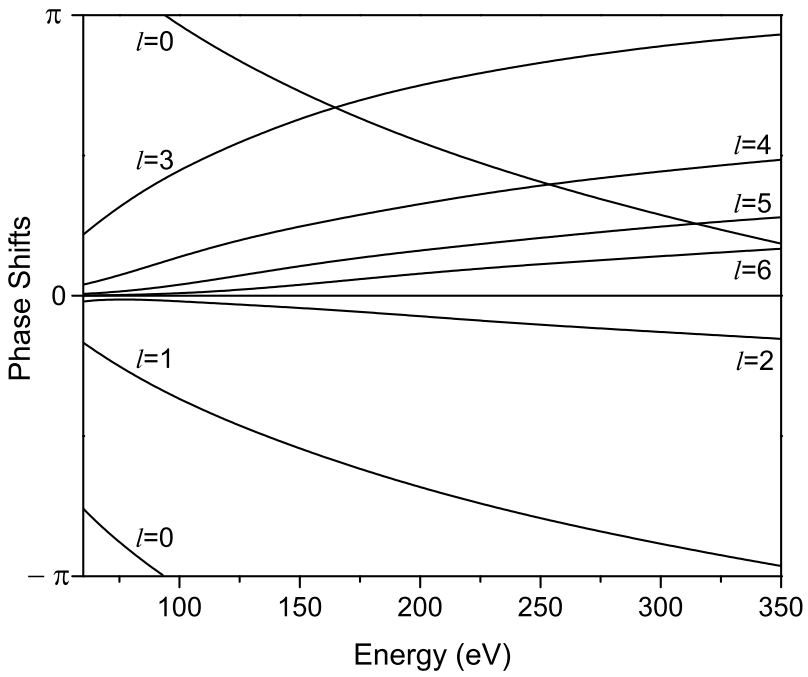

Fig. 3.3: Phase shifts for Cu up to $l_{\max}$=6.

dependent phase shifts. A Debye temperature of 343 K for Cu was used in this study, which corresponds to a vibration amplitude (μ_{bulk}) of 0.086 Å for the bulk atoms at 130 K, the temperature at which the experimental data was collected. The vibration amplitudes of the atoms in the topmost three layers (μ_1, μ_2 and μ_3) were enhanced by factors that were optimized in the best-fit search.

The Pendry R-factor (R_{P}) [27] was adopted in this study to ascertain the agreement between the experimental and the theoretical I-V curves. Both the interlayer spacings (d_{ij}) and the interlayer registries (r_{ij}) of the topmost three layers as shown in Fig. 3.1 were optimized. The minimum R_{P} was located by a conventional grid search with a spacing of 0.01 Å.

3.3.4 Results and Discussion

The parameters which give the best-fit to the experimental I-V curves are listed in Table 3.1. Also listed are the corresponding parameters from Ref. [75]. Δd_{ij} and Δr_{ij} are the relaxations of d_{ij} and r_{ij}, respectively. They are defined as $\Delta d_{ij} = (d_{ij} - d_0)/d_0$ and $\Delta r_{ij} = (r_{ij} - r_0)/r_0$. d_0 and r_0 are the corresponding bulk values of d_{ij} and r_{ij}. It can be seen that the current full-dynamical LEED

Tab. 3.1: Optimized structural and non-structural parameters which give the best-fit to the experimental *I-V* curves.

	This work	Ref. [75]
Δd_{12} (%)	-11.1 ± 1.9	-11.1 ± 2.0
Δd_{23} (%)	-5.0 ± 1.6	-5.7 ± 2.3
Δd_{34} (%)	$+3.7 \pm 1.7$	$+3.8 \pm 2.5$
d_0 (Å)	0.808	0.808
Δr_{12} (%)	-1.9 ± 2.9	-1.8 ± 3.0
Δr_{23} (%)	-1.9 ± 2.5	-2.5 ± 3.2
Δr_{34} (%)	$+0.6 \pm 2.6$	$+1.7 \pm 3.5$
r_0 (Å)	1.616	1.616
μ_1 (Å)	0.138	0.134
μ_2 (Å)	0.112	0.096
μ_3 (Å)	0.103	-
μ_{bulk} (Å)	0.086	0.086
$V_{0\mathrm{r}}$ (eV)	-6.0	-5.99
$V_{0\mathrm{i}}$ (eV)	-4.5	-4.0
R_{P}	0.12	0.15
var(R_{P})	0.016	0.017

analysis using the layer-doubling method and the previous tensor-LEED analysis using the combined-space method give basically identical results.

The best-fit calculated *I-V* curves are compared with the experimental ones in Fig. 3.4. The beam-averaged R_{P} between the two sets of curves is 0.12 and the variance of R_{P}, var(R_{P}), is 0.016 as evaluated by Pendry's formula, Equation (2.36). This result is comparable to the best achieved on high-index surfaces, i.e., on the Cu(711) surface where $R_{\mathrm{P}} = 0.12$ and var(R_{P}) = 0.013 were reported [19].

The error bars for the structural parameters in Table 3.1 are also evaluated by Pendry's approach [27]. A plot of R_{P} versus the deviations of the six structural parameters from their best-fit values is given in Fig. 3.5. The dashed line indicates the level of min(R_{P})+var(R_{P}). The two intersections of a parabola with the dashed line are the upper and lower limits of the corresponding structural parameter. From this figure, it can be seen that quantitative LEED analysis is more sensitive to the change in vertical relaxations (Δd's) than lateral relaxations (Δr's). The

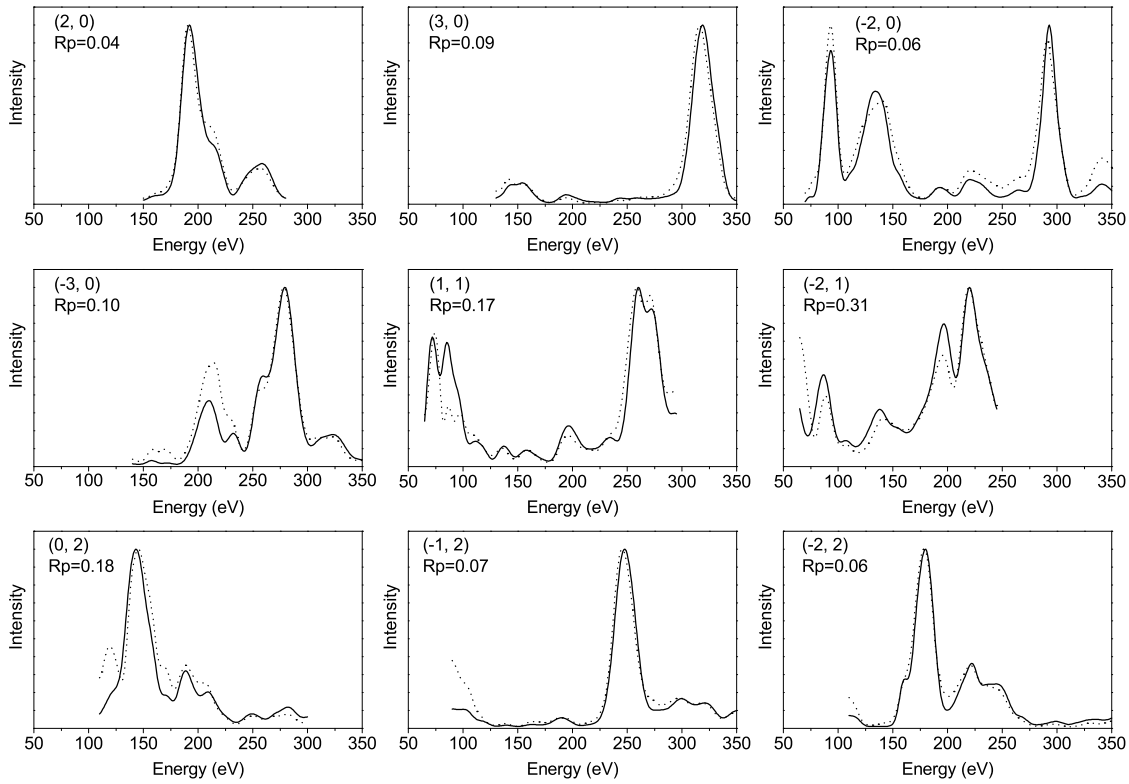

Fig. 3.4: Comparison of experimental (solid line) and best-fit theoretical (dashed line) I-V curves for Cu(210) surface. The experimental curves were measured at 130 K.

error bars for Δd's are all within 0.01 – 0.02 Å, while larger than 0.04 Å for all Δr's. This is mainly due to the fact that most quantitative LEED studies adopt the normal incidence geometry.

A direct inspection of Fig. 3.4 also confirms the excellent agreement between the two sets of I-V curves. All detailed features exhibited in the experimental curves have been reproduced by the calculations except for several regions where a small peak becomes a shoulder or vice versa. This agreement was not achieved in the previous studies [74, 75].

Dynamical (multiple scattering) features, such as weak peaks and shoulders, in I-V curves are crucial for quantitative LEED analysis. In the current study the accurate reproduction of both the kinematic (single scattering) and the dynamical features in the experimental I-V curves implies that the layer-doubling method works well for high-index metal surfaces with the interlayer spacings down to at least 0.8 Å, in particular, for materials in which the multiple scattering is not very

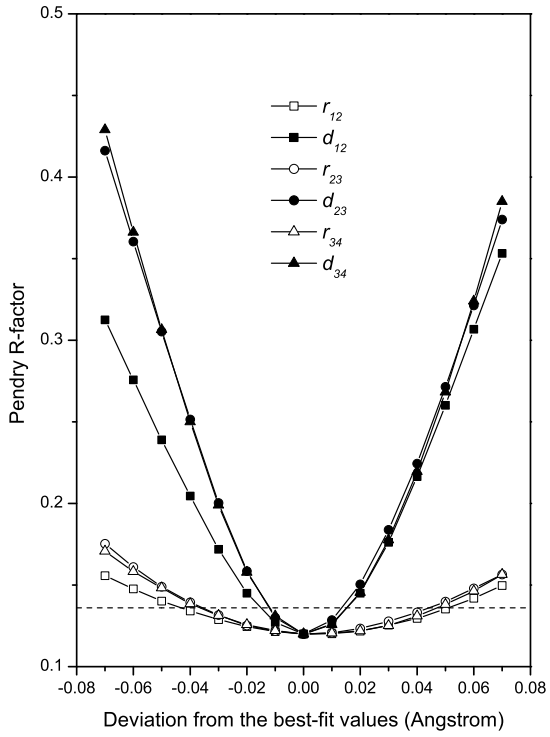

Fig. 3.5: Plot of R_{P} versus the deviations of the structural parameters from their best-fit values.

strong.

When conducting structural studies on chemisorption systems, sufficient models have to be considered. Quantitative LEED analysis on these systems using the l-space methods is usually tedious even with the tensor-LEED scheme [79]. This work should pave the way for future studies on various chemisorption systems on Cu(210) surface and other similar surfaces, such as Ni(210).

3.4 First-principles Calculations

3.4.1 Computer Program

Self-consistent periodic slab calculations within the framework of DFT were conducted by the Vienna *ab initio* simulation package (VASP) [56, 80, 81] to find the equilibrium ionic configuration of the Cu(210) surface. VASP is one of the most popular DFT packages employing the pseudopotential plane-wave method. Many research groups over the world are using this package to perform first-principles studies of many kinds of materials properties. The reliability of the

results produced by this package has been confirmed by numerous publications in the literature.

For carrying out a surface relaxation study, VASP iteratively solves the Kohn-Sham equation for the electronic ground state of an initial ionic configuration setup by the user. After this calculation the ions are moved according to Hellmann-Feynman forces to predict a new trial ionic configuration. This process is repeated until the forces become less than a prescribed criterion. In VASP, the interactions between the ion-cores and valence electrons can be described by either the Vanderbilt-type ultrasoft pseudopotential (USPP) or the projector augmented wave (PAW) method [82]. A variety of approximations to the xc functional are available in this package.

3.4.2 Details of Calculations

The USPP's provided in the VASP package [83] were used in this study. The generalized gradient approximation (GGA) of Perdew-Wang [38] was used for the exchange-correlation (xc) functional. To investigate the effects of different ion-core representations and different xc approximations on the prediction of multilayer relaxations by first-principles calculations, the PAW method was compared with the USPP and the local density approximation (LDA) of Perdew-Zunger [84] was compared with the GGA.

The lattice constant (a_0) of fcc Cu was firstly obtained by performing bulk calculations. Three combinations of the pseudopotentials and the xc functionals, namely USPP-GGA, PAW-GGA and USPP-LDA, were used. The obtained a_0 is 3.64 Å for USPP-GGA, 3.64 Å for PAW-GGA and 3.53 Å for USPP-LDA. (Experimental a_0 = 3.61 Å.) These values were used in the following slab calculations accordingly. A plot of total energy versus lattice constant (the case of USPP-GGA) is given in Fig. 3.6.

In the bulk calculations, a grid of $(8\times8\times8)$ **k**-points used for the Brillouin zone integration was generated according to the scheme of Monkhorst and Pack [50]. This grid corresponds to 60 irreducible **k**-points in the reduced BZ. Only the plane-

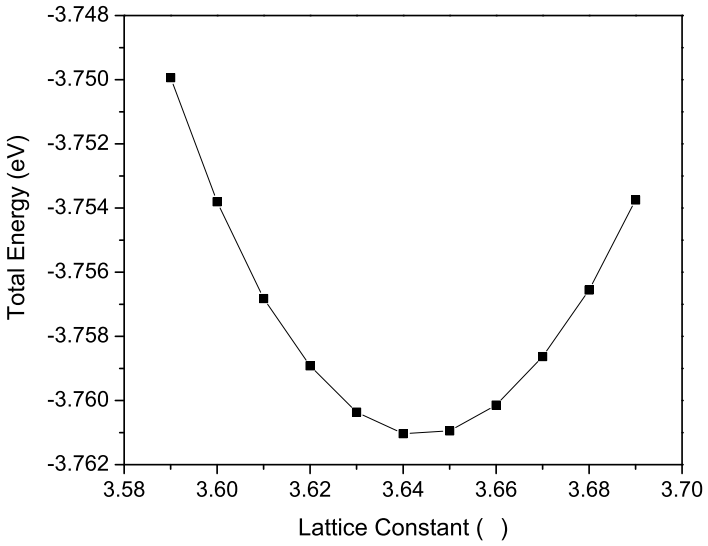

Fig. 3.6: Plot of total energy versus lattice constant for fcc Cu.

waves with kinetic energies below 340 eV were included in the basis set. From

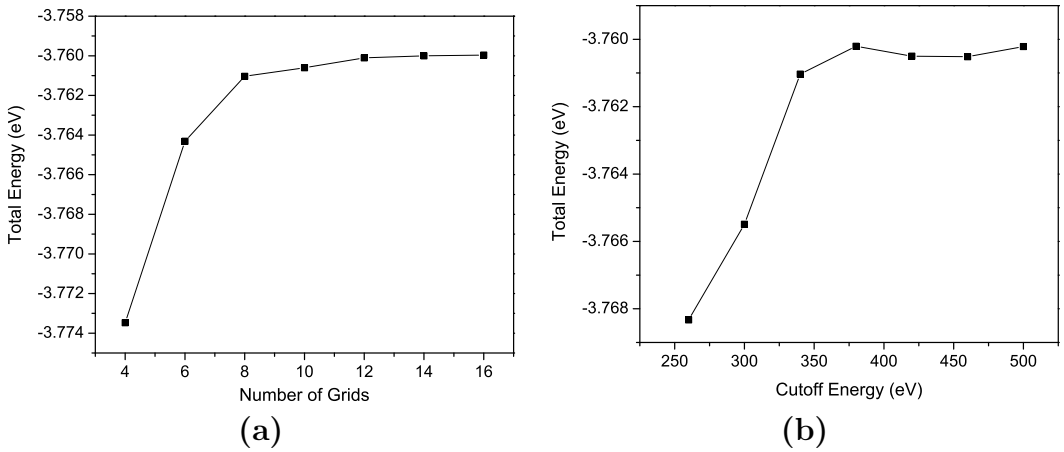

Fig. 3.7: Convergence testing for the number of **k**-points and the cutoff energy for Cu.

Fig. 3.7, it can be seen that both the number of grids and the cutoff energy could converge the total energy per bulk Cu atom to about 1 meV, which is sufficiently accurate for almost all kinds of first-principles calculations.

The supercell (slab) approximation was employed in this study to model the Cu(210) surface, where each slab consists of 21 atomic layers and a 10 Å thick vacuum layer was used to separate adjacent slabs. For testing purposes, 19-layer slabs were also used.

For the slab calculations, a $(8 \times 8 \times 1)$ grid, which corresponds to 20 irreducible **k**-points, was used. The surface unit cell used in the slab calculations is rhombic

as illustrated in Fig. 3.1 (the left one). The cutoff energy is the same as in the bulk calculations. The relaxations were stopped when the forces became less than 10 meV/Å.

The smearing method of Methfessel and Paxton [51] was used in this study to reduce the number of **k**-points for total energy convergence. A smearing width (σ) of 0.5 eV was used for Cu. As obtained from the calculation on the relaxed structure, the entropy term per Cu atom is less than 1 meV by using this σ. The zero temperature total energies were obtained by extrapolating to $\sigma = 0$ eV.

3.4.3 Results and Discussion

Tab. 3.2: Multilayer relaxations of Cu(210) surface from pseudopotential DFT calculations using different setups.

	USPP GGA 21-layer	USPP GGA 19-layer	PAW GGA 21-layer	USPP LDA 21-layer
a_0 (Å)	3.64	3.64	3.64	3.53
Δd_{12} (%)	−16.4	−16.5	−17.1	−17.0
Δd_{23} (%)	−4.5	−6.2	−4.8	−4.2
Δd_{34} (%)	+7.2	+7.4	+7.0	+6.6
Δd_{45} (%)	−0.6	−0.5	−1.2	−1.3
Δd_{56} (%)	−0.9	−1.3	−0.9	−0.8
Δd_{67} (%)	+1.4	+0.7	+0.8	+0.9
Δr_{12} (%)	−1.1	−1.2	−1.0	−0.9
Δr_{23} (%)	−1.0	−1.2	−0.8	−1.0
Δr_{34} (%)	+2.0	+2.4	+2.4	+2.0
Δr_{45} (%)	−1.0	−0.5	−0.8	−0.9
Δr_{56} (%)	−1.2	−1.0	−1.2	−1.3
Δr_{67} (%)	−0.3	−0.1	−0.4	−0.4

The multilayer relaxations of the Cu(210) surface by pseudopotential DFT calculations using four different setups are listed in Table 3.2. For the USPP-GGA calculation with a 21-layer slab, it can be seen that only the topmost three layers relax significantly and the relaxation sequence is consistent with the LEED analyses, i.e., $- - + \cdots$, where "−" denotes a contraction, "+" an expansion and "$\cdots$" means that the sequence followed is not definite due to the small relaxations.

However, quantitative differences from the relaxations in Table 3.1 are observed.

Comparing the second and third columns in Table 3.2, it can be seen that the largest difference between the results calculated from a 19-layer slab and a 21-layer slab is 1.7% for Δd's and 0.5% for Δr's. This implies that the error introduced by a finite thickness slab is about 0.015 Å. In view of other approximations employed in the calculations, such as the non-zero residual forces, the **k**-point sampling and the plane-wave cutoff, it is estimated that the total errors in the final ionic positions are about 0.02 Å.

As can be seen from Table 3.1, LEED is less sensitive to Δr as compared to Δd. The error bars for the Δr's are always larger than 0.04 Å. In view of this, the discrepancies in Δr's are acceptable, while only discrepancies in Δd smaller than 0.04 Å are acceptable excluding the temperature effect discussed later. Judged by this criterion, only the discrepancy in Δd_{12} (about 0.043 Å) is slightly large.

The result using the PAW method is listed in the fourth column of Table 3.2. It can be seen that the PAW does not improve the discrepancy. Table 3.2 also shows that the LDA gives similar relative results to the GGA even though the difference between the bulk lattice constants is larger than 0.1 Å.

Another possible reason that may account for the discrepancies is the temperature-dependency of relaxations, which is recently attracting more attention. Both thermal expansion and contraction of relaxations have been observed on open metal surfaces [85–87]. However, due to the limited number of temperature-dependent studies on multilayer relaxations of high-index surfaces, the picture of the dependency is not clear yet. Nevertheless, due to the low temperature (130 K) at which the LEED dataset for Cu(210) is collected, the temperature effect should not be very significant.

3.5 Conclusion

The multilayer relaxation of the Cu(210) surface has been studied by layer-doubling LEED analysis and pseudopotential DFT calculations. The best-fit structure obtained from the current layer-doubling LEED analysis is identical

to that obtained from a previous study using combined space method. The calculated I-V curves from the best-fit structure show excellent agreement with the experimental ones as judged by both visual inspection and a small R_{P} (0.12). These results imply that the layer-doubling method is a suitable choice for quantitative LEED analyses on high-index metal surfaces with interlayer spacings down to 0.8 Å. Based on this reliable LEED result, the accuracy of the DFT calculations on prediction of the structure of Cu(210) is investigated. The correct relaxation sequence of this surface, i.e., $- - + \cdots$, has been obtained by the pseudopotential DFT calculations. The largest quantitative discrepancy in the structural parameters is about 0.04 Å.

Chapter 4

Multilayer Relaxation of Fe(310)

4.1 Introduction

Determination of surface crystallographic structures is a fundamental topic in surface science. Without the structural information, studies on electronic, energetic, magnetic and vibrational properties of surfaces, such as density of states, work function, spin magnetic moment, and surface phonons, can only be qualitative. Quantitative LEED analysis is the principal experimental technique for surface crystallography, while parameter-free first-principles calculations based on DFT are the most definitive theoretical method for predicting surface structures. Obtaining mutually consistent results has become a common goal for researchers working in both LEED and DFT. This consistency has been achieved on many clean metal surfaces, including low-index and high-index surfaces. However, inconsistencies still exist, an example being the Fe(310) surface.

In one of the pioneering studies on detailed structure determination of high-index metal surfaces, Sokolov, Jona and Marcus (SJM) studied the Fe(310) surface by quantitative LEED analysis [88]. They obtained the structure of Fe(310) as: the relaxation of the first interlayer spacing (Δd_{12}) is $-16.1\pm3.3\%$, the second (Δd_{23}) $+12.6\pm3.3\%$ and the third (Δd_{34}) $-4.0\pm4.4\%$; the relaxation of the first interlayer registry (Δr_{12}) is $+7.2\pm2.8\%$ and the second (Δr_{23}) $+1.6\pm2.8\%$, where the $-$ sign denotes a contraction and $+$ an expansion. The interlayer spacing (d) and the interlayer registry (r) of Fe(310) are illustrated in Fig. 4.1. In a recent article, Geng, Kim and Freeman (GKF) studied the structure and magnetism of Fe(310) by full-potential linearized augmented plane-wave (FLAPW) method [89]. In this study, the authors obtained a Δd_{12} of about -14.4%, while all other structural parameters (d_{23}, d_{34}, r_{12} and r_{23}) have very small relaxations (less than 2%). It can be seen that significant discrepancies, beyond the accuracy of both LEED analysis and DFT calculations, exist for Δr_{12} and Δd_{23}.

The cause of the discrepancy may be two-fold. With regard to the LEED analysis, GKF postulated three possible reasons [89]. The first is the limited size of the I-V dataset. The second is the insufficient number of structural parameters that were allowed to relax. The third is the non-consideration of the temperature-

dependent surface vibrational effect. As for the FLAPW study, the results are also unexpected. GKF deduced significant relaxation only for the first interlayer spacing, which is unusual for such an open surface as Fe(310) (see Fig. 4.1) since multilayer relaxation on high-index surfaces is usually more significant than on low-index surfaces.

In this chapter, a refined quantitative LEED analysis and a pseudopotential DFT study are conducted on Fe(310). The aim of this study is to investigate if the pseudopotential plane-wave method can produce consistent results with LEED analysis since this has been achieved on other high-index metal surfaces [71, 72, 90–93].

4.2 Fe(310) Surface

The Fe(310) surface is obtained by cutting the crystal at 18.4° away from the (100) plane in the [001] azimuth. The top and side views of this surface are shown in Fig. 4.1. The depth of layers from the surface are indicated by the gray scale.

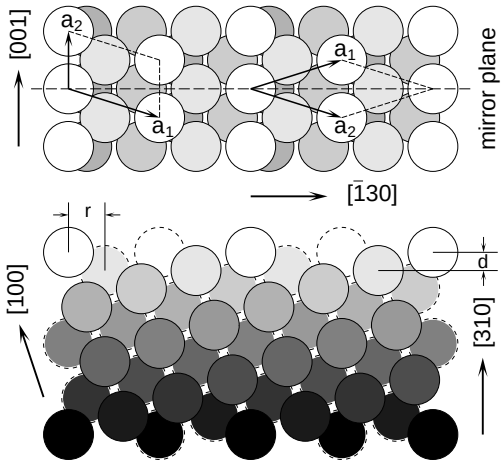

Fig. 4.1: Top view of Fe(310) surface and side view at the mirror plane.

Four layers are shown in the top view. The gaps between the "atoms" (circles) reflect the openness of this surface, and deeper layers are "visible" through these gaps from the top view. The registry repeats at every 11th layer as seen from the side view. The dashed circles represent another layer of atoms that can be seen from the side view.

The interlayer registry (r) and the interlayer spacing (d) are illustrated in the side view. r_0 and d_0 equal to $\frac{2}{\sqrt{10}}a_0$ and $\frac{1}{\sqrt{10}}a_0$, respectively. The (310) surface is the fourth closest-packed surface of bcc structure and has a d_0 smaller than (110), (100) and (211) surfaces. The coordination number of the atoms in the first layer is only 4. Those in the second layer are 6-fold coordinated. From the third layer downwards, the coordination number recovers to the bulk value, i.e., 8. Like Cu(210) surface, Fe(310) is also characterized by steps along [001] direction and atomic terraces in-between. These steps are more widely separated compared with Cu(210). The inter-step distance is $\frac{\sqrt{10}}{2}a_0$.

4.3 Quantitative LEED Analysis

4.3.1 Details of Analysis

The experimental I-V dataset used in this study is from the previous LEED study by SJM [88]. 9 beams from the normal incidence case, which span a $\Delta E =$ 1200 eV, were used. In Fig. 4.2, a schematic LEED pattern from Fe(310) is illustrated.

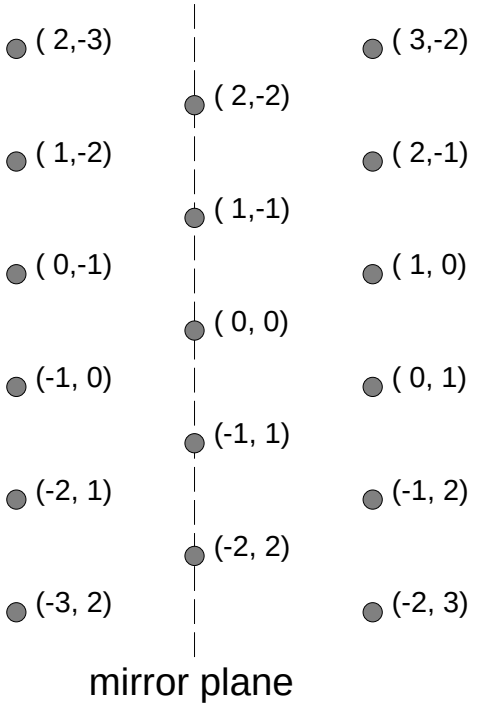

Fig. 4.2: Schematic LEED pattern for Fe(310).

The layer-doubling method was adopted to carry out the multiple scattering analysis. This method has demonstrated convergence on Fe(111) which has a smaller interlayer spacing [34]. The number of propagating beams ($N_{\rm b}$) and the number of ion-core scattering phase shifts (N_l) were made energy-dependent in this analysis. At the low energy end (20 eV), $N_{\rm b}$ is about 55 and N_l is 5; at the high energy end (200 eV), $N_{\rm b}$ is about 105 and N_l is 11. The muffin-tin potential for Fe used to generate the phase shifts was also from Morruzi, Janak and Williams [78]. In Fig. 4.3 the first seven phase shifts calculated from this potential are shown. The inner potential was taken to be energy-independent. The imaginary part (V_{0i})

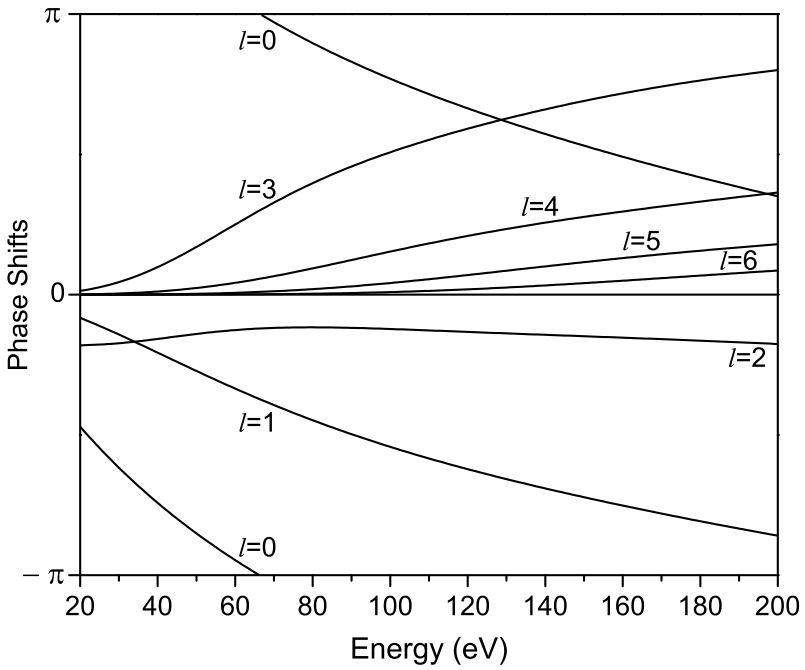

Fig. 4.3: Phase shifts for Fe up to $l_{\rm max}$=6.

was fixed at −4.0 eV, while the real part (V_{0r}) was optimized during the course of the best-fit structure search.

The temperature effect was taken into account by considering the isotropic thermal vibrations of the ion-cores, which were incorporated in the temperature-dependent phase shifts. A Debye temperature of 467 K for Fe was used in this study, which corresponds to a vibration amplitude of 0.102 Å for the bulk atoms at room temperature (the temperature at which the I-V data was collected). The positions and vibration amplitudes of the ion-cores down to the fourth layer were

optimized in this analysis. Three more structural parameters (i.e., r_{34}, r_{45} and d_{45}) and four more non-structural parameters (i.e., the vibration enhancement factors for the topmost four layers) than the previous LEED analysis [88] were allowed to relax.

Another important factor that may affect the best-fit structure is the R-factor used to ascertain the agreement between the measured and calculated I-V curves. The inconsistency between the results obtained from using different R-factors may indicate a far deviation from the global minimum in the parameter space. In this study, the Pendry R-factor (R_{P}) [27] was adopted to see if consistent results can be achieved by using a different R-factor. R_{P} is different from the Zanazzi-Jona R-factor, which was used by SJM [88], in the sense that the former is more sensitive to the weak peaks. The best-fit structure is found by a conventional grid search with a spacing of 0.01 Å.

4.3.2 Results and Discussion

The multilayer relaxation results of Fe(310) obtained from the new LEED analysis are given in Table 4.1. Also listed are the corresponding results from SJM. It can be seen that the current LEED results are essentially the same as those of SJM. The largest difference in Δd's is 1.6%. The large relaxation of r_{12} as obtained by SJM was also confirmed by the new LEED analysis. Allowing three more structural parameters to relax has only a marginal effect on the best-fit structure except for Δr_{23} where a small expansion from SJM's analysis has been changed to a small contraction. The V_{0r} for iron as optimized from the current analysis is -10.1 eV. This value is identical to that obtained by SJM.

The I-V curves calculated from the best-fit structure are compared with the experimental ones in Fig. 4.4. The beam notation used in Fig. 4.4 is that by SJM as illustrated in Fig. 4.2. It should be noted that these labels are not consistent with the unit cell shown in Fig. 4.1 (the left one) which is actually used in the current LEED analysis.

The beam-averaged R_{P} between the two sets of curves in Fig. 4.4 is 0.14 and

Tab. 4.1: Multilayer relaxation of Fe(310) determined by LEED analyses.

	This work	SJM
Δd_{12} (%)	-17.7 ± 3.1	-16.1 ± 3.3
Δd_{23} (%)	$+12.1 \pm 1.8$	$+12.6 \pm 3.3$
Δd_{34} (%)	-5.5 ± 2.0	-4.0 ± 4.4
Δd_{45} (%)	$+1.1 \pm 2.2$	-
d_0 (Å)	0.906	0.906
Δr_{12} (%)	$+6.6 \pm 3.4$	$+7.2 \pm 2.8$
Δr_{23} (%)	-1.1 ± 3.1	$+1.6 \pm 2.8$
Δr_{34} (%)	$+2.8 \pm 3.1$	-
Δr_{45} (%)	-1.1 ± 3.0	-
r_0 (Å)	1.813	1.813
$V_{0\mathrm{r}}$ (eV)	-10.1	-10.1
$V_{0\mathrm{i}}$ (eV)	-4.0	-4.0
R-factor	R_{P}=0.14	R_{ZJ}=0.116

var(R_{P}) is 0.02. A plot of R_{P} versus the deviations of the structural parameters from their best-fit values is given in Fig. 4.5, from which the error bars of the structural parameters, as given in Table 4.1, are estimated.

The relatively narrow energy range of the dataset used in this study is compensated by the numerous I-V curve features considered. The number of peaks and shoulders included in this dataset is comparable to those from other high-index metal surfaces with wider energy range [19, 75]. The features of I-V curves, especially the dynamical (multiple scattering) features, are often more important than the spanned energy range for an accurate LEED analysis. Direct inspection of Fig. 4.4 shows that almost all features in the experimental I-V curves have been reproduced by the calculations. The uncertainty in the structural parameters due to a finite size of dataset has been considered in the error bars.

The optimized vibration amplitudes are 0.194 Å for the first layer, 0.163 Å the second, 0.184 Å the third and 0.143 Å the fourth. The vibration enhancement is more significant compared with that on Cu(117) [19] and Cu(210) [35, 75] since the I-V data of Fe(310) was collected at a higher temperature. However, it is found that the enhanced vibrations have little impact on the best-fit structural

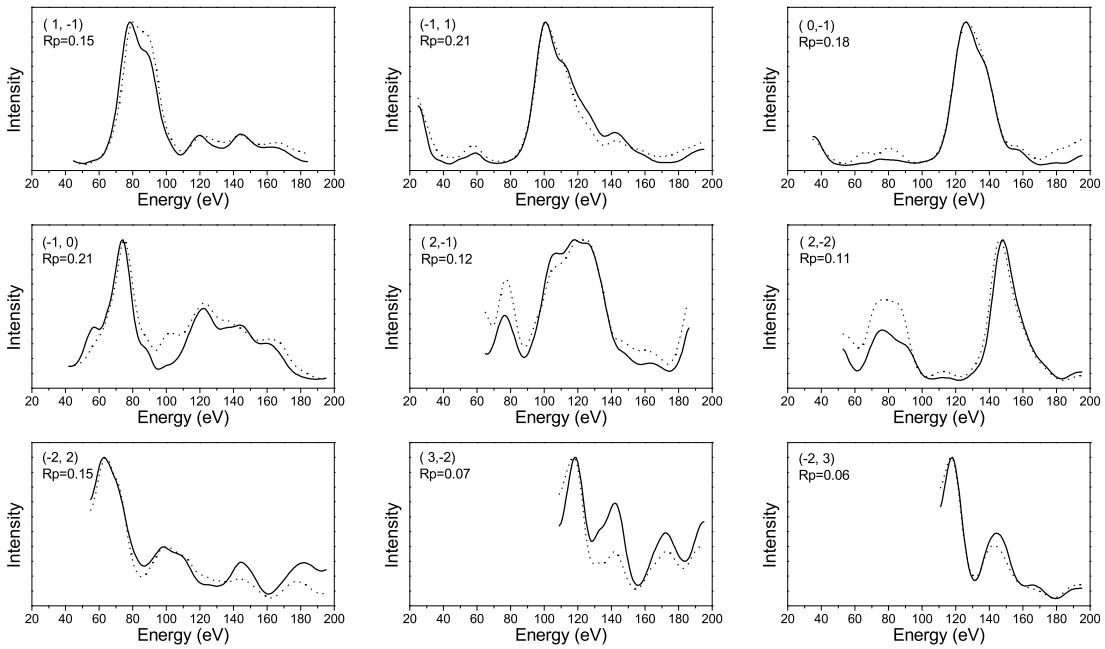

Fig. 4.4: Comparison of experimental (solid line) and best-fit theoretical (dotted line) I-V curves for Fe(310) surface. The experimental curves were measured at room temperature.

parameters (about 1%), but only improve the beam-averaged R_{P} from 0.20 to 0.14.

The consistency between the present and SJM's LEED results implies that the global minimum in the parameter space has been reached in both analyses. In this case, choosing different R-factors has only little effect on the best-fit structure.

4.4 Pseudopotential DFT Calculations

4.4.1 Details of Calculations

The VASP code was used in this study to carry out the periodic slab calculations using the pseudopotential plane-wave method. The USPP for Fe is provided in the VASP package. The generalized gradient approximation of Perdew-Wang [38] was taken for the exchange-correlation functional. A cutoff energy of 340 eV was used in all calculations. The positions of the ion-cores are relaxed according to the Hellmann-Feynman forces. The relaxation is terminated when the forces on all ion-cores become less than 10 meV/Å. The smearing method of Methfessel and Paxton [51] was used in this study to handle the abrupt jump of

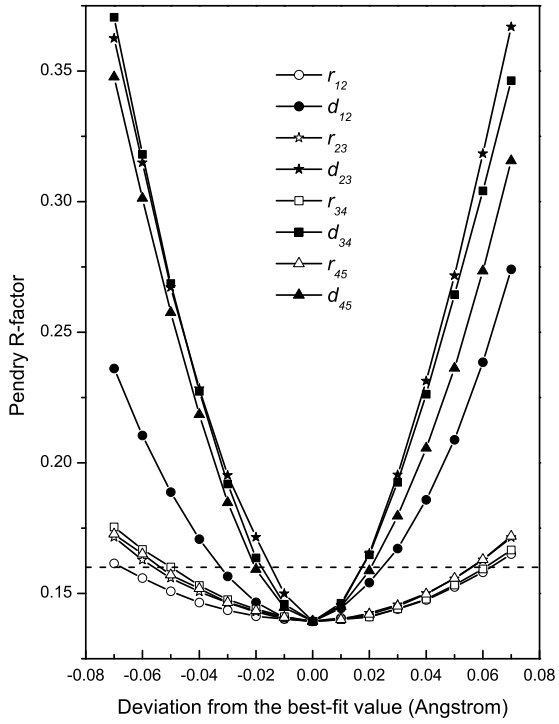

Fig. 4.5: Plot of R_{P} versus the deviations of the structural parameters from their best-fit values.

occupancies from 1 to 0 at the Fermi level. A smearing width of 0.2 eV was used for iron.

The bulk calculations on bcc Fe give a lattice constant of 2.86 Å. This value is slightly smaller than the experimental value of 2.87 Å and was used in the following slab calculations. The plot of total energy versus lattice constant for bcc Fe is given in Fig. 4.6. In the bulk calculations, a grid of $(12 \times 12 \times 12)$ **k**-points used for the Brillouin zone integration was generated according to the scheme of Monkhorst and Pack [50]. This grid corresponds to 68 irreducible **k**-points in the reduced BZ. Only the plane-waves with kinetic energies below 340 eV were included in the basis set. From Fig. 4.7, it can be seen that both the number of grids and the cutoff energy could converge the total energy per bulk Fe atom to about 1 meV.

The Fe(310) surface was represented by a slab consisting of 21 atomic layers. Adjacent slabs were separated by a vacuum layer of about 10 Å thick. A $(8\times8\times1)$ Monkhorst-Pack grid [50], which corresponds to 20 irreducible **k**-points, was used for the Brillouin zone integration. The surface unit cell used in the slab calculations

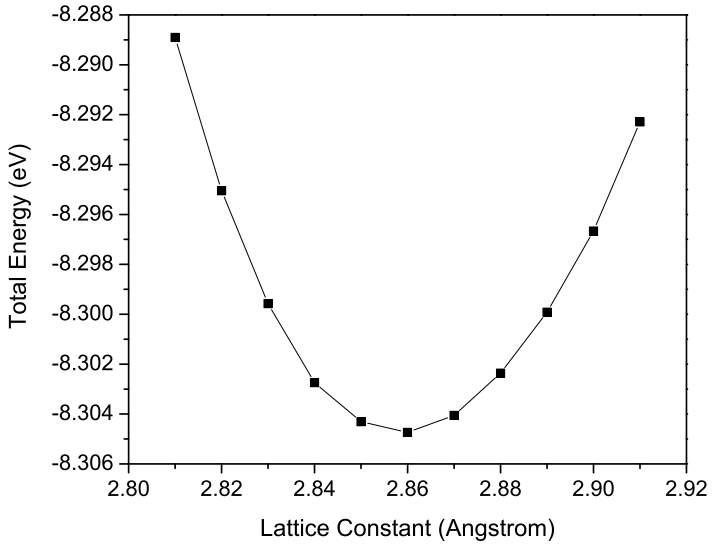

Fig. 4.6: Plot of total energy versus lattice constant for bcc Fe.

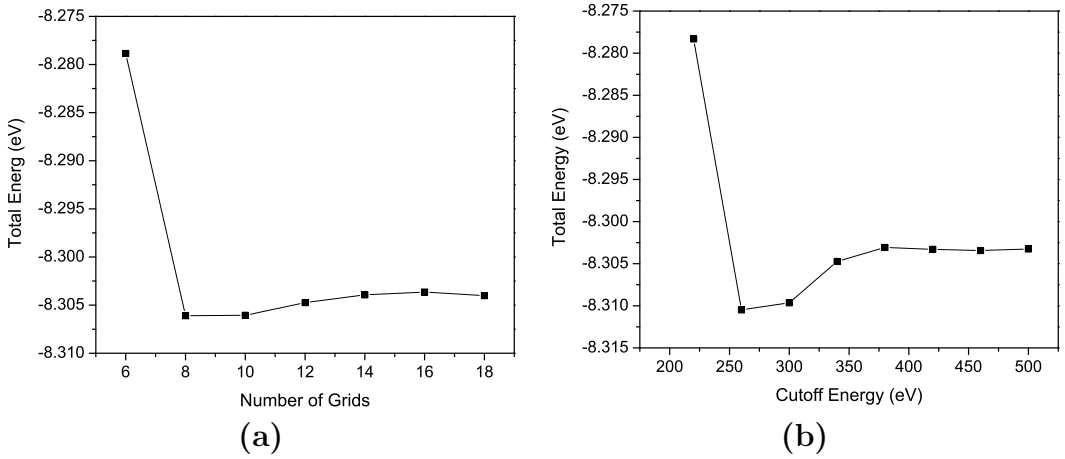

Fig. 4.7: Convergence testing for the number of **k**-points and the cutoff energy for Fe.

is shown in Fig. 4.1 (the right one). All layers except for the center one in the 21-layer slab were allowed to move in the relaxation calculations. Spin-polarization effect was taken into account in both the bulk and slab calculations due to the strong ferromagnetism of iron.

To confirm the reliability of the current pseudopotential DFT results, another pseudopotential plane-wave package, CASTEP, was also used to study the structure of Fe(310). All setups in the CASTEP calculations are the same as described above except that CASTEP uses the Gaussian smearing method rather than the method of Methfessel and Paxton. A smearing width of 0.1 eV was used in the CASTEP calculations. In addition, the bulk calculations using CASTEP give a

Tab. 4.2: Multilayer relaxation of Fe(310) obtained from DFT calculations.

	This work (VASP)	This work (CASTEP)	GKF (FLAPW)
Δd_{12} (%)	−14.9	−14.2	−14.4
Δd_{23} (%)	+8.0	+7.8	+1.1
Δd_{34} (%)	−1.4	−2.8	0.0
Δd_{45} (%)	+4.1	+2.8	0.0
d_0 (Å)	0.904	0.895	0.900
Δr_{12} (%)	+4.9	+4.6	+1.7
Δr_{23} (%)	+0.4	+0.1	−0.6
Δr_{34} (%)	+1.4	+1.3	-
Δr_{45} (%)	−0.4	−0.4	-
r_0 (Å)	1.808	1.790	1.800

lattice constant of 2.83 Å for bcc Fe.

4.4.2 Results and Discussion

In Table 4.2 multilayer relaxations of Fe(310) obtained from various first-principles calculations are shown. It can be firstly seen that the pseudopotential calculations by VASP and CASTEP give very close results. Both of them reproduce the relaxation sequence of the interlayer spacings obtained by the LEED analyses, i.e., $- + - +$. The largest discrepancy in the structural parameters obtained from the current LEED analysis and pseudopotential calculations is less than 0.04 Å. This quantitative agreement is acceptable if considering the error bars in the LEED analysis as listed in Table 4.1 and the approximations employed in the pseudopotential calculations, such as the finite slab thickness and the non-zero residual forces on the ion-cores, which result in errors of about 0.01–0.02 Å. From Table 4.2 it can also be seen that the large relaxation of r_{12} as obtained by both the previous and current LEED analyses was also confirmed by our pseudopotential calculations.

In pseudopotential calculations, the total energy of a valence electron system is typically three orders of magnitude smaller than that in full-potential all-electron calculations. Therefore, in the pseudopotential method, the accuracy required on calculating the energy differences between ionic configurations is much less strict than that in full-potential methods. This feature may reduce the technical errors in

the relaxation calculations, which are based on the total energy or force (derivative of total energy) minimizations. On the aspect of the basis set, the plane-waves are decided only by the shape and size of the supercell (atomic slab plus vacuum layer) and independent of the positions of the ion-cores. Hence, the plane-wave basis set can be kept fixed throughout the relaxation process. This feature is unique to the plane-wave method and also helpful for accurately calculating the energy differences between ionic configurations. The advantages discussed above make the pseudopotential plane-wave method a competitive tool for relaxation studies on surfaces. This has been demonstrated on open metal surfaces by the consistency between LEED analysis and pseudopotential calculations achieved on Fe(310) in this study as well as on other open metal surfaces, such as Cu(211) [71, 72], Mo(211) [90, 91] and Al(331) [92, 93].

4.5 Conclusion

In summary, the structure of the Fe(310) surface has been studied by a refined quantitative LEED analysis and pseudopotential DFT calculations. Similar results to the previous LEED study by SJM have been obtained by our new LEED analysis. It is found that allowing more structural parameters to relax has only a marginal effect on the best-fit structure. Considering the enhanced vibrations of surface atoms and using a different R-factor do not significantly affect the LEED analysis. The pseudopotential DFT calculations reproduce the relaxation sequence of the interlayer spacings determined by the LEED analysis, i.e., $- + - +$ with the largest discrepancy in the structural parameters less than 0.04 Å. A large lateral relaxation of the first interlayer registry has been confirmed by both the LEED analysis and pseudopotential calculations.

Chapter 5

Rule of Multilayer Relaxations on Open Metal Surfaces

5.1 Introduction

Many attempts to understand the mechanism of ionic relaxations on single crystal metal surfaces have been made in the past three decades. Based on experimental results, the topmost atomic layer on low-index metal surfaces can relax both inwards and outwards. Extensive theoretical studies have concentrated on drawing a general rule on top layer relaxations observed experimentally [94]. As made clear by Feibelman [95], a physical picture and a chemical picture exist to describe the top layer relaxations. The former originated from the theory of Finnis and Heine [96] using the concept of charge smoothing by Smoluchowski [97]. The latter was put forward by Feibelman [95] and is based on the bond-order–bond-length relation [98]. Recently, high-index metal surfaces have received much attention due to their importance in areas such as catalytic chemistry. In contrast to low-index surfaces, all high-index metal surfaces experimentally studied exhibit, without exception, a contraction on the first interlayer spacing. Another feature of high-index metal surfaces is that *multilayer* relaxations on them are usually more significant. Predicting *a priori* the relaxation sequence on a high-index metal surface has become a new focus of the theoretical studies. Both the physical and chemical pictures have been adopted to explain the multilayer relaxations on high-index metal surfaces [70, 93]. A general rule, which relates the relaxation sequence to the number of atomic steps on the terrace, has also been proposed [69]. However, as will be shown, this rule is not consistent with first-principles results on some surfaces, e.g., Cu(320) and Cu(410).

In this chapter, an empirical rule of multilayer relaxations on open metal surfaces is postulated based on experimental results on high-index Cu surfaces. A systematic evaluation on this rule is then conducted on a series of vicinal Cu surfaces. Finally, a physical explanation in the light of Smoluchowski's charge smoothing picture is given.

5.2 The Rule Proposed

The single crystal surfaces of copper are the most extensively studied by both quantitative LEED analysis and first-principles calculations. Hence, it will be meaning to review these surfaces. In Table 5.1 the multilayer relaxations of high-index Cu surfaces obtained by quantitative LEED analysis and slab DFT calculations are shown. Although the extent of quantitative agreement between LEED and DFT results differs from one study to another, the relaxation sequence obtained by both techniques are consistent on all these surfaces.

Tab. 5.1: Comparison of multilayer relaxations of high-index Cu surfaces from quantitative LEED analysis and slab DFT calculations.

	Cu(311)		Cu(331)	
	LEED Ref. [67]	USPP Ref. [68]	LEED Ref. [69]	FLAPW Ref. [70]
Δd_{12} (%)	−11.9	−15.0	−13.8	−22.0
Δd_{23} (%)	+1.8	+4.0	+0.4	+1.6
Δd_{34} (%)			+4.0	+6.9
Δd_{45} (%)			−4.0	−2.4
	Cu(210)		Cu(211)	
	LEED This work	USPP This work	LEED Ref. [71]	PP Ref. [72]
Δd_{12} (%)	−11.1	−16.4	−14.9	−14.4
Δd_{23} (%)	−5.0	−4.5	−10.8	−10.7
Δd_{34} (%)	+3.7	+7.2	+8.1	+10.9
	Cu(511)		Cu(711)	
	LEED Ref. [73]	USPP Ref. [68]	LEED Ref. [19]	USPP Ref. [68]
Δd_{12} (%)	−14.2	−11.1	−13.0	−9.3
Δd_{23} (%)	−5.2	−16.4	−2.0	−7.7
Δd_{34} (%)	+5.2	+8.4	−10.0	−21.8
Δd_{45} (%)	−1.2	−4.6	+7.0	+14.3
Δd_{56} (%)	+3.2	+2.3	−1.0	−3.0
Δd_{67} (%)	−3.1	−1.5	−4.0	−9.1
Δd_{78} (%)	−3.3	+0.2	+7.0	+5.6

In Table 5.1 it can be noticed that (210), (211) and (511) have the same relaxation sequence for the first three interlayer spacings. Inspired by this hint, a general rule of the multilayer relaxations on open metal surfaces can be postulated, which states:

> At bulk-truncated configuration, define a *surface slab* in which the nearest neighbors (nn's) of all atoms are fewer than those in the bulk. In the process of relaxation, the interlayer spacing between each pair of layers within this slab contracts, while the spacing between this slab and the substrate expands.

In this rule, the relaxation sequence of a surface is related to the change in the number of nn's. The nn sequences for the six fcc surfaces in Table 5.1 are given in Table 5.2. Taking (210) as an example, the nn sequence (6,9,11,12 $\cdots$) means

Tab. 5.2: Relation between nn sequence and postulated relaxation sequence of high-index surfaces of fcc structure. N is the number of layers in the *surface slab* (see text).

Orientation	nn sequence	N	Relaxation sequence
(311)	(7,10,12 $\cdots$)	2	$- + \cdots$
(331)	(7, 9,11,12 $\cdots$)	3	$- - + \cdots$
(210)	(6, 9,11,12 $\cdots$)	3	$- - + \cdots$
(211)	(7, 9,10,12 $\cdots$)	3	$- - + \cdots$
(511)	(7, 8,10,12 $\cdots$)	3	$- - + \cdots$
(711)	(7, 8, 8,10,12 $\cdots$)	4	$- - - + \cdots$

that, at bulk-truncated configuration, the atoms in the first layer have 6 nn's, the second layer 9 and the third 11. From the fourth layer downwards, the number recovers to 12, the value in the bulk. Thus, according to the proposed rule, the *surface slab* of fcc (210) consists of three layers and the interlayer spacings within this slab (i.e., d_{12} and d_{23}) contract, while the spacing between this slab and the substrate (i.e., d_{34}) expands. Hence, the relaxation sequence is $- - + \cdots$. The rest of Table 5.2 can be deduced by analogy.

A violation to this rule in Table 5.1 is Cu(331), where a relaxation sequence of $- + + \cdots$ was deduced from a LEED study [69] and was reproduced by a FLAPW study [70]. Discussion on this will be given later in the next chapter.

5.3 The Rule Evaluated

Systematic evaluation of the rule postulated in the last section by experiments such as LEED is costly. Fortunately, from Chapters 3 and 4, it has been shown

that the pseudopotential DFT calculations are reliable in studying the multilayer relaxations quantitatively. In this section, this technique will be solely employed to evaluate this rule on a series of vicinal Cu surfaces.

A pseudopotential DFT study on eight vicinal Cu surfaces has been conducted in a recent paper [68], while a more systematic study will be conducted in this chapter. Since, in the postulated rule, the multilayer relaxations are related to the reduction in the number of nn's, it is more suitable to perform the evaluation on the surfaces ranked by their openness, or in other words, the interlayer spacing.

In Table 5.3, the open Cu surfaces with their interlayer spacings down to about 0.5 Å are given. The interlayer spacings can be evaluated by

$$d_{\text{bulk}} = \frac{a_0}{\delta\sqrt{h^2+k^2+l^2}}, \tag{5.1}$$

where (hkl) are the Miller indices of the surface and δ equals to two if there is at least an even number in the indices and one otherwise. The postulated relaxation sequences for these surfaces are also given in Table 5.3.

Tab. 5.3: Open Cu surfaces ranked by their interlayer spacings.

Orientation	d_{bulk}	nn sequence	N	Relaxation sequence
(110)	$a_0/2\sqrt{2}$	(7, 11, 12 $\cdots$)	2	$-+\cdots$
(311)	$a_0/\sqrt{11}$	(7, 10, 12 $\cdots$)	2	$-+\cdots$
(331)	$a_0/\sqrt{19}$	(7, 9, 11, 12 $\cdots$)	3	$--+\cdots$
(210)	$a_0/2\sqrt{5}$	(6, 9, 11, 12 $\cdots$)	3	$--+\cdots$
(211)	$a_0/2\sqrt{6}$	(7, 9, 10, 12 $\cdots$)	3	$--+\cdots$
(511)	$a_0/\sqrt{27}$	(7, 8, 10, 12 $\cdots$)	3	$--+\cdots$
(531)	$a_0/\sqrt{35}$	(6, 8, 10, 11, 12 $\cdots$)	4	$---+\cdots$
(221)	$a_0/2\sqrt{9}$	(7, 9, 9, 11, 12 $\cdots$)	4	$---+\cdots$
(310)	$a_0/2\sqrt{10}$	(6, 8, 9, 11, 12 $\cdots$)	4	$---+\cdots$
(533)	$a_0/\sqrt{43}$	(7, 9, 9, 10, 12 $\cdots$)	4	$---+\cdots$
(711)	$a_0/\sqrt{51}$	(7, 8, 8, 10, 12 $\cdots$)	4	$---+\cdots$
(551)	$a_0/\sqrt{51}$	(7, 7, 9, 11, 11, 12 $\cdots$)	5	$----+\cdots$
(320)	$a_0/2\sqrt{13}$	(6, 7, 9, 11, 11, 12 $\cdots$)	5	$----+\cdots$

It is worth noting that Cu(711) and Cu(551) have the same interlayer spacing and the same shape of surface unit cell, but different stacking, i.e., different interlayer vector. The different stacking results in a different nn sequence, i.e., (7,

8, 8,10,12 $\cdots$) for (711) and (7, 7, 9,11,11,12 $\cdots$) for (551). This means that the surface slab of Cu(711) consists of four atomic layers, while Cu(551) five. Hence, different relaxation sequences are expected on the two surfaces.

In order to evaluate the postulated rule, pseudopotential DFT calculations were employed here. VASP is used to carry out the calculations. The setup of the calculations has been described in the previous two chapters. In brief, the USPP was used for Cu and the GGA for xc functional. The cutoff energy for the plane-waves was set to 340 eV and the termination criterion for the ionic relaxations was 10 meV/Å. The slab thickness, the **k**-points setup and the surface unit cells used are given in Table 5.4.

Tab. 5.4: The slab thickness (N_t, i.e., the number of atomic layers in the slab) and the number of irreducible **k** points (N_k) used in the calculations. The surface unit cells are defined by vectors $\mathbf{a}_1$ and $\mathbf{a}_2$, which are given by $\mathbf{a}_1 = a_0(a_{11}\hat{\mathbf{x}}+a_{12}\hat{\mathbf{y}})$ and $\mathbf{a}_2 = a_0(a_{21}\hat{\mathbf{x}} + a_{22}\hat{\mathbf{y}})$, respectively.

Surface	N_t	**k**-points (N_k)	a_{11}	a_{12}	a_{21}	a_{22}
Cu(110)	15	(16×12×1) - 48	$\frac{\sqrt{2}}{2}$	0	0	1
Cu(311)	17	(10×10×1) - 30	$\frac{\sqrt{2}}{4}$	$\frac{\sqrt{22}}{4}$	$-\frac{\sqrt{2}}{4}$	$\frac{\sqrt{22}}{4}$
Cu(331)	21	(10×10×1) - 30	$\frac{\sqrt{2}}{4}$	$\frac{\sqrt{38}}{4}$	$-\frac{\sqrt{2}}{4}$	$\frac{\sqrt{38}}{4}$
Cu(210)	21	(10×10×1) - 30	$\frac{1}{2}$	$\frac{\sqrt{5}}{2}$	$-\frac{1}{2}$	$\frac{\sqrt{5}}{2}$
Cu(211)	23	(16× 8×1) - 32	$\frac{\sqrt{2}}{2}$	0	0	$\sqrt{3}$
Cu(511)	25	(10×10×1) - 30	$\frac{\sqrt{2}}{4}$	$\frac{\sqrt{54}}{4}$	$-\frac{\sqrt{2}}{4}$	$\frac{\sqrt{54}}{4}$
Cu(531)	27	(8× 8×1) - 32	$\frac{\sqrt{6}}{2}$	0	$-\frac{\sqrt{6}}{12}$	$\frac{\sqrt{210}}{12}$
Cu(221)	29	(16× 6×1) - 24	$\frac{\sqrt{2}}{2}$	0	0	$\frac{3\sqrt{2}}{2}$
Cu(310)	29	(12× 8×1) - 24	1	0	0	$\frac{\sqrt{10}}{2}$
Cu(533)	31	(6× 6×1) - 12	$\frac{\sqrt{2}}{4}$	$\frac{\sqrt{86}}{4}$	$-\frac{\sqrt{2}}{4}$	$\frac{\sqrt{86}}{4}$
Cu(711)	33	(6× 6×1) - 12	$\frac{\sqrt{2}}{4}$	$\frac{\sqrt{102}}{4}$	$-\frac{\sqrt{2}}{4}$	$\frac{\sqrt{102}}{4}$
Cu(551)	33	(6× 6×1) - 12	$\frac{\sqrt{2}}{4}$	$\frac{\sqrt{102}}{4}$	$-\frac{\sqrt{2}}{4}$	$\frac{\sqrt{102}}{4}$
Cu(320)	33	(6× 6×1) - 12	$\frac{1}{2}$	$\frac{\sqrt{13}}{2}$	$-\frac{1}{2}$	$\frac{\sqrt{13}}{2}$

The calculated multilayer relaxations of open Cu surfaces are listed in Table 5.5. Since the lateral relaxations of all these surfaces are relatively small (about 2% or less),[1] only the relaxations of the interlayer spacings are given. Comparing the two tables and the last column of Table 5.3, it can be seen that

[1] The Cu(310) has a somewhat larger lateral relaxation on Δd_{45}. It is about 3.5%. The Cu(531) is a surface having no mirror plane. The lateral relaxations were not evaluated.

the relaxation sequences on all the 13 surfaces comply with the proposed rule, i.e., $N_s - 1$ contractions followed by an expansion. Note that, as expected, Cu(711) and Cu(551) exhibit different relaxation sequences although they have the same interlayer spacing and surface unit cell.

Tab. 5.5: Multilayer relaxations of vicinal Cu surfaces.

		(110)	(311)	(331)	(210)	(211)	(511)
Δd_{12} (%)		−9.9	−13.7	−13.6	−16.2	−13.1	−10.4
Δd_{23} (%)		**+4.4**	**+4.5**	−5.1	−5.6	−9.9	−13.6
Δd_{34} (%)		−1.0	−0.4	**+8.0**	**+6.9**	**+9.5**	**+9.4**
Δd_{45} (%)		+0.7	−0.2	−2.5	−0.5	−1.6	−3.8
Δd_{56} (%)		+0.1	+0.9	−0.2	−0.6	−1.0	+2.0
Δd_{67} (%)		+0.2	−0.5	+0.2	+0.3	+0.8	−0.3
	(531)	(221)	(310)	(533)	(711)	(551)	(320)
Δd_{12} (%)	−16.7	−14.3	−11.8	−15.9	−12.3	−7.5	−11.5
Δd_{23} (%)	−12.3	−6.8	−15.4	−2.2	−4.1	−18.0	−16.5
Δd_{34} (%)	−1.3	−5.9	−4.1	−13.0	−18.0	−5.5	−6.3
Δd_{45} (%)	**+8.6**	**+12.7**	**+10.2**	**+14.6**	**+15.7**	−1.3	−3.9
Δd_{56} (%)	−0.3	−4.6	−2.0	−0.4	−3.1	**+13.9**	**+13.7**
Δd_{67} (%)	−1.0	−1.4	−0.8	−4.4	−4.6	−1.8	−1.4
Δd_{78} (%)	−1.0	+1.8	+0.2	−0.4	+3.4	−3.3	−1.4
Δd_{89} (%)	+0.8	−0.5	+0.8	+1.7	+2.5	−1.9	−0.5
Δd_{90} (%)	+0.9	+0.0	+0.4	+0.2	−1.2	+1.6	−1.2

However, some of the relaxations in Table 5.5, such as Δd_{34} on Cu(531), Δd_{23} on Cu(533) and Δd_{45} on Cu(551), are too small to be said unambiguously as having a contraction. Nevertheless, it can be noticed the relaxation sequences are actually characterized by the positions where the expansions take place. From this point of view, there is no ambiguity since the expansions on all the 13 surfaces are significant.

5.4 The Rule Explained

According to the physical picture of surface relaxations, the ionic relaxations are induced by the charge redistribution near the surface region. Hence, the relaxation rule proposed can be understood from the charge redistribution on these surfaces. For this purpose, we calculated the electric charge within a sphere centered at the nuclei of all atoms in the simulating slabs. The sphere radius

is chosen to be the Wigner-Seitz radius, i.e., the radius that makes the volume of the sphere equal to that of the Wigner-Seitz unit cell. This is in the spirit of the atomic sphere approximation in the linear muffin-tin orbital method [99]. For Cu, this radius is 1.42 Å. All calculations were done on slabs at *bulk-truncated* configurations. This choice is also made for studying the forces applied on the ion-cores due to the charge redistribution since these forces drive the ionic relaxations. The plots of the number of charges within a sphere against the layer depth are given in Fig. 5.1.

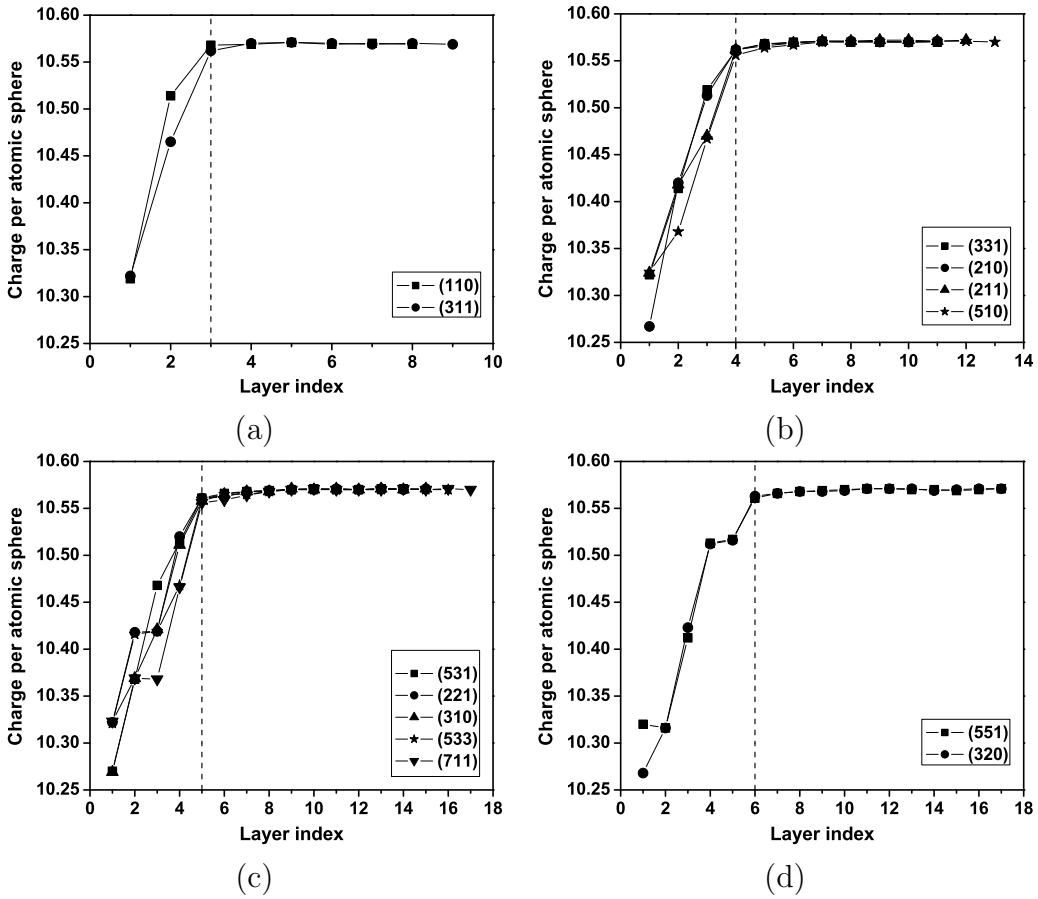

Fig. 5.1: Charge smoothing on vicinal Cu surfaces at bulk-truncated configurations. (a)-(d) are the surfaces with surface slab thickness 2, 3, 4 and 5, respectively.

In Fig. 5.1, the 13 surfaces are divided into four groups according to their relaxation sequences (or number of atomic layers in their surface slabs). It can be seen that the number of layers in which the charge per atomic sphere considerably decreases, coincide with the number of layers in the surface slab defined in the last section. This indicates a direct relation of the relaxation sequence to the charge

redistribution on these surfaces. By performing site-projected calculations, it was found that about 90 % charge loss in the surface slab is due to the $4p$ electrons that are promoted from $4s$ orbitals and are located in the outermost shell.

This charge redistribution can be understood in the light of Smoluchowski's concept of charge smoothing. According to this concept, at metal surfaces, the nearly-free electrons tend to spread towards regions of low charge density and smooth the corrugation formed by the ion-cores in order to reduce the kinetic energy. With the picture of charge smoothing in mind, the relaxation sequence can be understood as follows. In the process of charge smoothing, the ion-cores in deeper layers shift towards the surface, induced by the movement of the electrons, and result in contraction of the interlayer spacings near the surface. For more open surfaces, electrons from the deeper layers contribute to the smoothing, hence more spacings contract. The number of contractions in the relaxation sequence depends on the number of layers in the surface slab (i.e., N in Table 5.3).

Tab. 5.6: Initial forces (component perpendicular to the surface) on the ion-cores calculated at the bulk-truncated configurations. f_n denotes the forces on the atoms in the n-th layer. The unit used is eV/Å.

Surface	f_1	f_2	f_3	f_4	f_5	f_6
Cu(110)	**+0.41**	**−0.38**	−0.04			
Cu(311)	**+0.46**	**−0.27**	−0.23			
Cu(331)	**+0.45**	−0.06	**−0.32**	−0.06		
Cu(210)	**+0.60**	−0.08	**−0.41**	−0.19		
Cu(211)	**+0.45**	+0.01	**−0.23**	−0.22		
Cu(511)	**+0.45**	+0.16	**−0.26**	−0.28		
Cu(531)	**+0.64**	+0.14	−0.27	**−0.34**	−0.23	
Cu(221)	**+0.44**	+0.02	−0.01	**−0.31**	−0.07	
Cu(310)	**+0.58**	+0.19	−0.07	**−0.41**	−0.27	
Cu(533)	**+0.40**	−0.01	+0.04	**−0.21**	−0.15	
Cu(711)	**+0.41**	+0.15	+0.15	**−0.25**	−0.25	
Cu(551)	**+0.42**	+0.38	−0.07	−0.35	**−0.31**	−0.00
Cu(320)	**+0.60**	+0.38	−0.07	−0.43	**−0.34**	−0.17

The effect of the charge redistribution can be seen from the calculated initial forces on the ion-cores at bulk-truncated configurations as listed in Table 5.6, where a + sign denotes a force pointing into the surface and − out of the surface. From this table, it can be seen that, for all the surfaces, the topmost layer feels

an inward force and the N-th layer feels an outward force, while the forces on the layers in between are not definite. This means that the two sides of the surface slab feel compression forces, which lead to contractions within the surface slab. If the magnitude of f_{N+1} is always smaller than f_N, the expansion of the spacing between the surface slab and the substrate can also be explained readily. However, we found $|f_4| > |f_3|$ on Cu(511) and $|f_5| \approx |f_4|$ on Cu(711). This implies that dynamically monitoring the forces in the process of the simulated relaxation, instead of solely studying the initial forces, is necessary in order to explain the expansion. Fig. 5.2 illustrates the force changes in simulated relaxations on Cu(511) and Cu(711). It can be seen that all forces vanish in a monotonic way except for f_{N+1}, which changes from negative to positive after two relaxation steps. This illustration using Cu(511) and Cu(711) is representative of all other surfaces studied and independent of the algorithm (conjugate gradient and variable metric methods are tested) used in the relaxation. It is the opposite sign of f_N and f_{N+1} that is responsible for the expansion.

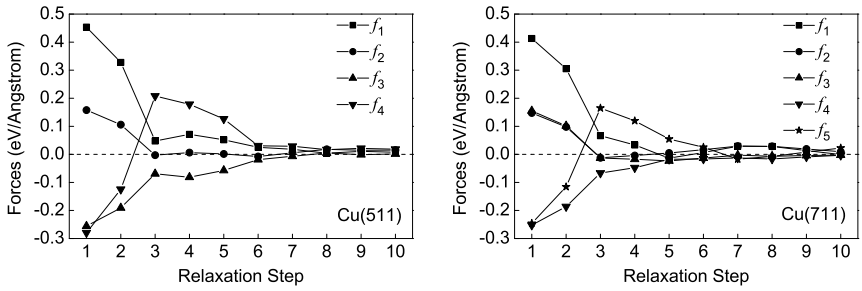

Fig. 5.2: Force changes in simulated relaxations on Cu(511) and Cu(711).

As mentioned in the introduction, another rule [69], which relates the relaxation sequence to the number of atomic steps on the terrace, is also proposed. According to this rule, if there are N atomic steps on a terrace, the relaxation sequence will be $N-1$ contractions followed by an expansion. However, the number of atomic rows on a terrace can not be decided unambiguously. Moreover, this rule predicts a relaxation sequence of $--+\cdots$ for fcc(320) and $---+\cdots$ for fcc(410). Yet, according to Table 5.5, Cu(320) has a relaxation sequence of $----+\cdots$. And fcc(410) has an nn sequence of (6, 8, 8, 9, 11, 12 $\cdots$), hence a relaxation sequence of $----+\cdots$ according to the newly proposed rule.

This is also confirmed by pseudopotential DFT calculations on Cu(410), where the relaxations of the first five interlayer spacings are -14.4%, -6.1%, -16.8%, -3.5% and $+13.9\%$.

Finally, it is noted that the proposed rule is also consistent with the bond-order–bond-length relation, i.e., the chemical picture [95]. Based on this relation, when the number of neighbors of an atom is reduced, the bonds become stronger, hence the bond-length is shortened. In the surface slab, all atoms have less nearest neighbors than those in the bulk. Hence, the interlayer spacings (the bond-length) within it become shorter. If considering the surface slab as a whole with respect to the substrate, the top layers of the substrate actually see more neighbors due to the contractions in the surface slab. This results in a weakened bonding between the surface slab and the substrate and may explain the expansion between them.

5.5 Conclusion

An empirical rule of the multilayer relaxations on open metal surfaces is proposed. Pseudopotential DFT calculations are employed to evaluate this rule systematically on a series of vicinal Cu surfaces with interlayer spacings down to about 0.5 Å. The relaxation sequences obtained on all the surfaces conform to the postulated rule. It has been illustrated that the Smoluchowski's charge smoothing effect in the bulk-truncated surface accounts for the first $N-1$ contractions and the following expansion. This rule can be understood using both physical and chemical arguments, which warrants an extension of this rule in the understanding of all open metal surfaces.

Chapter 6

Further Evaluation of the Proposed Rule

6.1 Introduction

An empirical rule of multilayer relaxations on open metal surfaces has been proposed and evaluated on a series of vicinal Cu surfaces in the last chapter. To be a universal rule, it should be further checked whether the surfaces of different metals with the same orientation follow the same relaxation sequence and whether the open surfaces of other structures (such as bcc, hcp and even reconstructed) obey this rule. There have been about 20 high-index metal surfaces elucidated by experimental techniques [14]. Unfortunately, these results are not sufficient to establish a general rule of multilayer relaxations. For example, the relaxation sequence of Cu(331) has been determined by quantitative LEED analysis to be $-++$ [69], which is different from $--+$ on Al(331) [92, 93] although they have the same orientation. Since Al is a simple metal and Cu a transition metal (TM), a logical question is whether other fcc (331) TM surfaces follow the same sequence as Cu(331). Yet, performing a detailed structure determination by LEED is not an easy task, especially on stepped surfaces as has been stated in Chapter 3. Fortunately, pseudopotential DFT calculations have proven to be a powerful tool in determining the structures of stepped metal surfaces not only qualitatively but quantitatively (see Chapters 3–4) and can be employed to systematically study the relaxation trends of a series of stepped TM surfaces.

In this Chapter, the multilayer relaxations of (311), (331) and (210) surfaces of seven TM's of fcc structure, namely Ni, Cu, Rh, Pd, Ag, Ir and Pt are studied by pseudopotential DFT calculations. (311), (331) and (210) are the fourth, fifth and sixth most close-packed surfaces of the fcc structure, respectively. Most previous LEED studies focused on these three orientations. All the seven TM's have important catalytic applications in chemical engineering, environment control or scientific research. Among these surfaces, some have been studied by other DFT calculations, such as Ni(210) [100], Cu(311) [68], Cu(331) [70], Pd(210) [101] and Pt(311) [102]. For consistency, these surfaces are reinvestigated in this chapter. Also, it will be shown that this rule is consistent with the existing results on the open surfaces of bcc and hcp metals and even reconstructed surfaces.

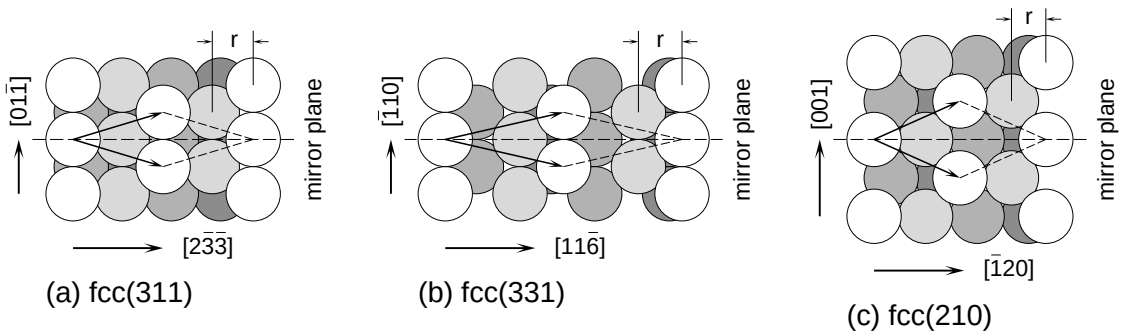

Fig. 6.1: Top views of fcc (311), (331) and (210) surfaces at bulk-truncated configurations. The depth of layers from the surface are indicated by the gray scale. The interlayer spacing (d) is $\frac{a_0}{\sqrt{11}}$ for (311), $\frac{a_0}{\sqrt{19}}$ for (331) and $\frac{a_0}{2\sqrt{5}}$ for (210). The interlayer registries (r's) as illustrated are $\frac{5a_0}{2\sqrt{22}}$, $\frac{7a_0}{2\sqrt{38}}$ and $\frac{a_0}{\sqrt{5}}$ for (311), (331) and (210), respectively.

6.2 (311), (331) and (210) Surfaces of fcc Transition Metals

6.2.1 Calculations

The supercell approximation was used to model the surface. The fcc (311), (331) and (210) surfaces were represented by 16, 20 and 21 atomic layers, respectively. The thickness of the vacuum region was always larger than 10 Å. Pseudopotential DFT calculations were carried out using VASP. A plane wave cutoff energy of 340 eV was used in all calculations. The structure optimizations were stopped when the force on each ion became smaller than 10 meV/Å. The generalized gradient approximation (GGA) of Perdew-Wang [38] was taken for the exchange-correlation functional throughout this study. The smearing method of Methfessel and Paxton [51] was used to calculate the partial occupancies of metallic materials at a finite temperature. The smearing width (σ) for each element was chosen so that it can be as large as possible while keeping the entropy term [81] in the total free energy less than 1 meV per atom. Based on this criterion, a σ of 0.2 eV was used for Rh and Ir; 0.1 eV for Ni, Pd and Pt; 0.5 eV for Cu and Ag. The zero temperature total energies were obtained by extrapolating to $\sigma = 0$ eV.

The lattice constants (a_0) of the seven fcc metals obtained from the bulk calculations are shown in Table 6.1. These values were used in the following slab calculations. For comparison, the experimental lattice constants are also listed in

Tab. 6.1: Calculated (a_0^{cal}) and experimental (a_0^{exp}) lattice constants of seven fcc transition metals.

	a_0^{cal} (Å)	a_0^{exp} (Å)	Δa_0 (%)
Ni	3.532	3.524	+0.2
Cu	3.644	3.615	+0.8
Rh	3.850	3.803	+1.2
Pd	3.962	3.891	+1.8
Ag	4.168	4.085	+2.0
Ir	3.887	3.839	+1.3
Pt	3.992	3.924	+1.7

Table 6.1. All calculated values are slightly larger than the corresponding experimental values as given in the last column of Table 6.1. This is normal when using the GGA.

For all slab calculations, surface unit cells were rhombic as illustrated in Fig. 6.1 and a $(8 \times 8 \times 1)$ Monkhorst-Pack grid [50], which corresponds to 20 irreducible **k**-points, was used for the Brillouin zone integration. For (311) and (331) slabs, the center two layers were fixed and all the others were allowed to move in the course of structure optimization, while for (210), only the center layer was fixed.

All calculations on Ni (bulk and slab) are spin-polarized. An initial magnetic moment of 0.63 μ_B obtained from the bulk calculations was assigned to all atoms in the slab calculations.

6.2.2 Results and Discussion

Tab. 6.2: Multilayer relaxations of (311) surfaces of seven fcc transition metals.

	Ni(311)	Cu(311)	Rh(311)	Pd(311)	Ag(311)	Ir(311)	Pt(311)
Δd_{12} (%)	−16.1	−13.9	−16.2	−12.4	−12.1	−22.7	−24.0
Δd_{23} (%)	+6.0	+4.4	+6.2	+6.9	+4.6	+10.6	+13.4
Δd_{34} (%)	−2.7	−0.8	−2.6	−3.0	−0.9	−4.1	−5.0
Δd_{45} (%)	+1.1	−0.3	−0.0	+1.2	−0.1	+0.2	+1.3
Δr_{12} (%)	−0.2	−0.2	−0.6	+1.1	+0.1	−1.2	−0.1
Δr_{23} (%)	−1.8	−1.6	−1.8	−1.9	−1.2	−3.1	−6.6
Δr_{34} (%)	+0.6	+1.0	+0.9	−0.1	+1.0	+1.4	−0.8
Δr_{45} (%)	+0.2	+0.2	+0.3	−0.6	+0.4	+0.1	−1.0

The multilayer relaxation results of the (311), (331) and (210) surfaces of

Tab. 6.3: Multilayer relaxations of (331) surfaces of seven fcc transition metals.

	Ni(331)	Cu(331)	Rh(331)	Pd(331)	Ag(331)	Ir(331)	Pt(331)
Δd_{12} (%)	−13.0	−14.2	−9.8	−14.2	−12.6	−10.0	−25.5
Δd_{23} (%)	−6.0	−4.8	−10.2	−4.4	−4.3	−15.0	−8.8
Δd_{34} (%)	+5.3	+7.5	+7.5	+9.7	+7.8	+12.2	+22.5
Δd_{45} (%)	−0.5	−3.0	−1.5	−4.0	−3.8	−2.1	−11.4
Δd_{56} (%)	−0.3	−0.3	−2.1	+1.4	+0.5	−3.1	+4.0
Δd_{67} (%)	−0.9	−0.7	−0.8	−1.0	−1.1	−0.5	−2.2
Δr_{12} (%)	−1.1	−1.0	−2.3	−1.3	−0.9	−3.9	−3.3
Δr_{23} (%)	−1.8	−1.8	−1.3	−2.9	−1.9	−0.9	−4.6
Δr_{34} (%)	+1.4	+1.6	+1.7	+1.0	+1.2	+2.1	+1.8
Δr_{45} (%)	+1.0	+0.7	+1.2	+0.9	+1.0	+1.1	+1.8
Δr_{56} (%)	−0.5	−0.5	−0.7	−0.8	−0.5	−1.0	−2.3
Δr_{67} (%)	−0.4	+0.2	−0.8	+0.4	+0.4	−0.7	+1.2

Tab. 6.4: Multilayer relaxations of (210) surfaces of seven fcc transition metals.

	Ni(210)	Cu(210)	Rh(210)	Pd(210)	Ag(210)	Ir(210)	Pt(210)
Δd_{12} (%)	−12.7	−16.4	−11.5	−17.3	−16.0	−14.9	−28.9
Δd_{23} (%)	−8.1	−5.9	−10.2	−3.7	−4.3	−11.3	−2.9
Δd_{34} (%)	+5.6	+6.7	+6.9	+9.4	+7.5	+8.3	+15.2
Δd_{45} (%)	+0.4	−0.9	−0.6	−4.6	−1.7	−0.0	−7.7
Δd_{56} (%)	−1.2	−0.7	−2.4	+0.7	−0.3	−4.0	+1.5
Δd_{67} (%)	+0.2	+0.0	+0.7	−0.3	+0.1	+1.5	−1.1
Δr_{12} (%)	−0.8	−0.9	−0.3	−2.5	−1.2	−0.2	−2.3
Δr_{23} (%)	−1.1	−1.0	−1.5	−2.7	−1.4	−1.3	−2.6
Δr_{34} (%)	+1.8	+2.2	+2.3	+2.0	+2.3	+3.6	+5.4
Δr_{45} (%)	+0.5	−0.3	+0.6	+0.6	−0.2	−0.2	+1.1
Δr_{56} (%)	−0.6	−0.8	−1.0	−0.3	−1.0	−1.3	−1.2
Δr_{67} (%)	−0.4	−0.1	−0.4	+0.5	+0.0	+0.0	+0.4

seven fcc TM's obtained from the pseudopotential DFT calculations are given in Tables 6.2–6.4. From these tables, it can be observed that:

Firstly, the relaxations of the interlayer spacings (Δd's) of all (311) surfaces follow the sequence $-+\cdots$, while (331) and (210) surfaces follow $--+\cdots$. Here, "$\cdots$" means that the sequence following the topmost two or three layers is not definite due to the small relaxations.

Secondly, except for the two heavy metals, i.e., Ir and Pt, the relaxations of the interlayer registries (Δr's) are relatively small (less than 3%) compared with the Δd's.

Thirdly, Ir and Pt, especially Pt, have more significant relaxations, both parallel and perpendicular to the surface normal, than the other five TM's.

With respect to the relaxations of the interlayer spacings, the sequence $- + \cdots$ for (311) and $- - + \cdots$ for (331) and (210) conform to the rule proposed in the last chapter. For fcc (311), the atoms in the topmost layer have 7 nn's and 10 in the second layer. From the third layer downwards, the number recovers to the bulk value, i.e., 12. In other words, fcc (311) has a nn sequence of (7,10,12 $\cdots$). According to the definition above, the surface slab for fcc (311) consists of 2 layers. The spacing within this slab, i.e., d_{12} contracts; while the spacing between this slab and the substrate, i.e., d_{23} expands. Therefore, the relaxation sequence is $- + \cdots$. The nn sequences for fcc (331) and (210) are (7,9,11,12 $\cdots$) and (6,9,11,12 $\cdots$), respectively, that is to say, the surface slabs consist of 3 layers. According to the rule, the spacings within the slabs, i.e., d_{12} and d_{23} contract and the spacing between the slabs and the substrates, i.e., d_{34} expand. Therefore, the relaxation sequence is $- - + \cdots$.

As for the relaxations of the interlayer registries, Tables 6.2–6.4 show that, on (331) and (210) surfaces, Δr's have the same trend as Δd's for the topmost three layers, while no obvious trend can be observed on (311) surfaces. However, since most of the Δr's are small and at the limit of the accuracy of DFT calculations, it is not practical to draw a meaningful conclusion on the trends of the relaxations of the interlayer registries from the current results.

The large relaxations on the surfaces of Ir and Pt can be understood from the point of view of surface energy (E_{surf}). The surface energies of all the surfaces at the bulk-truncated (unrelaxed) and the equilibrium (relaxed) configurations were calculated using $E_{\text{surf}} = (E_{\text{slab}} - NE_{\text{bulk}})/2$, where E_{slab} is the total energy of the slab, E_{bulk} the total energy per bulk atom and N the number of atoms in the slab. The factor 2 takes into account the two surfaces of the slab. The results are given in Table 6.5. It can be seen that the surfaces of Ir and Pt have much higher energy differences (ΔE) between the relaxed and unrelaxed configurations than the other surfaces. Since multilayer relaxation is a process of minimizing

Tab. 6.5: Surfaces energies of (311), (331) and (210) surfaces of seven fcc transition metals.

E_{surf} (eV/atom)	relaxed	unrelaxed	ΔE
Ni(311)	1.45	1.50	0.05
Ni(331)	1.86	1.91	0.05
Ni(210)	2.07	2.13	0.06
Cu(311)	1.09	1.12	0.03
Cu(331)	1.40	1.43	0.04
Cu(210)	1.48	1.53	0.05
Rh(311)	1.85	1.92	0.07
Rh(331)	2.35	2.44	0.10
Rh(210)	2.57	2.68	0.11
Pd(311)	1.27	1.30	0.03
Pd(331)	1.63	1.68	0.05
Pd(210)	1.76	1.82	0.06
Ag(311)	0.80	0.82	0.02
Ag(331)	1.03	1.06	0.02
Ag(210)	1.08	1.12	0.04
Ir(311)	2.24	2.40	0.16
Ir(331)	2.79	2.99	0.20
Ir(210)	3.12	3.33	0.21
Pt(311)	1.49	1.61	0.12
Pt(331)	1.85	2.04	0.19
Pt(210)	2.04	2.24	0.20

the surface free energy, the surfaces of Ir and Pt are expected to undergo large relaxations to release the extra energy. In certain cases, the large energy difference may result in surface reconstruction as has been observed on clean Pt(311) [12].

6.2.3 Comparisons with LEED Results

Comparisons of calculated relaxations with corresponding LEED results on Ni(311) [103], Cu(311) [67] and Rh(311) [104] are made in Table 6.6. It can be seen that the agreement between DFT and LEED for both Δd's and Δr's is excellent. The largest difference comes from Δd_{23} on Cu(311) surface, which is less than 0.03 Å. This value is within the accuracy of LEED and DFT.

Among the (331) fcc TM surfaces, only Cu(331) has been studied by LEED [69]. It was deduced from the LEED study that Cu(331) had an anomalous relaxation sequence since an expansion of d_{23} as shown in Table 6.7 was unexpected. However, the pseudopotential calculations obtained a sequence of $- - + \cdots$ for all the seven

Tab. 6.6: Comparison of multilayer relaxations of Ni(311), Cu(311) and Rh(311) surfaces with LEED results. The DFT results are from this work.

	Ni(311)		Cu(311)		Rh(311)	
	LEED [103]	DFT	LEED [67]	DFT	LEED [104]	DFT
Δd_{12} (%)	−15.9	−16.1	−11.9	−13.9	−14.5	−16.2
Δd_{23} (%)	+4.1	+6.0	+1.8	+4.4	+4.9	+6.2
Δd_{34} (%)	−1.6	−2.7	-	−0.8	−1.0	−2.6
Δr_{12} (%)	−0.8	−0.2	-	−0.2	0.0	−0.6
Δr_{23} (%)	−1.4	−1.8	-	−1.6	−1.5	−1.8
Δr_{34} (%)	+0.5	+0.6	-	+1.0	-	+0.9

Tab. 6.7: Comparison of multilayer relaxation of Cu(331) with the LEED and FLAPW results.

	This work	LEED [69]	FLAPW [70]
Δd_{12} (%)	−14.2	−13.8	−22.0
Δd_{23} (%)	−4.8	+0.4	+1.6
Δd_{34} (%)	+7.5	+3.6	+6.9
Δd_{45} (%)	−3.0	−4.3	−2.4

(331) fcc TM surfaces. No anomalous behavior was observed on Cu(331). From the LEED result, Δd_{23} is +0.4% (about 0.003 Å), which is much smaller than the error bars associated with the LEED analysis (about 0.03 Å) [69]. Regarding the discrepancy in d_{23}, it is postulated that d_{23} has a small relaxation at room temperature (either contraction or expansion), but a noticeable contraction at zero temperature (possibly, also at low temperature). Temperature dependence of relaxations is usually not a negligible effect when making a comparison between LEED and DFT [85]. Another fcc (331) surface that has been studied by both LEED and DFT is Al(331). The LEED experiment on this surface was conducted at low temperature [92] (115 K) and the agreement between the results from the LEED analysis and pseudopotential DFT calculations [93] is excellent.

Tab. 6.8: Comparison of multilayer relaxation results of Cu(211) from different studies.

	LEED [71]	FLAPW [70]	PP [72]	This work
Δd_{12} (%)	−14.9	−28.4	−14.4	−13.3
Δd_{23} (%)	−10.8	−3.0	−10.7	−10.5
Δd_{34} (%)	+8.1	+15.3	+10.9	+10.0

It is also noticed that a FLAPW study [70] reproduced the relaxation sequence

obtained by LEED as shown in Table 6.7. Yet, the large relaxation of d_{12} (-22.0%) obtained from the FLAPW study is unusual. The contraction (about 0.18 Å) is larger than the LEED result by about 0.07 Å. Such a large relaxation has never been experimentally observed on stepped Cu surfaces. The over-contraction of d_{12} may influence the other parameters. This can be seen from Table 6.8, where the multilayer relaxation results of Cu(211) from various studies are listed. The FLAPW result is from the same reference [70] as Cu(331). It can be seen that the Δd_{12} of Cu(211) from the FLAPW study is also significantly larger than the LEED result [71] as in the case of Cu(331), and the agreement on Δd_{23} and Δd_{34} is not convincing either. On the contrary, it can be seen that a pseudopotential (PP) study [72] shows excellent agreement with the LEED result. A reinvestigation of Cu(211) using the ultrasoft pseudopotential as described in the previous chapters was also conducted. A 25-layer slab and 21 irreducible **k**-points were used. The result is given in the last column of Table 6.8. It can be seen that the result also agrees with the LEED data and is consistent with the previous PP study.

Tab. 6.9: Comparison of multilayer relaxations of Cu(210), Pd(210) and Pt(210) surfaces with LEED results. The DFT results are from this work.

	Cu(210)		Pd(210)		Pt(210)	
	LEED [75]	DFT	LEED [91]	DFT	LEED [105]	DFT
Δd_{12} (%)	-11.12	-16.4	-3	-17.3	-23	-28.9
Δd_{23} (%)	-5.68	-5.9	$+7$	-3.7	-12	-2.9
Δd_{34} (%)	$+3.83$	$+6.7$	$+3$	$+9.4$	$+4$	$+15.2$
Δd_{45} (%)	$+0.06$	-0.9	-1	-4.6	-3	-7.7
Δd_{56} (%)	-0.66	-0.7	-	$+0.7$	-	$+1.5$
Δr_{12} (%)	-1.83	-0.9	-2	-2.5	$+1$	-2.3
Δr_{23} (%)	-2.51	-1.0	-1	-2.7	-2	-2.6
Δr_{34} (%)	$+1.68$	$+2.2$	-	$+2.0$	-5	$+5.4$
Δr_{45} (%)	-0.48	-0.3	-	$+0.6$	-1	$+1.1$
Δr_{56} (%)	$+0.06$	-0.8	-	-0.3	-	-1.2

Three fcc (210) TM surfaces have been investigated by LEED. They are Cu(210) [75], Pd(210) [91] and Pt(210) [105]. In Table 6.9, the results from LEED are compared with the pseudopotential calculations. It can be seen that the agreement obtained on Cu(210) is good for all the parameters except for a slightly larger difference (about 0.04 Å) on Δd_{12}. However, on Pd(210), the LEED results give

a relaxation sequence of $- + +$ for the first three interlayer spacings. From the LEED results of Pd(210) in Table 6.9, one can notice that the relaxation of d_{12} is considerably smaller (-3%), which has been questioned by the authors of the LEED study. From a pseudopotential DFT study, Lischka and Groß [101] have concluded that subsurface hydrogen could be the cause for the small relaxation of d_{12} observed in the experiment since Pd is a well-known hydrogen-storage material. As for Pt(210), the relaxation sequences of the interlayer spacings obtained from the LEED analysis and the pseudopotential calculations are consistent. The large relaxation of d_{12} is also reproduced by the pseudopotential calculations. However, quantitative comparisons of other parameters show weaker agreement. The discrepancies may be partly due to the small I-V dataset employed in the LEED analysis, where only the data below 120 eV was used. The small I-V dataset is reflected by the large error bars associated with that study, which are up to 0.06 Å (7%) for Δd's and 0.10 Å (6%) for Δr's.

6.3 Open Metal Surfaces of Other Structures

In Table 6.10, we list the relaxation sequences on all open Fe surfaces studied by quantitative low-energy electron diffraction analysis [88, 106–108]. It can be seen that these relaxation sequences are consistent with the proposed rule. This implies that the rule may also apply to open surfaces of bcc metals although the bcc structure is relatively less close-packed and the bulk atoms have only 8 nn's.

Tab. 6.10: Testing of the proposed rule on open Fe surfaces.

Orientation	nn sequence	N	Relaxation sequence	Reference
Fe(211)	(5, 7, 8 $\cdots$)	2	$- + \cdots$	[106]
Fe(310)	(4, 6, 8 $\cdots$)	2	$- + \cdots$	[88]
Fe(111)	(4, 7, 7, 8 $\cdots$)	3	$- - + \cdots$	[107]
Fe(210)	(4, 6, 6, 8 $\cdots$)	3	$- - + \cdots$	[108]

Compared with fcc and bcc metals, fewer open surfaces of hcp metals have been studied. Nevertheless, it is found that the relaxations on Be(10$\bar{1}$0) and Mg(10$\bar{1}$0) obey the proposed rule. The atoms in the first layer of hcp(10$\bar{1}$0) surface have 8 nn's, the second 10 and from the third layer downwards, the number recovers to the

bulk value, 12. Hence, the relaxation sequence is expected to be $- + \cdots$. This has been confirmed by quantitative LEED analysis on Be($10\bar{1}0$) and Mg($10\bar{1}0$) surfaces [86, 87, 109].

For missing-row (110)-(1x2) and (311)-(1x2) surfaces of fcc metals, the surface slabs consist of one more atomic layer than those in the unreconstructed configurations due to the missing rows. The expansions are, therefore, expected to be delayed to one layer deeper, i.e. to Δd_{34}. Indeed, this is found to be true for Pt by first-principles calculations [102].

6.4 Conclusion

The multilayer relaxation rule proposed in last chapter has been evaluated on (311), (331) and (210) surfaces of Ni, Cu, Rh, Pd, Ag, Ir and Pt by pseudopotential DFT calculations. The calculations show a relaxation sequence of $- + \cdots$ for the interlayer spacings of all the (311) surfaces and $- - + \cdots$ for all (331) and (210) surfaces. These results are consistent with the proposed rule. This implies that the surfaces of the same orientation, but of different metals, tend to have the same relaxation sequence. Moreover, it has been shown that the proposed rule may also apply to bcc and hcp metals and even reconstructed missing-row surfaces.

Chapter 7

Concluding Remarks

The structures of Cu(210) and Fe(310) have been studied by quantitative LEED analyses and first-principles pseudopotential calculations. It is demonstrated that the layer-doubling method works well for high-index transition metal surfaces with interlayer spacings down to at least 0.8 Å. This study suggest that, in future quantitative LEED analysis on similar surfaces, especially those with chemical (or physical) adsorptions, the layer-doubling method can be adopted to save computational efforts. It is also shown that the agreement on the structural parameters obtained from the two techniques with a tolerance of about 0.04 Å can be achieved on both surfaces. This indicates the plane-wave method using ultrasoft pseudopotentials is a reliable tool for studying the structures of high-index transition metal surfaces, which are traditionally inaccessible using norm-conserving pseudopotentials due to the prohibitively large cut-off energy for the basis set.

A general rule of the multilayer relaxations on open metal surfaces has been proposed. This rule relates the relaxation sequence to the reduction in the number of the nearest neighbors in the surface region. With this rule, the relaxation sequence of an open metal surface can be known *a priori*. This rule is consistent with both the physical picture based on Smoluchowski's charge smoothing and the chemical picture based on Pauling's bond-order–bond-length relation.

To check the validity of this rule, pseudopotential calculations have been carried out. Firstly, taking Cu as an example, the high-index surfaces of the fcc structure with interlayer spacings down to 0.5 Å are studied. It is shown that the proposed rule is obeyed on all these surfaces. Secondly, the relaxations of (311), (331) and (210) surfaces of seven transition metals (namely, Ni, Cu, Rh, Pd, Ag, Ir and Pt) have been studied. The results show that the surfaces of the same orientation, but of different materials, have the same relaxation sequence and conform to the proposed rule. Moreover, it has been demonstrated that this rule may also apply to open surfaces of other structures, such as bcc, hcp and even reconstructed missing-row metal surfaces. Based on the evidence above, it is expected that the proposed rule is universally applicable to open metal surfaces.

Despite the consistency between the proposed rule and the pseudopotential calculations, discrepancy with LEED results on several surfaces has been noticed. Therefore, further evaluation of this rule on more surfaces by both quantitative LEED analysis and first-principle calculations are needed.

Finally, it is worth mentioning that this rule addresses only the relaxations within the surface slab and the relaxation between the surface slab and the substrate. Sometimes, deeper interlayer spacings do relax significantly and oscillatory relaxations have been found on some low-index surfaces, which has been attributed to the Friedel oscillations of the charge density near the surfaces [110, 111]. However, this oscillatory relaxation is not routinely found on high-index surfaces. The relation of the relaxation sequence to the Friedel oscillation is, therefore, an interesting topic for future work.

Bibliography

[1] G. A. Somorjai, K. R. McCrea, and J. Zhu, *Topics in Catalysis* **18**, 157 (2002).

[2] J. Stangl, V. Holy, J. Grim, G. Bauer, J. Zhu, K. Brunner, G. Abstreiter, O. Kienzle, and F. Ernst, *Thin Solid Films* **357**, 71 (1999).

[3] K. Brunner, J. Zhu, G. Abstreiter, O. Kienzle, and F. Ernst, *Thin Solid Films* **369**, 39 (2000).

[4] H. Suzuki, H. Nakahara, S. Miyata, and A. Ichimiya, *Surf. Sci.* **493**, 166 (2001).

[5] A. A. Baski, K. M. Saoud, and K. M. Jones, *Appl. Surf. Sci.* **182**, 216 (2001).

[6] D. Spišák and J. Hafner, *Phys. Rev. B* **67**, 214416 (2003).

[7] A. J. Gellman, J. D. Horvath, and M. T. Buelow, *J. Mol. Catal. A* **167**, 3 (2001).

[8] A. Ahmadi, G. Attard, J. Feliu, and A. Rodes, *Langmuir* **15**, 2420 (1999).

[9] C. M. Chan, M. A. Van Hove, W. H. Weinberg, and E. D. Williams, *Solid State Commun.* **30**, 47 (1979).

[10] E. C. Sowa, M. A. Van Hove, and D. L. Adams, *Surf. Sci.* **199**, 174 (1988).

[11] H. Landskron, N. Bickel, K. Heinz, G. Schmidtlein, and K. Müller, *J. Phys.: Condens. Matter* **1**, 1 (1989).

[12] R. Kose and D. A. King, *Chem. Phys. Lett.* **313**, 1 (1999).

[13] C. Davisson and L. H. Germer, *Phys. Rev.* **30**, 705 (1927).

[14] P. R. Watson, M. A. Van Hove, and K. Hermann, *NIST Surface Structure Database Ver. 4.0, NIST Standard Reference Data Program* (Gaithersburg, MD, USA, 2002).

[15] J. B. Pendry, *Low Energy Electron Diffraction* (Academic Press, London, 1974).

[16] M. A. Van Hove and S. Y. Tong, *Surface Crystallography by LEED* (Springer, Berlin, 1979).

[17] A. Chutjian, *Rev. Sci. Instrum.* **50**, 347 (1979).

[18] J. Rundgren, *Phys. Rev. B* **59**, 5106 (1999).

[19] S. Walter, H. Baier, M. Weinelt, K. Heinz, and Th. Fauster, *Phys. Rev. B* **63**, 155407 (2001).

[20] S. Walter, V. Blum, L. Hammer, S. Müller, K. Heinz, and M. Giesen, *Surf. Sci.* **458**, 155 (2000).

[21] V. Fritzsche, *Phys. Rev. B* **50**, 1922 (1994).

[22] J. C. Adams, *Proc. Roy. Soc. London* **27**, 63 (1878).

[23] P. L. de Andres and D. A. King, *Comput. Phys. Commun.* **138**, 281 (2001).

[24] D. A. Varshalovic, A. N. Moskalev, and V. K. Khersonskii, *Quantum Theory of Angular Momentum* (World Scientific, Singapore, 1988).

[25] M. A. Van Hove, S. Y. Tong, and M. H. Elconin, *Surf. Sci.* **64**, 85 (1971).

[26] E. Zanazzi and F. Jona, *Surf. Sci.* **62**, 61 (1977).

[27] J. B. Pendry, *J. Phys. C* **13**, 937 (1980).

[28] M. A. Van Hove and R. J. Koestner. In P. M. Marcus and Jona. F., editors, *Proc. Conf. on Determination of Surface Science by LEED*, 357 (Plenum, New York, 1984).

[29] W. H. Press, S. A. Teukolsky, W. T. Vetterling, and B. P. Flannery, *Numerical Recipes in Fortran 77: the art of scientific computing* (Cambridge University Press, Cambridge, 1992).

[30] P. J. Rous, *Surf. Sci.* **296**, 358 (1993).

[31] R. Döll and M. A. Van Hove, *Surf. Sci.* **355**, L393 (1996).

[32] M. Kottcke and K. Heinz, *Surf. Sci.* **376**, 352 (1997).

[33] P. J. Rous, J. B. Pendry, D. K. Saldin, K. Heinz, K. Müller, and N. Bickel, *Phys. Rev. Lett.* **57**, 2951 (1986).

[34] N. F. Materer, *Surf. Sci.* **491**, 131 (2001).

[35] Y. Y. Sun, H. Xu, J. C. Zheng, J. Y. Zhou, Y. P. Feng, A. C. H. Huan, and A. T. S. Wee, *Phys. Rev. B* **68**, 115420 (2003).

[36] P. Hohenberg and W. Kohn, *Phys. Rev.* **136**, B864 (1964).

[37] W. Kohn and L. J. Sham, *Phys. Rev.* **140**, A1133 (1965).

[38] J. P. Perdew and Y. Wang, *Phys. Rev. B* **45**, 13244 (1992).

[39] J. P. Perdew, K. Burke, and M. Ernzerhof, *Phys. Rev. Lett.* **77**, 3865 (1996).

[40] B. Hammer, L. B. Hansen, and J. K. Nørskov, *Phys. Rev. B* **59**, 7413 (1999).

[41] T. L. Beck, *Rev. Mod. Phys.* **72**, 1041 (2000).

[42] R. Car and M. Parrinello, *Phys. Rev. Lett.* **55**, 2471 (1985).

[43] M. C. Payne, M. P. Teter, D. C. Allan, T. A. Arias, and J. D. Joannopoulos, *Rev. Mod. Phys.* **64**, 1045 (1992).

[44] D. R. Hamann, M. Schlüter, and C. Chiang, *Phys. Rev. Lett.* **43**, 1494 (1979).

[45] G. B. Bachelet, D. R. Hamann, and M. Schlüter, *Phys. Rev. B* **26**, 4199 (1982).

[46] L. Kleinman and D. M. Bylander, *Phys. Rev. Lett.* **48**, 1425 (1982).

[47] D. Vanderbilt, *Phys. Rev. B* **41**, 7892 (1990).

[48] K. Laasonen, A. Pasquarello, R. Car, C. Lee, and D. Vanderbilt, *Phys. Rev. B* **47**, 10142 (1993).

[49] D. J. Chadi and M. L. Cohen, *Phys. Rev. B* **8**, 5747 (1973).

[50] H. J. Monkhorst and J. D. Pack, *Phys. Rev. B* **13**, 5188 (1976).

[51] M. Methfessel and A. T. Paxton, *Phys. Rev. B* **40**, 3616 (1989).

[52] D. Kevin and C. Severance, *High performance computing* (O'Reilly, Sebastopol, 1998).

[53] D. M. Wood and A. Zunger, *J. Phys. A* **18**, 1343 (1985).

[54] P. Löwdin, *J. Chem. Phys.* **19**, 1396 (1951).

[55] P. Pulay, *Chem. Phys. Lett.* **73**, 393 (1980).

[56] G. Kresse and J. Furthmüller, *Phys. Rev. B* **54**, 11169 (1996).

[57] G. P. Kerker, *Phys. Rev. B* **23**, 3082 (1981).

[58] R. P. Feynman, *Phys. Rev.* **56**, 340 (1939).

[59] P. Pulay, *Mol. Phys.* **17**, 197 (1969).

[60] M. Scheffler, J. P. Vigneron, and G. B. Bachelet, *Phys. Rev. B* **31**, 6541 (1985).

[61] J. Perdereau and G. E. Rhead, *Surf. Sci.* **24**, 555 (1971).

[62] B. Lang, R. W. Joyner, and G. A. Somorjai, *Surf. Sci.* **30**, 440 (1972).

[63] J. B. Pendry, *Phys. Rev. Lett.* **27**, 856 (1971).

[64] M. A. Van Hove. In A. Gonis and G. M. Stocks, editors, *Equilibrium Structure and Properties of Surfaces and Interfaces*, 231 (Plenum, New York, 1992).

[65] Y. Tian, J. Quinn, K. W. Lin, and F. Jona, *Phys. Rev. B* **61**, 4904 (2000).

[66] J. L. Beeby, *J. Phys. C* **1**, 82 (1968).

[67] S. R. Parkin, P. R. Watson, R. A. McFarlane, and K. A. R. Mitchell, *Solid State Commun.* **78**, 841 (1991).

[68] D. Spišák, *Surf. Sci.* **489**, 151 (2001).

[69] Y. Tian, K. W. Lin, and F. Jona, *Phys. Rev. B* **62**, 12844 (2000).

[70] W. T. Geng and A. J. Freeman, *Phys. Rev. B* **64**, 115401 (2001).

[71] Th. Seyller, R. D. Diehl, and F. Jona, *J. Vac. Sci. Technol. A* **17**, 1635 (1999).

[72] C. Y. Wei, S. P. Lewis, E. J. Mele, and A. M. Rappe, *Phys. Rev. B* **57**, 10062 (1998).

[73] M. Albrecht, H. L. Meyerheim, W. Moritz, R. Blome, D. Walko, and I. K. Robinson, unpublished.

[74] Y. P. Guo, K. C. Tan, A. T. S. Wee, and C. H. A. Huan, *Surf. Rev. Lett.* **6**, 819 (1999).

[75] Ismail, S. Chandravakar, and D. M. Zehner, *Surf. Sci.* **504**, L201 (2002).

[76] S. Y. Tong and M. A. Van Hove, *Phys. Rev. B* **16**, 1459 (1977).

[77] Y. Y. Sun, A. T. S. Wee, and A. C. H. Huan, *Surf. Rev. Lett.* **10**, 493 (2003).

[78] V. L. Moruzzi, J. F. Janak, and A. R. Williams, *Calculated Electronic Properties of Metals* (Pergamon, New York, 1978).

[79] Y. P. Guo, K. C. Tan, H. Q. Wang, C. H. A. Huan, and A. T. S. Wee, *Phys. Rev. B* **66**, 165410 (2002).

[80] G. Kresse and J. Hafner, *Phys. Rev. B* **47**, 558 (1993).

[81] G. Kresse and J. Furthmüller, *Computat. Mat. Sci.* **6**, 15 (1996).

[82] G. Kresse and D. Joubert, *Phys. Rev. B* **59**, 1758 (1999).

[83] G. Kresse and J. Hafner, *J. Phys.: Condens. Matter* **6**, 8245 (1994).

[84] J. P. Perdew and A. Zunger, *Phys. Rev. B* **23**, 5048 (1981).

[85] K. Pohl, J. H. Cho, K. Terakura, M. Scheffler, and E. W. Plummer, *Phys. Rev. Lett.* **80**, 2853 (1998).

[86] Ismail, E. W. Plummer, M. Lazzeri, and S. de Gironcoli, *Phys. Rev. B* **63**, 233401 (2001).

[87] Ismail, Ph. Hofmann, A. P. Baddorf, and E. W. Plummer, *Phys. Rev. B* **66**, 245414 (2002).

[88] J. Sokolov, F. Jona, and P. M. Marcus, *Phys. Rev. B* **29**, 5402 (1984).

[89] W. T. Geng, M. Kim, and A. J. Freeman, *Phys. Rev. B* **63**, 245401 (2001).

[90] J. G. Che, C. T. Chan, W. E. Jian, and T. C. Leung, *Phys. Rev. B* **57**, 1875 (1998).

[91] D. Kolthoff, H. Pfnür, A. G. Fedorus, V. Koval, and A. G. Naumovets, *Surf. Sci.* **439**, 224 (1999).

[92] D. L. Adams and C. S. Sørensen, *Surf. Sci.* **166**, 495 (1986).

[93] J. S. Nelson and P. J. Feibelman, *Phys. Rev. Lett.* **68**, 2188 (1992).

[94] M. Methfessel, D. Hennig, and M. Scheffler, *Phys. Rev. B* **46**, 4816 (1992).

[95] P. J. Feibelman, *Phys. Rev. B* **53**, 13740 (1996).

[96] M. W. Finnis and V. Heine, *J. Phys. F* **4**, L37 (1974).

[97] R. Smoluchowski, *Phys. Rev.* **60**, 661 (1941).

[98] L. Pauling, *The Nature of the Chemical Bond* (Cornell University Press, Ithaca, New York, 1960).

[99] H. L. Skriver, *The LMTO method* (Springer-Verlag, Berlin, 1984).

[100] W. T. Geng, A. J. Freeman, and R. Q. Wu, *Phys. Rev. B* **63**, 064427 (2001).

[101] M. Lischka and A. Groß, *Phys. Rev. B* **65**, 075420 (2002).

[102] S. J. Jenkins, M. A. Petersen, and D. A. King, *Surf. Sci.* **494**, 159 (2001).

[103] D. L. Adams, W. T. Moore, and K. A. R. Mitchell, *Surf. Sci.* **149**, 407 (1985).

[104] S. Liepold, N. Elbel, M. Michl, W. Nichtl-Pecher, K. Heinz, and K. Müller, *Surf. Sci.* **240**, 81 (1990).

[105] X. G. Zhang, M. A. Van Hove, G. A. Somorjai, P. J. Rous, D. Tobin, A. Gonis, J. M. MacLaren, K. Heinz, M. Michl, H. Lindner, K. Müller, M. Ehsasi, and J. H. Block, *Phys. Rev. Lett.* **67**, 1298 (1991).

[106] J. Sokolov, H. D. Shih, U. Bardi, F. Jona, and P. M. Marcus, *J. Phys.: Condens. Matter* **17**, 371 (1984).

[107] J. Sokolov, F. Jona, and P. M. Marcus, *Phys. Rev. B* **33**, 1397 (1986).

[108] J. Sokolov, F. Jona, and P. M. Marcus, *Phys. Rev. B* **31**, 1929 (1985).

[109] Ph. Hofmann, K. Pohl, R. Stumpf, and E. W. Plummer, *Phys. Rev. B* **53**, 13715 (1996).

[110] J.-H. Cho, Ismail, Z. Zhang, and E. W. Plummer, *Phys. Rev. B* **59**, 1677 (1999).

[111] P. Staikov and T. S. Rahman, *Phys. Rev. B* **60**, 15613 (1999).